The Pacific Cooperative Studies Unit
UNIVERSITY OF HAWAI`I AT MĀNOA
Dr. David C. Duffy, Unit Leader
Department of Botany
3190 Maile Way, St. John #408
Honolulu, Hawai'i 96822

Technical Report 193

Climatology of Haleakalā

July 2015

Ryan J. Longman[1], Thomas W. Giambelluca[1], Michael A. Nullet[1] and Lloyd L. Loope[2]

[1] University of Hawai'i Department of Geography, 2424 Maile Way, Saunders Hall, 445, Honolulu, HI 96822
[2] L. L. Loope (retired) Formerly: USGS Pacific Island Ecosystems Research Center, Haleakalā Field Station, Makawao (Maui), HI. Current address: 751 Pelenaka Place, Makawao, HI 96768

PCSU is a cooperative program between the University of Hawai`i and U.S. National Park Service, Cooperative Ecological Studies Unit.

Organization Contact Information:
Ryan J. Longman, rlongman@hawaii.edu

Recommended Citation:
Longman, R. J., T. W. Giambelluca, M. A. Nullet and L. L. Loope. 2015. Climatology of Haleakalā. Technical Report No. 193. Pacific Cooperative Studies Unit, University of Hawai'i, Honolulu, Hawai'i. 126 pp.

Key words:
HaleNet, trade wind inversion, Hawai'i microclimates, high elevation climate change, climate monitoring, data quality control techniques, climate change

Place key words:
Haleakalā Volcano, Haleakalā National Park, Maui, Hawaii

About this technical report series:

This technical report series began in 1973 with the formation of the Cooperative National Park Resources Studies Unit at the University of Hawai'i at Mānoa. In 2000, it continued under the Pacific Cooperative Studies Unit (PCSU).

The Pacific Cooperative Studies Unit at the University of Hawai'i at Mānoa works to protect cultural and natural biodiversity in the Pacific while encouraging a sustainable economy. PCSU works cooperatively with private, state and federal land management organizations, allowing them to pool and coordinate their efforts to address problems across the landscape.

Acknowledgments

The data analysis presented here and the preparation of this report were supported by the Pacific Island Climate Science Center (PICSC) and the Pacific Island Climate Change Cooperative (PICCC) and the Pacific Island Ecosystem Research Center (PIERC). We also thank Paul Krushelnycky, Shelley Crausbay, Abby Frazier, Henry Diaz, Erica von Allmen, Thomas Schroeder and Ross Sutherland for their contributions to this report. In conducting fieldwork on Maui, the authors were given support, encouragement, and assistance by numerous individuals. We extend our gratitude especially to Jotoku and Doris Asato, Dennis Nullet, Bill Minyard, Ryan Mudd, Dave Penn, Ron Nagata, Ted Rodrigues, Timmy Bailey, Matt Brown, Pamela Waiolena, Chuck Chimera, Kathy Wakely, Philip Thomas, and Sabine Jessel. We thank Haleakalā National Park and PIERC, and the USGS, for their long support of the HaleNet system. We owe a special debt of gratitude to Gordon Tribble of PIERC for his unwavering commitment to sustaining HaleNet. We would also like to thank Jeff Burgett of PICCC, Deborah Solis of the U.S. Army Corps of Engineers and Neil Fujii and Jeremy Kimura of the Commission on Water Resource Management. Over the years, HaleNet research has also been supported with funding from the University of Hawai‘i Research Council, the Water Resources Institute Program of the U.S. Geological Survey, the Cooperative National Parks Resources Study Unit, NSF EPSCoR (under award 0903833), and PICCC.

Abstract

The steep mountain slopes of Haleakalā Volcano (Maui, HI) support some of the most spatially diverse environments on the planet. Microclimates found across vertical gradients on the mountain slopes can change over relatively short differences in slope exposure and elevation and are strongly influenced by a persistent temperature inversion and northeast trade winds that are characteristic of this region. Eleven climate stations, which comprise the HaleNet climate network, have been monitoring climatic conditions along a 2030-m leeward (960 to 2990 m) and a 810-m windward (1650 to 2460 m) elevational transect, beginning as early as June of 1988. Hourly measurements of solar radiation, net radiation, relative humidity, wind speed, temperature, precipitation and soil moisture, and derived variables including potential evapotranspiration, vapor pressure deficit, soil heat flux, and daytime cloud attenuation of sunlight are analyzed in this study. This report documents the annual, diurnal and elevational characteristics of these climatic variables as well as their behavior over the period-of-record (~1988 to 2013) in both the 6-month dry (May – October) and wet (November to April) seasons.

Results show that the climate gradients along both leeward and windward elevation transects are highly influenced by the trade wind inversion in both dry and wet seasons. Period-of-record trends in the dry-season, show increases in energy and decrease in moisture at high elevations (>2000 m). Significant dry season changes include: decreases in precipitation (5 to 8% decade^{-1}), relative humidity (3 to 5% decade^{-1}) and cloud attenuation of sunlight (-2 to -5% decade^{-1}) and increase in solar radiation (2 to 4% decade^{-1}), vapor pressure deficit (9 to 10 % decade^{-1}), zero precipitation days (4 to 5% decade^{-1}) and potential evapotranspiration (3 to 7% decade $^{-1}$). For the wet season, an opposite signal of change was observed at high elevation although trends were not as robust as the dry season trends. Reported dry season trends are potentially explained by a 4% significant increase in TWI frequency identified over a similar observation period (1991-2013). In addition to a climate variable analysis, this report also highlights other past and ongoing research projects that have taken place on the mountain and provides a summary of the history of the HaleNet climate network, the people and organizations that have contributed to its operation, and a list of publications that have made use of HaleNet climate data. It is the authors' hope that this information will aid resource managers in protecting the ecosystems and other natural resources, and provide insight into ongoing and future climate changes on Haleakalā.

Table of Contents

List of Tables

List of Figures

List of Abbreviations

CA - cloud attenuation of sunlight

CWI - cloud water interception

ENSO - El Niño Southern Oscillation

HST - Hawai‘i standard time

K - incoming shortwave radiation

LCL - lifting condensation level

P - precipitation

PDO - Pacific Decadal Oscillation

PET - Potential Evapotranspiration

RH - relative humidity

R_n - net radiation

SHF - soil heat flux

SM - soil moisture

SST - sea surface temperature

T_a - surface air temperature

TMCF - tropical montane cloud forest

TWI - trade wind inversion

VPD - vapor pressure deficit

WS - wind speed at 2 meters

ZP - zero precipitation days

1. Introduction

Climate is the driving factor behind the physical, chemical and biological processes operating within the natural environment. The climatology of a mountain is a composite of a multitude of microclimates that change through space and time. The myriad of microclimates along elevation transects on the high mountains in Hawai‘i determines the local variability in ecosystem processes, species composition, and the distribution of vegetation (Riehl et al., 1951; Parmesan 1996; Giambelluca and Nullet, 1991; Crausbay and Hotchkiss, 2010). Haleakalā Volcano, which is located on the Island of Maui, is the third highest mountain in the Hawaiian archipelago extending 3055 m above sea level. Haleakalā is a shield shaped volcano which originated in the early Pleistocene (0.8 myr) and is still considered to be volcanically active (Sherrod et al., 2007). Though volcanic episodes have lessened, Haleakalā has continued to erupt every 200 to 500 years and its youngest lava flows are thought to have formed between A.D. 1449 and 1633 (Sherrod et al., 2007). The summit of Haleakalā, located at 20°42' N and 156°15' W, overlooks a large erosional depression (often referred to as a crater) which is 12 km long and 4 km wide and has ten cinder cones on its floor and sheets of exposed pyroclastic materials on the outer walls. Maui Island, like most of the main Hawaiian Islands, has distinctly different climates on windward and leeward slopes. Great environmental contrasts occur within short distances as a result of the diverse topography and the influence of general and local circulation patterns. Along the windward exposure of the volcano, the persistent northeast trade winds push moist marine air towards mountain slopes where it is orograhically lifted to form a persistent cloud layer and provides a steady source of precipitation. On the leeward side of the mountain, clouds are formed by convective forces that move air up the mountain slopes throughout the day (Leopold, 1949). One of the most striking climatic features affecting the volcano is the trade wind inversion (TWI), a synoptic subsidence inversion that prevents orographic precipitation or the formation of clouds above its base height (Riehl, 1979: Giambelluca and Nullet, 1991: Cao et al., 2007). Because vertical lifting is suppressed by the presences of TWI, moisture regimes are decreased, and radiative fluxes are increased, at locations above the TWI base height (Giambelluca and Nullet, 1992a). Elevation, proximity to the mean TWI base height and exposure to prevailing winds are all primary factors determining microclimates along the slopes

of the volcano. As a result of these environmental characteristics, ecosystems can range from desert, to tropical rainforest, to alpine shrubland over very short distances.

In 1916, upper Haleakalā Volcano was made part of Hawai‘i National Park. This area, along with subsequent additions, became Haleakalā National Park in 1961 and currently protects 13,444 ha of land, of which 10,003 ha are designated as a wilderness area managed under the Wilderness Act of 1964 (NPS, 2015). The park encompasses the summit/“crater” area and its boundary extends down to sea level on the eastern flank of the mountain. More than 90% of the native biota that is found within the park boundaries is endemic to the Hawaiian Islands and nearly 50% is endemic to the Island of Maui (NPS, 2015). Despite the high percentages of native and endemic species found in the park, the introduction of alien plants and animals primarily by anthropogenic activities has led to the decline and in some cases extinction of many native species. The National Park has had a profound impact on the preservation of high-elevation ecosystems through fencing efforts and the removal of feral goats and other invasive alien species (NPS, 2015).

The primary objective of this report is to characterize the general climatology of Haleakalā Volcano through an analysis of field observations obtained from the eleven climate stations that make up the HaleNet climate network located on the mountain (Figure 1). This climatology includes analysis of the spatial and temporal characteristics of the various microclimates found along two mountain slope transects located on windward and leeward exposures of the mountain and a analysis of long-term (~25 yrs) climate variability. We analyze seven measured variables and five derived variables in this report and characterize our findings in terms of spatial and temporal characteristics. Period-of-record changes are assessed for 10 climate variables and described in terms of changes to available energy and moisture. An attempt is made to link changes in atmospheric variables to changes in TWI characteristics, which are assessed for the overlapping period of record. In addition to climate data analysis, we provide a brief synthesis of related ongoing and past research focused on Haleakalā, and a list of research publications that have made use of HaleNet climate data.

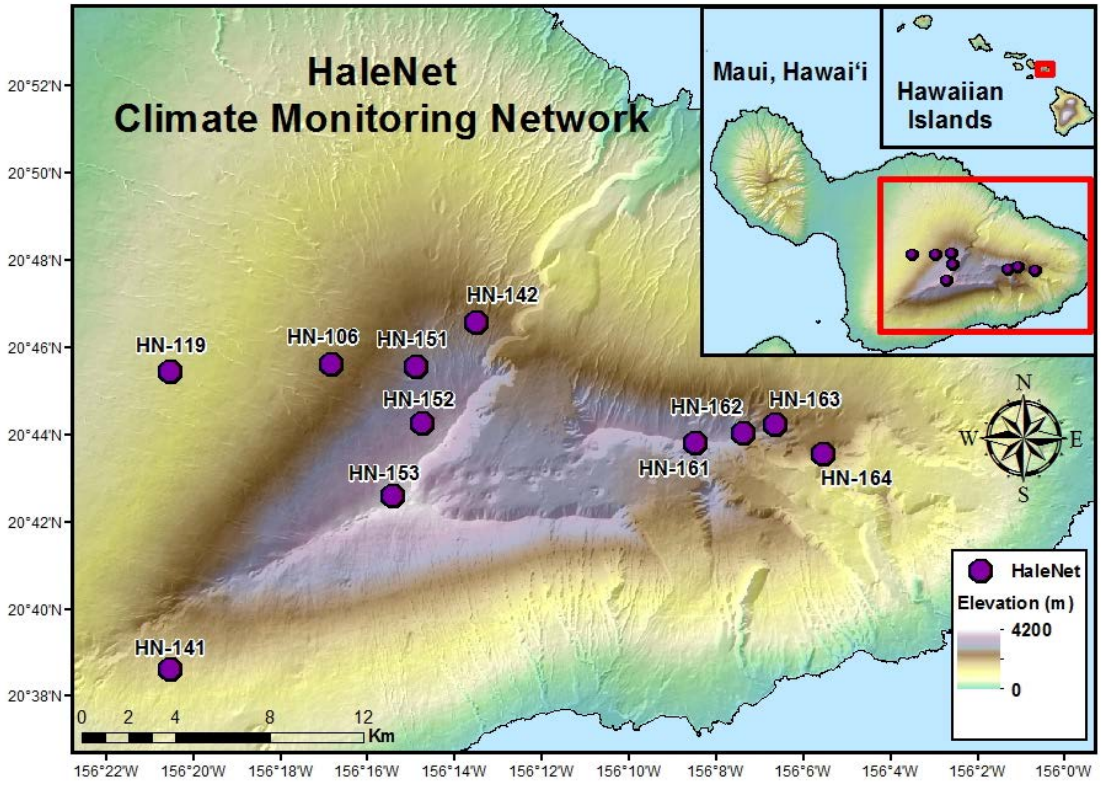

Figure 1: HaleNet climate network, Haleakalā Volcano, East Maui, Hawai'i.

2. Physical Setting

2.1 Climate and Vegetation Characteristics

The general climate around the main Hawaiian Islands is relatively dry, with rainfall over the open ocean less than ~600 mm yr $^{-1}$ (Adler et al., 2003). The islands themselves however, may receive up to 15 times the open-ocean rainfall as a result of the orographic lifting of moist marine air driven by the persistent northeast trade winds (Loope and Giambelluca, 1998). The mean annual cycle of climate in Hawai'i is usually described in terms of two 6-month seasons (May-Oct and Nov-Apr), which correspond to the traditional dry and wet seasons (Giambelluca and Schroeder, 1998). Trade winds are present between 80-90% of the year, thus dominating surface airflow and weather patterns (Cao et al., 2007). The TWI is created as a result of subsiding air from the upper troposphere interacting with convection-driven air from the surface (Riehl, 1979; Giambelluca and Nullet, 1991; Cao et al., 2007). Both the trade winds and the TWI are associated with the thermally-driven circulation, known as the Hadley Cell, in which air is

lifted near the equator and pushed poleward, where it subsides in the subtropics (Diaz and Bradley, 2005). Hawai‘i lies in the zone of subsiding air within the Hadley Cell circulation.

The TWI layer inhibits the vertical movement of air up the mountain, which causes a sharp contrast in rainfall at high elevations (Giambelluca and Nullet, 1991). The TWI is a prominent feature on the mountain occurring on average 83% (±9% s.d.) of the year at an average base height of 2159 m (±148 m s.d.) based on the most recent ~2 decades of TWI characteristic data (1991-2013) (Longman, 2015). In general, during the dry season mean TWI frequency is greater (+3%) and mean base height is higher (+112 m) than during the wet season (Figure 2). Maximum TWI frequency occurs in June (88%) and minimum TWI frequency occurs in November (79%; Table 1).

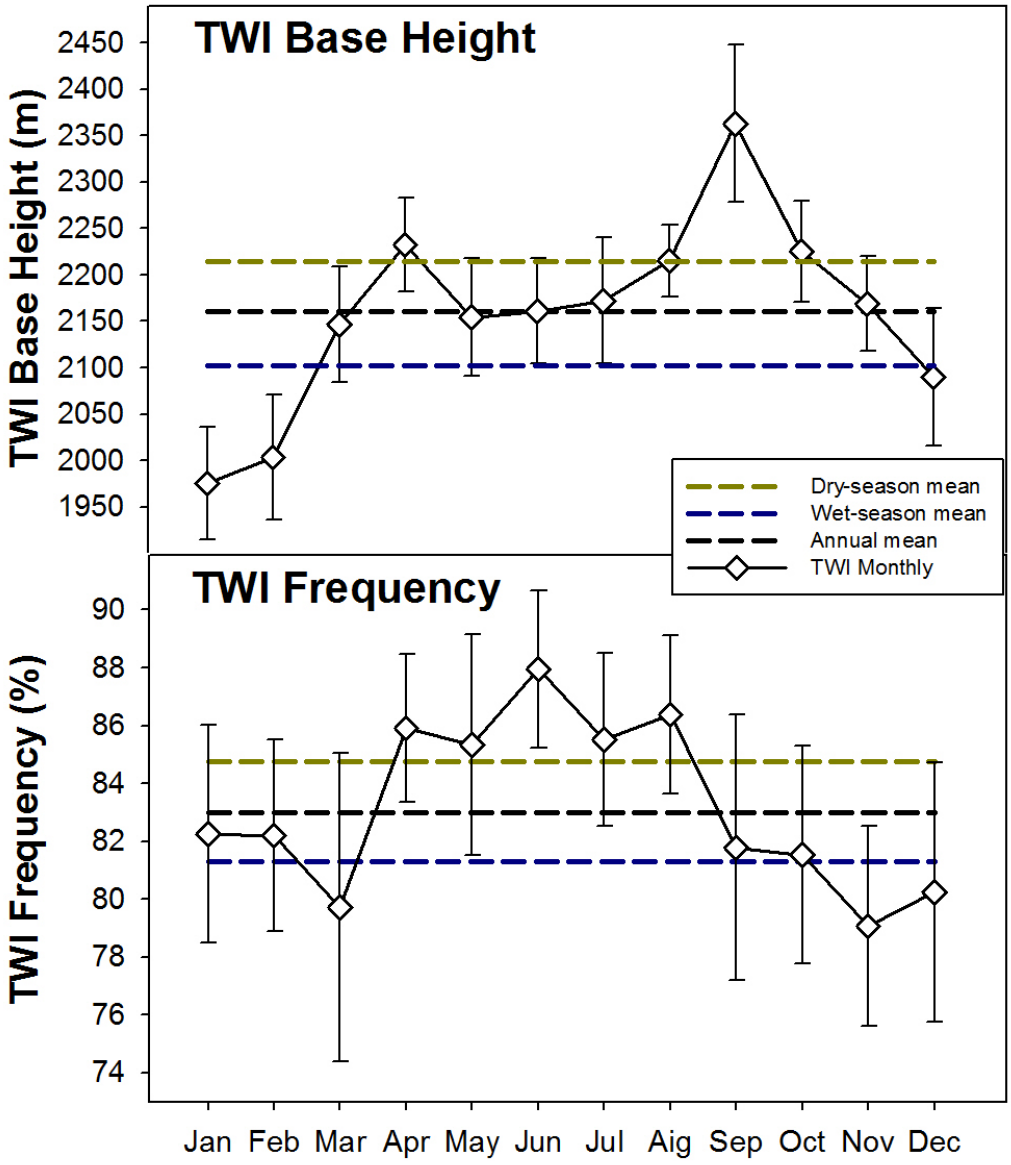

Figure 2: Mean annual cycle for TWI base height (top) and frequency of occurrence (bottom); error bars represent the 95% confidence limits.

Table 1: Mean annual cycle of TWI base height (m) and Frequency of occurrence (%).

Variable	Jan	Feb	Mar	Apr	May	Jun	Jul	Aug	Sep	Oct	Nov	Dec	Annual	Dry	Wet
Base Ht.	1977	2014	2149	2232	2154	2161	2172	2215	2363	2225	2169	2090	2160	2215	2105
Frequency	82	82	79	86	85	88	86	86	82	82	79	80	83	85	81

The complex topography of Haleakalā interacts with atmospheric circulation to produce some of the most spatially complex rainfall patterns in the world (Lyons, 1982; Chu et al., 1993; Schroeder, 1993; Giambelluca et al., 2012; Figure 3). Desert-like precipitation minimum zones and extreme wet conditions can be found within a few tens of kilometers distance (Giambelluca et al., 2012).

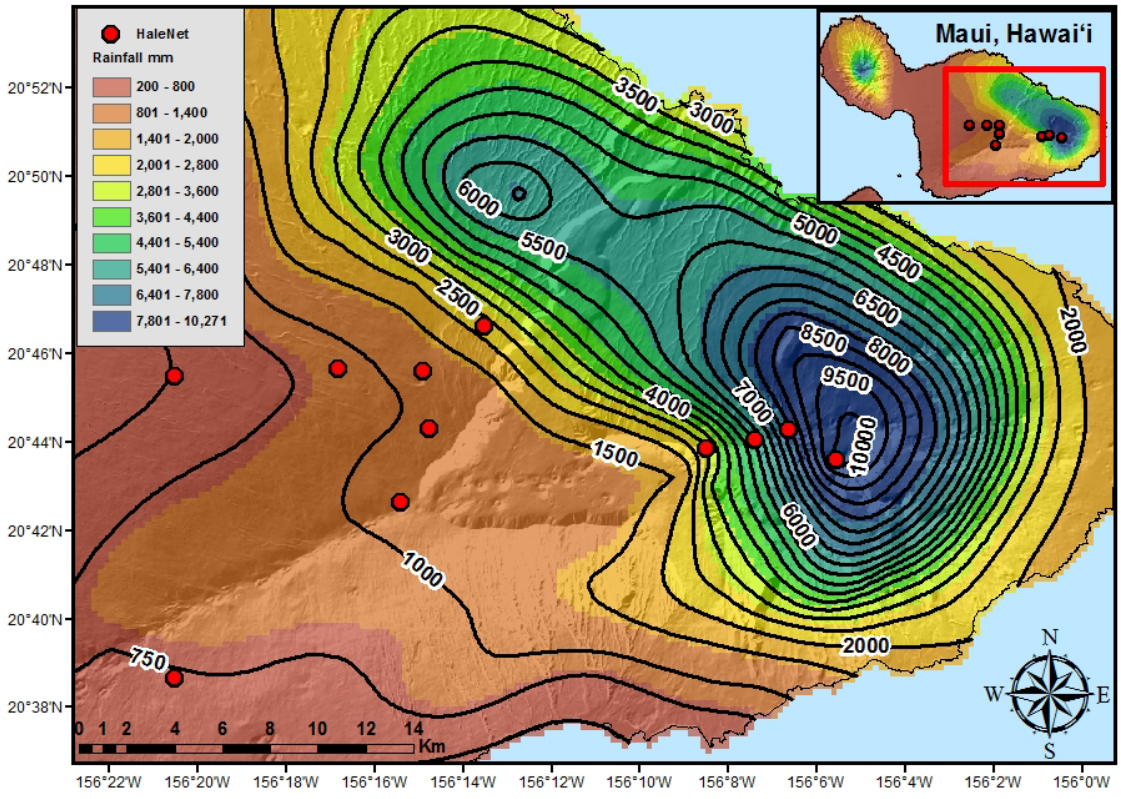

Figure 3: East Maui Annual Rainfall.

Orographic lifting is a major determinant of rainfall (precipitation) throughout the year in Hawai‘i and the processes that produce orographic cloud precipitation on the windward and leeward sides of the island are separate from one another. On the windward side of the island, trade winds push moist air up the eastern slopes of the mountain, cooling air to the dew point, causing water vapor to condense, forming clouds. The trade winds are present between 85 – 95% of the time in the summer and 50 – 80% in the winter (Sanderson, 1993). The strong persistence of the winds in the summer can be explained by the semi-permanent subtropical high-pressure anti-cyclone that sits to the northeast of the island chain (Gerza et al., 2012). The upper part of

Haleakalā extends above the TWI, which forces the trade winds around rather than over it (Leopold, 1949). Clouds from the windward side of the island do not reach the leeward side under normal trade wind conditions (Scholl et al., 2007). Instead a diurnal land/sea breeze pattern causes an anabatic movement of air up leeward slopes creating a cloud zone from about 1240 to 1800 m (Giambelluca and Nullet, 1991). However, this process is not sufficient to produce consistent convective showers (Leopold, 1949), therefore leeward slopes are generally dry. During the winter months, the semi-permanent anticyclone is weakened, and the trade winds are frequently interrupted by synoptic disturbances such as upper level troughs, frontal systems, and Kona storms (Giambelluca and Schroeder, 1998;Tu and Chen, 2011). A majority of the annual leeward precipitation is received as a result of these disturbances (Giambelluca and Schroeder, 1998). Cloud patterns are therefore explained by several factors including time of day, time of year, exposure to the trade winds and proximity to the TWI base (Figure 4).

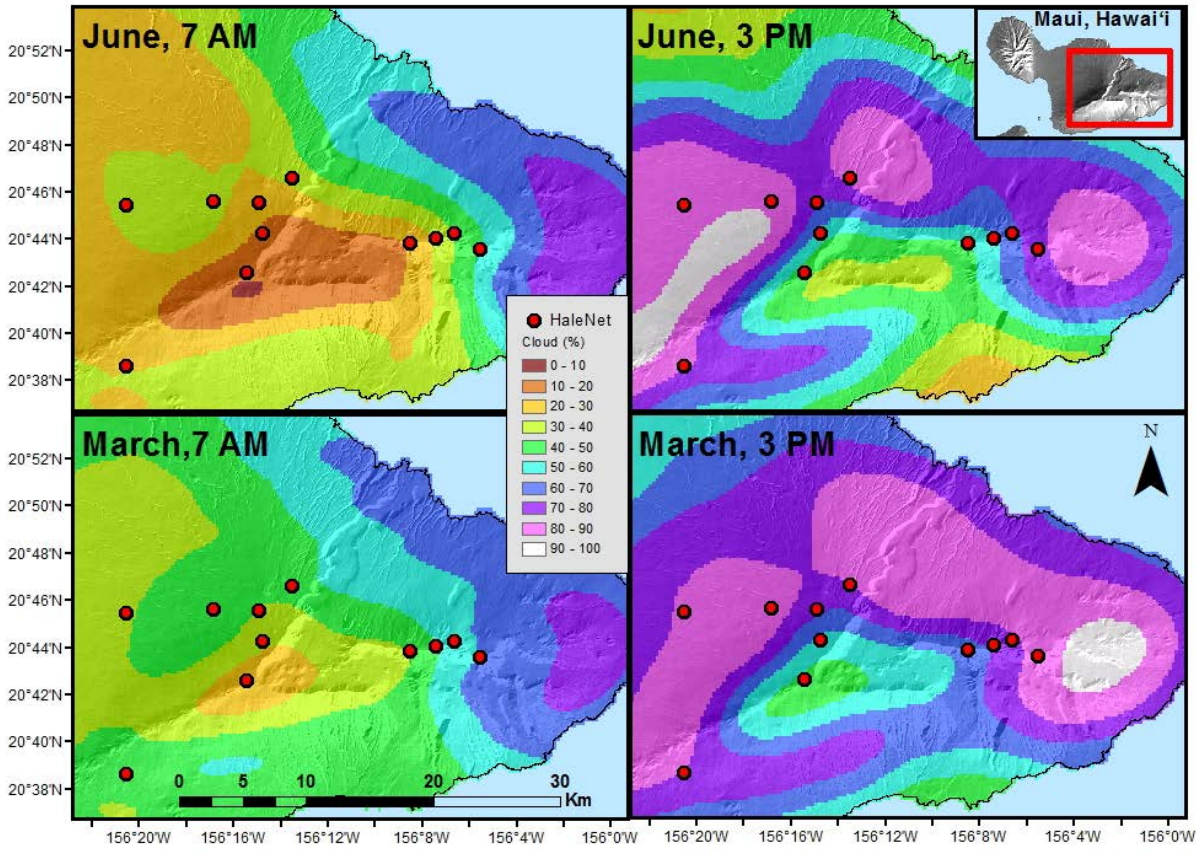

Figure 4: Cloud climatology of Haleakalā Volcano for June (top) and March (bottom) at 7 AM HST (left) and 3 PM HST (right).

The climate of Hawai‘i is strongly affected by the Pacific-centered coupled ocean-atmosphere phases of the El Niño Southern Oscillation (ENSO) and the Pacific Decadal Oscillation (PDO; Diaz and Giambelluca, 2012). Both ENSO and PDO are naturally occurring fluctuations in Pacific sea surface temperature (SST). ENSO phases recur on periods of 2 – 7 years and strongly influence winter rainfall patterns in Hawai‘i, where the positive phase (La Niña) is associated with wet conditions and the negative phase (El Niño) is associated with the dry conditions across the State (Chu and Chen, 2005). The patterns associated with positive (negative) phase of the PDO are similar to positive (negative) phase of ENSO, however the PDO signals fluctuate over longer (~20 yr) time periods (Chu and Chen, 2005).

Climatic zones on the slopes of Haleakalā can be characterized with reference to four atmospheric layers described by Riehl et al. (1951). These 4 climate zones with the corresponding atmospheric layers in parentheses are: 1) *marine* (sub-cloud), 2) *fog* (cloud), 3) *transitional* (inversion), and 4) *arid* (free atmosphere). The sub-cloud layer extends from sea level to the lifting condensation level (LCL, ~400 to ~1000 m; Diaz et al., 2011) at which point clouds begin to develop. Typically the LCL is higher on the leeward side due to additional heating of air in its longer trajectory across the land surface. The cloud layer exists from the LCL to the base of the TWI which can lie anywhere between 960 to 4200 m (Cao et al., 2007). The thickness of the inversion is variable (282 m ±281 m s.d.; Cao et al., 2007) and above this point the stable dry air of the free atmosphere can be found. The height and thickness of the TWI varies in space and time in response to fluctuations in large-scale circulation and surface heating (Giambelluca and Nullet, 1991). This layered system disappears when cyclonic systems disrupt the trade winds and Hadley Cell subsidence.

The vegetation characteristics across elevation gradients on both the windward and leeward orientations of Haleakalā are dependent on several factors, including substrate, topography, precipitation, available genotypes and the fragmentation and severe modification of native vegetation, especially at lower elevations (Medeiros et al. 1986). The northern and northeastern exposures of windward Haleakalā are subject to persistent orographic rainfall throughout the year. The tropical montane cloud forests (TMCFs) found within the fog zone on these slopes are dominated by the native species *Metrosideros polymorpha* (‘ōhi‘a lehua). The upper reaches of the cloud forests have resisted the invasion of alien species and native species have been shown to recover rapidly after the removal of feral ungulates (Loope et al., 1992).

Above the cloud zone an abrupt change in physiognomy and species composition of the vegetation occurs in the vicinity of the mean TWI, where the rain forest transitions to grassland and shrubland (Kitayama, and Mueller–Dombois, 1992). This abrupt transition in vegetation at the cloud zones upper limit (forest line) is linked to the TWI's pronounced discontinuity in moisture availability (Crausbay and Hotchkiss, 2010).

High-elevation wetland systems are also present on the windward side of the mountain. There are several bogs found along the northeast volcanic rift between 1450 and 2270 m elevation (Loope et al., 1991) and two high-elevation lakes found at 2040 m (Wai'ele'ele) and 2100 m (Wai'ānapanapa) (Crausbay and Hotchkiss, 2012). These wetland ecosystems contain a relatively large number of rare species some of which are endemic to the island of Maui.

The presence of clouds has profound effects on the biota within the TMCFs (Delay and Giambelluca, 2010). Cloud droplets are intercepted by leaves, stems and other obstacles within the forest system, adding to soil moisture on both windward and leeward sides of the mountain (Giambelluca et al., 2011). The leeward cloud zone was once extensively dominated by *Acacia koa* and *Metrosideros polymorpha,* much of which has been degraded to grassland by fire and browsing by feral goats and cattle (Medeiros et al., 1986).

A subalpine shrub land zone occurs from ~1800 to ~2400 m, dominated by *Coprosma montana, Sophora chrysophylla,* L*eptecophylla tameiameiae* and *Vaccinium reticulatum*; above ~2400 m, in an alpine zone, vegetation is sparse due to the combination of harsh climatic and edaphic conditions (Medeiros et al., 1986). The alpine zone is the habitat for the endemic Haleakalā silversword, (*Argyroxiphium sandwicense* subsp. *macrocephalum*), which grows on cinder cones, flats, and rocky cliffs in an area spanning the central to western portions of the crater and up to the summit from 2150 to 3000 m elevation (Krushelnycky et al., 2013; see section 8.5). Mean annual rainfall within this zone varies from 1090 to 1520 mm yr -1 (Giambelluca et al., 2013) with large diurnal temperature fluctuations with potentially freezing conditions at night and frequent high daytime temperatures (Loope et al., 1992). Early Hawaiian settlers did not use these high-elevation lands extensively, most likely because of the extreme conditions found there (Burney et al., 1995).

2.2 The HaleNet Climate Network

High mountains such as Haleakalā Volcano provide a natural laboratory for the study of elevation effects on tropical climate (Giambelluca and Nullet, 1991). Climate variables such as temperature, relative humidity, and precipitation exhibit impressive changes across relatively short distances along the slopes of the mountain. In July of 1983 a climate monitoring network (MauiNet) was established by the University of Hawai‘i College of Tropical Agriculture to support a variety of agricultural research projects. The network consisted of 23 stations ranging from 40 to 1640 m in elevation on the northwest flank of Haleakalā Volcano. MauiNet measurements included solar radiation, temperature, and relative humidity and, at some sites, rainfall, soil temperature and moisture and wind speed. MauiNet was operated by Haruyoshi Ikawa of Department of Agronomy and Soil Science until about 1989.

In June of 1988 the beginnings of the HaleNet climate network were established on the leeward slopes of Haleakalā Volcano with the installation of three climate measurement stations. Two climate monitoring stations were collocated with MauiNet sites HN-119 (960 m) and HN-106 (1640 m) and a third station HN-151 (2120) was installed near the Haleakalā National Park Headquarters (Table 2). This leeward transect of HaleNet stations was expanded further up the mountain in March 1990 with the addition of HN-152 (2590 m) and a summit station HN-153 (2990 m). In June 1992 stations HN-164(1650 m), HN-163(1960 m), HN-162(2260 m) and HN-161(2460 m) were installed along a second elevation transect located on the windward side of the island. These windward stations are all located in remote areas, making access to them difficult without the aid of helicopter transportation. In December 2000, an additional leeward station (HN-141) was installed at 1240 m elevation on the southwest rift of Haleakalā Volcano. In August 2001, a windward station (HN-142) was installed in The Nature Conservancy Waikamoi Preserve located in the upper Pi‘ina‘au stream drainage basin at 1932 m. Of the eleven stations that once operated in the HaleNet climate network eight are still in full operation. The Waikamoi station (HN-142), which was installed for a research project on cloud water interception, was removed in August 2003. The Horseshoe Pu`u station (HN-163) at 1960 m elevation was discontinued after being badly damaged by lightning and high winds in 1996. The Pu`u Pahu station (HN-106) at 1650 m elevation was vandalized in 2003 and now only collects rainfall data. The entire network has a vertical coverage 810 m (1650 – 2460 m) and 2030 m (960 – 2990 m) along the windward and leeward slopes respectively (Figure 5).

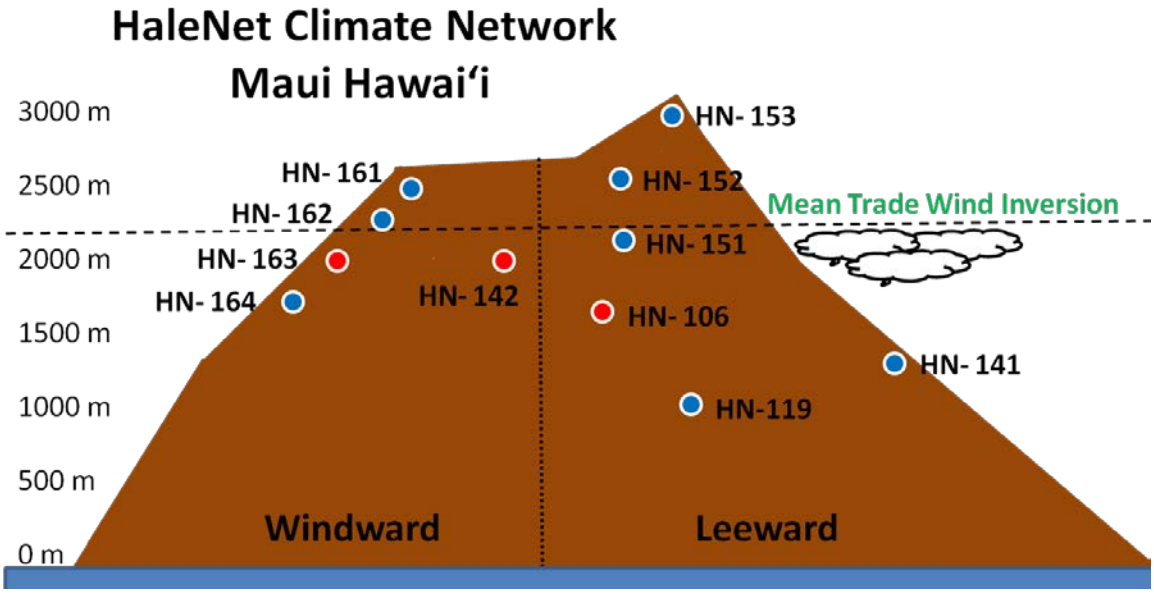

Figure 5: Vertical profile of the HaleNet climate network. Horizontal orientation of the stations and island topography are not to scale; blue dots indicate stations that are in full operation; red dots indicate stations that are in partial operation or not operating.

Table 2: HaleNet climate network station metadata.

ID #	Station Name	Elev (m)	Exposure	Albedo	Press (mb)	Lattitude	Longitude	Start Date	End Date	Land Cover Type
HN-119	Kula Ag	960	leeward	0.19	905	20.761	156.323	Jun-88	-	grass
HN-141	Auwahi	1240	leeward	0.14	875	20.648	156.345	Dec-00	-	dryland forest
HN-106	Pu'u Paha	1640	leeward	0.13	835	20.761	156.280	Jun-88	Oct-03	pasture
HN-164	Big Bog	1650	windward	0.13	834	20.730	156.095	Jun-92	-	montane wetland
HN-163	Horseshoe Pu'u	1930	windward	0.13	807	20.738	156.111	Jun-92	Nov-96	cloud forest
HN-142	Waikamoi	1960	windward	0.14	804	20.777	156.225	Aug-01	Aug-03	cloud forest
HN-151	Park HQ	2190	leeward	0.07	789	20.763	156.251	Jun-88	-	shrub, basaltic outcrop
HN-162	Tree Line	2260	windward	0.13	834	20.737	156.127	Jun-92	-	cloud forest, forest line
HN-161	Pohaku Palaha	2460	windward	0.13	758	20.734	156.143	Jun-92	-	shrub, basaltic outcrop
HN-152	Nene Nest	2590	leeward	0.10	747	20.741	156.249	Mar-90	-	cinder, sparse grass, fern
HN-153	Summit	2990	leeward	0.05	713	20.714	156.259	Mar-90	-	cinder, sparse grass, fern

HaleNet stations have been recording microclimatic data for as long as ~27 years (Table 2). The data collected at these stations include measurements of net and solar radiation, temperature, wind speed and direction, relative humidity, precipitation, soil temperature, soil heat flux, and soil moisture. More recent upgrades to the stations still in full operation have been the addition of 4-component net radiometers, which provide measurements of downward and upward longwave and shortwave radiation. All of these climate variables can be analyzed independently or in combination to derive additional variables such as potential evapotranspiration.

The stations within the HaleNet network provide data relevant to the four atmospheric layers described by Riehl (1951). These layers can be delineated according to levels of the cloud base and the TWI base, both of which can vary through space (vertical and horizontal) and time (e.g., dry season vs. wet season). The marine (sub-cloud) zone which extends from sea level to the mean cloud base level, ~1000 m on the leeward slope, is best represented by station HN-119 (960 m). Air in this layer is well mixed with temperature and relative humidity profiles strongly influenced by upwind sea surface conditions.

The fog (cloud) zone, which extends from the mean cloud base level to lower limit of the TWI, is represented best by leeward stations HN-141 (1240 m), HN-106 (1640 m) and windward station HN-164 (1650 m). This zone experiences frequently cloudy conditions, which typically correspond to the low receipts of energy and high amounts of moisture on either transect. This zone is also influenced by the rapid upslope movement of moist air during the day and the frequent downward flow of dry air, which produces high variability in humidity and radiation.

The transition (inversion) zone covers a range of heights beginning at the TWI base height and extending through the inversion. Within this zone any of the four atmospheric layers can be present at a given time. Fluctuations in the inversion can produce rapid changes in relative humidity of 60% or more over a few minutes (Giambelluca and Nullet, 1991). HaleNet stations HN-151 (2120 m) on the leeward transect and HN-162 (2260) on the windward transect are most representative of this zone.

The arid (free atmosphere) zone extends above the upper limit of the inversion zone. The air found in this layer originates high in the troposphere and is very dry and relatively warm. This air is isolated from ocean moisture when the TWI is present making it relatively cloud free. The upper slopes of Haleakalā, which penetrate into the arid zone, are exposed to high levels of radiation and low rainfall amounts. HaleNet stations HN-152 (2590 m) and HN-153 (2990 m) on the leeward slope and HN-161 (2460 m) on the windward slope most effectively capture the characteristics of the free atmosphere zone. When the TWI is absent or the base height is above 3000 m moist air originating from lower elevations can reach all of these stations.

3. Methods

3.1 Data Quality and Control

HaleNet data used in this report were subjected to a series of quality control and quality assurance procedures before they were made available for analyses. First, all the data were plotted as a time series and visually screened for outliers and unrealistic consecutive values (e.g. air temperature drops from 28˚ to 9˚ in one hour). Second, the relationships between variables that are highly correlated were compared (e.g. solar radiation and net radiation). Third, variable data were compared between nearby stations. To improve the overall accuracy and homogeneity of the HaleNet data, a series of error detection, correction, and homogenization techniques were developed for some of the measured variables. Application of these techniques was necessary to correct for the effects of instrument calibration drift and the abrupt data shifts resulting from adjustment of data logger coefficients following sensor recalibration. Note: a general description of the instrumentation used to measure climate variables at each HaleNet stations is found in Table 3.

Table 3: General description of the type of instrumentation used to monitor climate variables at the HaleNet stations and approximate instrument installation date.

Variable	Jun-88	Jul-99	Jan-11
Solar radiation	Eppley, 8-48		Hukseflux NRO1
Net radiation	REBS, Q*6 or Q*7	REBS Q*7	Hukseflux NRO1
Air temperature	Yaisala, HMD-30-YB	Vaisala, HMP-45-C	
Relative humidity	Vaisala, HMD-30-YB	Vaisala, HMP-45-C	
Wind Speed	Qualimetrics, 2011	Met One, 034A	R.M. Young 05106
Soil moisture		Campbell, CS615/CS616	
Soil Heat		REBS, HFT-3	
Data Logger	LI-COR, LI-1000	Campbell, CR10X	Campbell, CR3000

Data for all variables were sampled at 10 second intervals and averaged for the hour. Note: These instrumentation and replacement timeline reflect changes that occurred at a majority of HaleNet stations and this table should be interpreted as a general description.

For solar radiation (K_d) measurements, a method was developed to homogenize hourly K_d time series based on comparison of clear-sky radiation observations against estimates derived from a clear-sky radiation model. In-homogeneities in the record are identified based on shifts in pyranometer response in relation to the model estimates, and corrected to produce a

homogeneous time series. A detailed description of this method is given in Longman et al. (2013).

Net radiation (R_n) data were corrected and homogenized using several methods. First the data were corrected using a procedure that adjusted data obtained from early versions of the REBS net radiometers Q*6 and Q*7, to be consistent with the sensor calibration approach recommended by the manufacturer beginning with model Q*7.1. This correction involved the use of separate calibration factors for positive (daytime) and negative (nighttime) values, and a wind correction. If no wind speed value was available for a given time period, the mean station wind speed was used for the correction. Finally, the R_n data were homogenized so that values obtained from the different sensors that were in place over the period of record were in agreement with one another. To accomplish this, the hourly R_n/K_d ratio was used to identify inconsistencies within a given data set by examining how this ratio changed over time. The principle behind the adjustment is that the R_n/K_d ratio should be consistent over time and any apparent shifts or trends indicate a change in the sensor. R_n data can then be corrected based on the relationship between R_n/K_d ratios for a given time period and the R_n/K_d ratios obtained during a reference period. The mean ratio from the time period when recently installed Hukseflux net radiometers were in place was used as the R_n/K_d ratio reference period. All other time periods were corrected based on this value. The adjustments were checked by comparing adjusted REBS sensor data with Hukseflux data for a time period when both sensors operated at each site simultaneously. Based on this comparison, it was conclude that adjusted daytime radiation values were in close agreement with the reference data. However, adjusted nighttime (negative) Rn values were not in agreement with the reference data. Therefore, a simple adjustment of nighttime values was applied based on comparison of the new and old sensors during the period of overlapping observations.

An assessment of wind speed data revealed several homogenization issues: 1) sensors installed at different heights during the period of record; 2) changes in the low-wind threshold due to the degradation of the instruments bearings; and 3) changes in sensor type. These issues were addressed by: 1) adjusting wind speed to a common sensor height based on an assumed logarithmic profile, setting zero plane displacement and roughness length as a function of the vegetation height (e.g. Thomas et al., 2005) and 2) identifying and correcting data affected by worn bearings in the anemometer. After adjusting for sensor height differences, each station time

series was divided into two groups representing periods during which instrument bearings were assumed to be good (reference data) and periods when the bearings appeared to have been faulty. The bad-bearing periods were identified as periods with repeated cases of zero as the recorded wind speed. Experience shows that completely calm conditions are very rare at all stations. The end of these bad-bearing periods almost always coincided with the replacement of the bearings or sensor as indicated in the field notes. Using rank regression, parameter values for the Weibull distribution were determined based on the reference data set. Data were then adjusted for bad-bearing periods, by setting the wind speed at each time interval according to its cumulative frequency, using the inverse Weibull cumulative frequency function with settings from the reference data set. For intervals with measured zero wind speed (which have indistinguishable cumulative frequencies), the order of the Weibull-generated values was randomized before cumulative frequencies were assigned. Comparison of frequency distributions for reference bad-bearing periods showed that only the lower wind speed measurements are significantly affected by the bearing degradation. Therefore, only wind speeds less than 1.5 m s^{-1} were corrected using this method.

An assessment of relative humidity data from the HaleNet stations revealed several problems related to calibration drift. Fortunately, HaleNet stations experience saturated conditions (RH = 100%) more or less frequently, and these periods can be used as reference points to correct the calibration drift. First, the data were examined at each station during periods when the sensor calibration was thought to be accurate to establish the length of the time window needed to provide a high confidence in the occurrence of saturated conditions at the site. The length of the required time window ranged from 6 (HN station 164) to 60 (HN station 153) days. Maximum measured relative humidity was identified using a moving window that encompassed of the appropriate length for each station. Data with calibration drift errors were adjusted according to the following equation:

$$\mathrm{RH_{adj}} = \mathrm{RH} * \left(\frac{100}{\mathrm{RH_{max}}}\right) \quad (1)$$

where: $\mathrm{RH_{adj}}$ is the adjusted hourly relative humidity, RH is the measured hourly relative humidity, and $\mathrm{RH_{max}}$ is the maximum hourly value within the current time window. Each adjusted time series was graphed and visually checked. Rainfall at each station was graphed alongside the RH time series to provide additional information useful in conducting the visual consistency check.

3.2Derived Variables

3.2.1 Potential Evapotranspiration

Potential Evapotranspiration (PET) can be defined as the rate at which a vegetated surface, not limited by moisture availability, loses water to the atmosphere (Dunne and Leapold, 1978). Several methods have been developed to calculate PET (e.g. Penman, 1948; Thornthwaite 1948; Priestley and Taylor, 1972); however the Penman-Monteith (Monteith, 1965) method is recommended by the FAO for calculating PET whenever the required input data are available (Gong et al., 2006). The Penman-Monteith method requires measurements of air temperature, wind speed, relative humidity and net radiation. This method also includes a thermodynamic (energy required to evaporate water) and aerodynamic (the turbulent transport of water vapor away from the evaporating surface), component that accounts for the effects of vegetation on thermodynamic and aerodynamic processes (Howell and Evett, 2004; Bonan, 2008;). This method was used to calculate PET (mm hr^{-1}) at 8 HaleNet stations where sufficient data were available. The Penman-Monteith equation can be expressed as:

$$\lambda E = \frac{\Delta(R_n - G) + \frac{\rho C_p}{r_a}(e_*[T_a] - e_a)}{\Delta + \gamma} \quad (2)$$

where λE is the evaporation expressed as a latent heat flux (W m^{-2}), Δ is the slope of the saturation vapor pressure versus temperature curve (kPa $°C^{-1}$), R_n the net radiation flux density at the surface (W m^{-2}), G the sensible heat flux density from the surface to the soil (assumed to be negligible over a 24-hr period), ρ is the density of air (kg m^{-3}), C_p the specific heat of moist air at constant pressure (1004 J kg^{-1} K^{-1}), $e_*[T_a]$ is the saturation vapor pressure (kPa) at ambient air temperature (T_a, °C), e_a is the actual vapor pressure of the air (kPa), r_a is the aerodynamic resistance to turbulent heat and/or vapor transfer from the surface to the reference height (z) above the surface [s m^{-1}], γ is the pyschrometric constant (kPa $°C^{-1}$).

The resistance to transfer of heat and water vapor from the evaporating surface into the air above is represented by the aerodynamic resistance term, estimated here using the following relationship (Allen et al., 1998):

$$r_a = \frac{\left[\ln\left(\frac{(z_a - ZPD)}{z_0}\right)\right]^2}{k^2 U_Z} \quad (3)$$

where z_a is the height of wind measurements (m), ZPD zero plane displacement height (m), z_0 is the roughness length governing momentum transfer of heat and vapor [m], k is the von Karman's constant, 0.41, u_z is the wind speed at height z (m s^{-1}). To provide reference-surface PET estimates, the terms ZPD and z_0 were held constant at all of the stations at values of 0.1005 and 0.015 respectively, which are representative of a short grass cover.

3.2.2 Vapor Pressure Deficit

Saturation vapor pressure can be defined as the equilibrium vapor pressure under the existing environmental conditions of temperature (Murray, 1967). Saturation vapor pressure increases non-linearly with higher temperature and can be expressed by a sixth-order polynomial developed by Lowe (1977);

$$e_* = \mathrm{A_0} + \mathrm{T_a}\left(\mathrm{A_1} + \mathrm{T_a}\left(\mathrm{A_2} + \mathrm{T_a}\left(\mathrm{A_3} + \mathrm{T_a}\left(\mathrm{A_4} + \mathrm{T_a}(\mathrm{A_5} + \mathrm{A_6}\mathrm{T_a})\right)\right)\right)\right) \quad (4)$$

where A_0 is 6.107800, A_1 is 4.436519E-1, A_2 is 1.428946E-2, A_3 is 2.650648E-4, A_4 is 3.031240E-6, A_5 is 2.034081E-8, A_6 is 6.136821E-11.

Vapor pressure is defined as the part of the total atmospheric pressure contributed by the ambient water vapor content. Vapor pressure can be derived from RH as:

$$e_\mathrm{a} = \mathrm{RH}\left(\frac{e_*}{100}\right) \quad (5)$$

where RH is the relative humidity.

The vapor pressure deficit (VPD) is the difference between the saturation vapor pressure and the actual vapor pressure:

$$\mathrm{VPD} = e_* - e_\mathrm{a} \quad (6)$$

VPD is an indication of the dryness of the air and the potential for evaporative fluxes.

3.2.3 Soil Heat Flux

The flux of sensible energy into or out of the soil (soil heat flux, G) is an important component of the surface energy balance especially in areas with sparse or no vegetation (Giambelluca et al., 2014). Spatial and temporal variations in G are driven by available energy at the surface, which is influenced by surface characteristics and atmospheric conditions. At each HaleNet station, G is estimated based on measurements from two soil heat flux transducers placed at a 8 cm depth and estimated changes in sensible heat stored in the soil above the transducers based on measurements of soil moisture and soil temperature:

$$G = F + S \quad (7)$$

where F is the average of soil heat flux at 8 cm and S is the change in sensible heat storage in the upper 8 cm soil layer:

$$S = \left(\frac{\Delta T_{Soil}}{TI}\right) D \left((\rho_b C_s) + \theta\, \rho_w\, C_w\right) \quad (8)$$

where ΔT_{soil} is the change in temperature in the upper 8 cm of soil from the previous hour (°C), TI is the time interval (s), D is the vertical thickness of the soil layer above the heat plate (m), ρ_b is the bulk density of the soil (kg m^{-3}), C_s is the specific heat for mineral soil (J kg^{-1} K^{-1}), θ is the volumetric soil moisture content (m^3 m^{-3}), ρ_w is the density of water (kg m^{-3}) and C_w is the specific heat of water (J kg^{-1} K^{-1}).

3.2.4 Cloud Attenuation of Sunlight

To determine the reduction of global radiation by clouds, measured global radiation values are compared to clear-sky estimates derived from the REST2 clear-sky radiation model (Gueymard, 2008). The two-band REST2 clear-sky radiation model (Gueymard, 2008) can predict instantaneous or short-term (hourly or sub-hourly) global radiation based on a limited number of inputs that describe the local and current, atmospheric and environmental conditions. Methods for parameterizing clear-sky radiation models, specifically in Hawai‘i, have been described elsewhere (Gueymard, 2012; Longman 2012). For this study, REST2 model inputs are held constant at their respective long-term means. In a previous study, we analyzed the effects of temporal averaging of model atmospheric transmission parameters (Longman et al. 2012). The results showed that holding model inputs constant at their mean annual value gave better results than using temporally varying (daily or monthly) parameter estimates for prediction of clear-sky radiation. The use of fixed input parameter values was also mandated for this study by the fact that measured atmospheric parameters were not available for the entire period of record.

To calculate the cloud attenuation of sunlight, mean hourly solar radiation for each month in the record was divided by the long-term mean REST2 modeled clear-sky solar radiation for the appropriate calendar month. This analysis was applied only to data between the hours of 9:00 AM and 5:00 PM (HST) to eliminate any topographical shading effects during times of low sun angles. The hourly percent of cloud attenuation of sunlight is expressed as:

$$CA = 100 - \left(\frac{Kd_h}{CS_h}\right) * 100 \quad (9)$$

Where, CA is the cloud attenuation of sunlight, Kd_h is measured hourly solar radiation and CS_h is the modeled clear-sky hourly solar radiation. Monthly means are calculated as the average of the eight mean hourly CA values for each month.

3.3 Data Aggregation and Temporal Assessment Methods

Hourly HaleNet data are aggregated in several ways. The period-of-record mean diurnal cycles are calculated for each month with at least 15 days of data by averaging the monthly mean hourly values. Mean monthly values are derived from the mean monthly diurnal cycles. The 6-month dry and wet season and annual means are calculated by averaging the appropriate mean monthly values. Dry and wet season aggregated values are used to show spatial patterns related to elevation along leeward and windward transects. Period-of-record trends are assessed using the seasonal anomalies. These anomalies were calculated as the average of the departure of each monthly value from the appropriate period-of-record monthly mean. Anomaly values were included for a given season-year only if at least 50% of the data were available.

Precipitation (rainfall) was aggregated as follows to avoid extreme biases associated with missing data in the temporal analysis:

$$p_{i,j} = \frac{p_{sum\_i,j}}{m_{i,j}} N_i \quad (10)$$

where $p_{i,j}$ is the monthly rainfall total, $p_{sum\_i,j}$ is the sum of daily rainfall for days with good data, $m_{i,j}$ is the number of observation days in a month, N_i is the number of days in the month, and the subscripts i and j stand for month and year, respectively. Monthly mean precipitation was calculated as:

$$P_{POR\_i} = \frac{P_{sum\_i}}{M_i} N_i \quad (11)$$

where P_{POR_i} is the period-of-record mean precipitation for month i, P_{sum_i} is the sum of precipitation for month i for all months with ≥ 15 days of data and M_i is the number of days with precipitation observations included in P_{sum_i}. Precipitation anomalies are calculated as:

$$P_{anom\_i,j} = p_{i,j} - P_{POR\_i} \quad (12)$$

where $P_{anom\_i,j}$ is the monthly precipitation anomaly for month i and year j. For months with ≥ 15 days of data, a zero precipitation statistic was calculated as:

$$ZP_{i,j} = \frac{NZP_{i,j}}{m_{i,j}} * 100 \quad (13)$$

where ZP = the percentage of days with zero precipitation in month i and year j, NZP is the number of days of good data with zero precipitation, and the subscripts i and j stand for month and year, respectively.

Period-of-record trends are characterized using the linear model function (lm) in the R open source statistical software. We measure statistical significance at the 90% significance level ($\alpha = 0.1$), using the null hypothesis that the trend is zero. Time series are assessed for the period of record for each variable at each station. Time series start dates vary with station (Table 1). Time series end dates are typically October 2013 with the exception the variables potential evapotranspiration and cloud attenuation of solar radiation (October 2011) at all stations and all variables at the HN-106 station (October 2003).

Period of record trends are assessed for each of the two seasons for all time series with $n \geq 15$ seasonal values. Following this criteria we exclude all of the time series from HN-106 (except for precipitation), HN-141, HN-142, HN-163, and all time series data of the derived soil heat flux and measured soil moisture. We express relative change in a given variable over the period of record as:

$$Trend_{X\_k} = \frac{b_{X\_k}}{X_{POR\_k}} * 100 \qquad (14)$$

where $Trend_{X\_k}$ is the period-of-record trend as a percentage of the mean for variable X and season k; b_{X_k} is the slope of the trend line derived from linear regression in per year units for variable X and season k; X_{POR_k} is the period-of-record mean of variable X and season k. In total, 10 climate variables obtained from data collected from as many as 8 HaleNet stations are analyzed for period-of-record change for both dry and wet seasons.

In addition to the analysis of HaleNet-derived climate variables we also analyze seasonal TWI base height and frequency of occurrence data over the period 1991to 2013. Atmospheric sounding data obtained from the Līhuʻe and Hilo rawinsonde stations in Hawaiʻi are used to determine TWI characteristics using methods described by Longman et al. (in review).

The linear model used in this analysis does not account for the effects of temporal autocorrelation. In a preliminary analysis, 128 climate variable time series were tested for temporal autocorrelation using the Durbin-Watson statistical test (Durbin and Watson, 1971). Of the 128 time series tested, 15 (11.7%) we significant at $\alpha = 0.05$ and 5 (3.9%) were significant at $\alpha = 0.01$ and no consistent patterns among stations or variables were identified. Based on these results it was decided to not include a temporal autocorrelation correction in the linear model.

4. Spatial and Temporal Assessment

The complete record of HaleNet data is analyzed and results are presented for each variable. A description of the HaleNet data with regards to the temporal (diurnal and annual) and spatial (elevation and exposure to the prevailing winds) behavior of seven observed and four derived variables is presented and discussed for all HaleNet stations where sufficient data are available. We analyze the mean annual cycle of each variable as well as the spatial and temporal characteristics of the 6-month dry and wet seasons. High-elevation stations are those located above 2000 m and mid-elevation stations are located between 900 and 2000 m (Table 2). Long-term trends are assessed only for the stations that were established by June 1992 and are currently still in operation (i.e. 8 stations).

4.1 Solar Radiation

The amount of solar radiation reaching the surface of the Earth is modulated by several factors including latitude, time of day, time of year, topography and the optical properties of the atmosphere. Latitude of a given location governs the angle at which the sun's rays strike the Earth and therefore the amount of solar radiation arriving at the surface at any point throughout the day. Near the equator, the sun is always high overhead at mid-day and the days and nights are nearly equal in length throughout the year. Since Haleakalā Volcano is located ~20°N of the equator, the annual day length cycle has a range of approximately 2.5 hours. The annual cycle of solar radiation for each HaleNet station is shown in Figure 6. The seasonal changes are related to day length changes, the annual march of solar declination affecting the angle of incidence of direct radiation, and variations in cloud cover characteristics. Differences among stations are due mainly to elevation effects on clear sky radiation (under clear skies, solar radiation increases with elevation as the optical thickness of atmosphere is reduced) and spatial differences in cloud cover. The annual peak of solar radiation occurs in June for the four highest-elevation stations located above the mean TWI level (2160 m) and in July for the five stations located at or below this point (Table 4). The minimum values occur in either November or December although the values for these months were very similar at all stations.

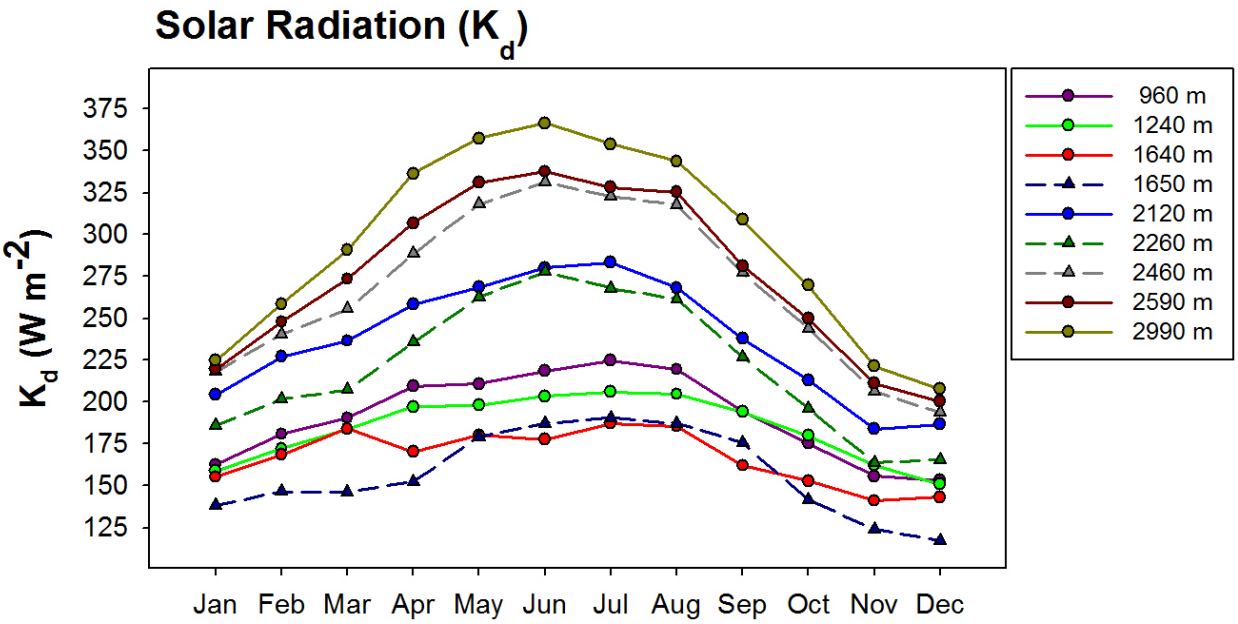

Figure 6: Mean annual cycle of solar radiation (K_d); solid lines with a circle marker indicate leeward stations; dashed lines with a triangle marker indicate windward stations.

Table 4: Mean annual cycle of solar radiation (W m^{-2}).

Sta ID	Elev	Jan	Feb	Mar	Apr	May	Jun	Jul	Aug	Sep	Oct	Nov	Dec	Annual	Dry	Wet
HN-119	960	163	181	191	210	211	219	225	220	195	175	156	153	191	207	175
HN-141	1240	159	172	184	197	198	203	206	205	194	180	162	151	184	198	171
HN-106	1640	155	169	184	170	180	178	187	185	162	153	141	143	167	174	160
HN-164	1650	138	147	146	153	179	187	191	187	176	142	124	117	157	177	138
HN-151	2120	205	227	237	259	269	280	283	268	238	213	184	187	237	259	216
HN-162	2260	186	202	207	236	263	278	268	262	227	196	164	166	221	249	193
HN-161	2460	218	241	256	289	318	331	323	318	277	244	206	194	268	302	234
HN-152	2590	220	248	274	307	331	338	328	326	281	250	211	200	276	309	243
HN-153	2990	225	259	291	337	357	367	354	344	309	270	221	208	295	333	257

Where monthly values (Jan-Dec) are the Period-of-record average monthly values for a period encompassing the start date of each station and an end date of October 2011. Annual is the twelve month average value, Dry is the May to October average value; Wet is the November to April average value; yellow highlighted squares indicate monthly maxima; blue highlighted squares indicate monthly minima.

The diurnal solar radiation patterns for the dry and wet seasons are shown in Figure 7. For all stations, solar radiation increases sharply in the morning with relatively little attenuation by clouds in both the dry and wet seasons (see Figure 4). For the highest elevation stations located at or above the mean TWI, solar radiation peaks at 12:00 or 13:00. This pattern is

indicative of generally clear conditions at these elevations throughout the day with slight increases in cloud cover in the afternoon hours (see Figure 4). At the mid-elevation stations, clouds that move progressively upslope during the day begin to reduce solar radiation significantly by late morning, especially for the leeward stations. The most notable change occurs within the cloud zone at leeward station HN-141(1240 m) where radiation is 30% lower at 13:00 PM than at 10:00 AM (Figure 7). Local sea-land and mountain-valley wind regimes can interact with the general trade wind flow and promote cloud development on the leeward side of the islands (Leopold, 1949). The presence of the TWI effectively caps the vertical development of clouds thus the highest-elevation stations show relatively cloud free conditions throughout the day. In both the dry and wet seasons cloud cover is consistently greater along the leeward transect in the afternoon hours (Figure 4).

For the mid-elevation station HN-164 (1650 m) on the windward exposure diurnal differences in cloud effects are not as clearly identifiable, which can be explained by the consistent presence of clouds throughout the day. Diurnal patterns for all stations are similar in the dry and wet seasons. However, less influence of clouds is seen during the wet season at mid-elevation leeward stations.

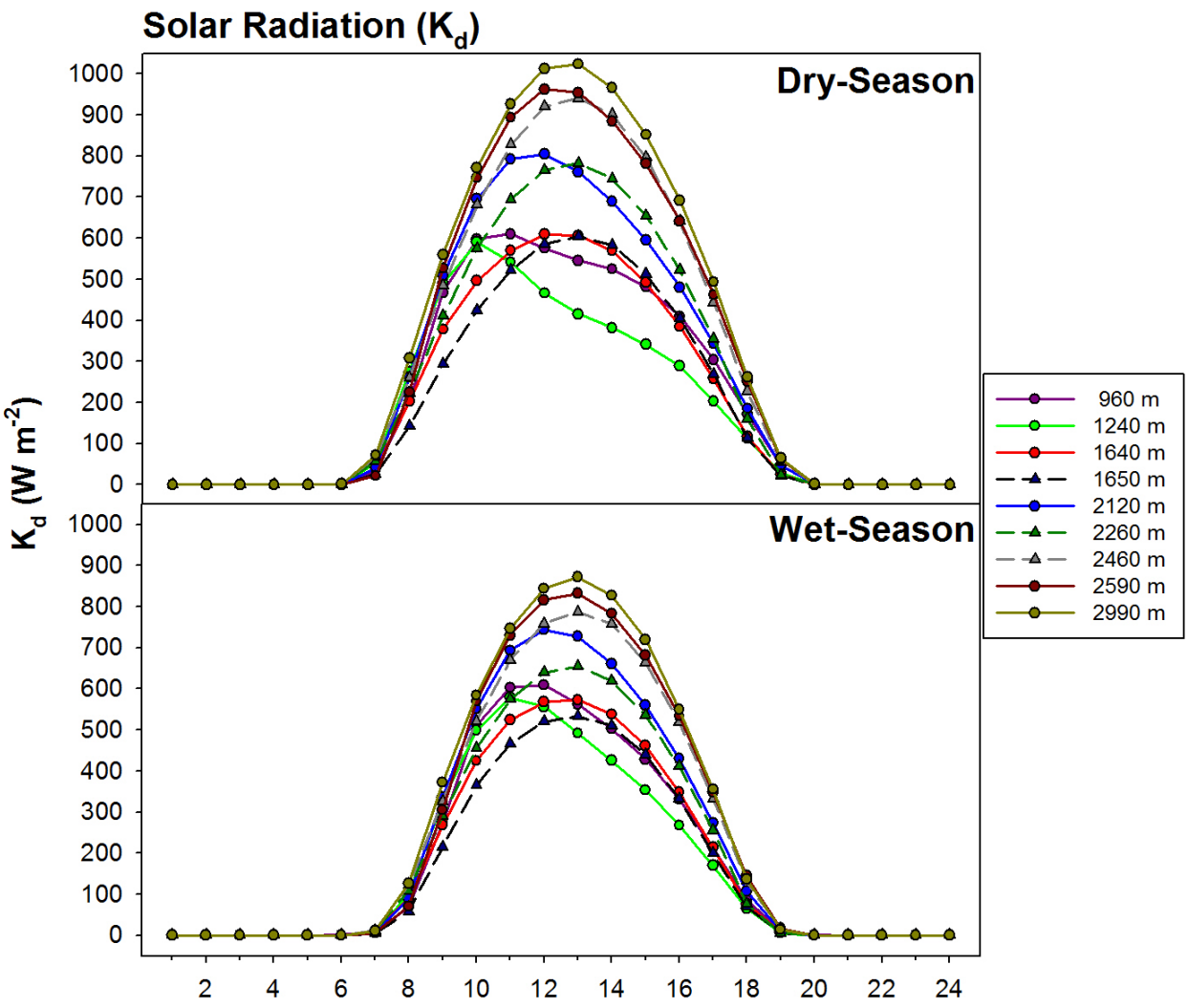

Figure 7: Diurnal cycles of solar radiation for the dry (top) and wet (bottom) season; solid lines with a circle marker indicate leeward stations; dashed lines with a triangle marker indicate windward stations.

The dry and wet season spatial profiles of solar radiation for 3 windward and 6 leeward stations are shown in Figure 8. Solar radiation gradients along the transects show similar patterns with a distinct minimum occurring in the center of the cloud zone ~1650 m and the highest irradiance occurring at the highest-elevation station along both transects. For the dry season, radiation at the highest station on each transect (2990 m and 2460 m for leeward and windward transects, respectively) is almost twice as much as the radiation measured within the cloud zone (Table 3). This contrast is much less pronounced in the wet season profiles.

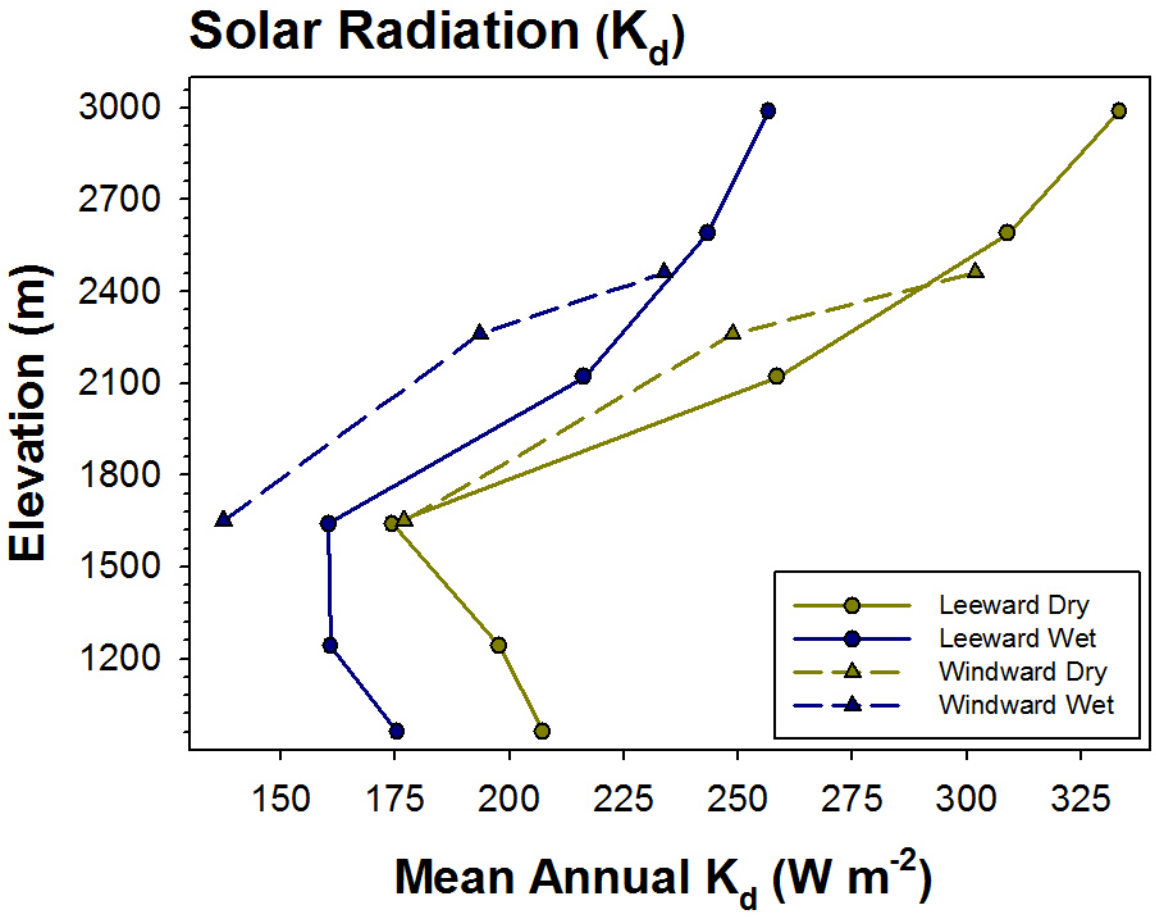

Figure 8: Vertical profiles of mean annual solar radiation along leeward (solid line, circle marker) and windward (dashed line, triangle marker) elevation transects for dry (yellow) and wet (blue) seasons.

4.2 Cloud Attenuation of Sunlight

Global solar radiation passing through the Earth's atmosphere is modulated by aerosols, trace gases and clouds. Because of Hawai'i's mid-oceanic location and distance from continental aerosol source areas, variability in atmospheric transmissivity is relatively low, especially in the free atmosphere above stations at high elevations (Longman et al., 2012). At the surface, clouds are the primary factor determining the attenuation of global radiation. Annually, the cloud attenuation of insolation (CA) can be as low as 4% at the summit and as high as 56% in the heart of the cloud zone all within the same month (Figure 9; Table 5). Annual CA minima (i.e. sparse cloud cover) occur between December and January for all but one of the leeward stations (2990 m). Despite being in the middle of the wet season these months have the lowest cloud cover frequency across the islands (Barnes, 2013). The timing of the highest mean monthly CA (i.e. abundant cloud cover) is more spatially variable. For mid-elevation leeward stations, maxima occur between April and June, which corresponds to the time of the highest TWI frequency and base height (Figure 2), thus promoting cloudy conditions at low elevations. For high-elevation leeward stations, the highest CA occurs between September and November, which is the transition period from the dry to wet season, a period of decreasing TWI frequency. Windward CA maxima occur in March and April, corresponding to some of the wettest months of the year at those locations (Giambelluca et al., 2013).

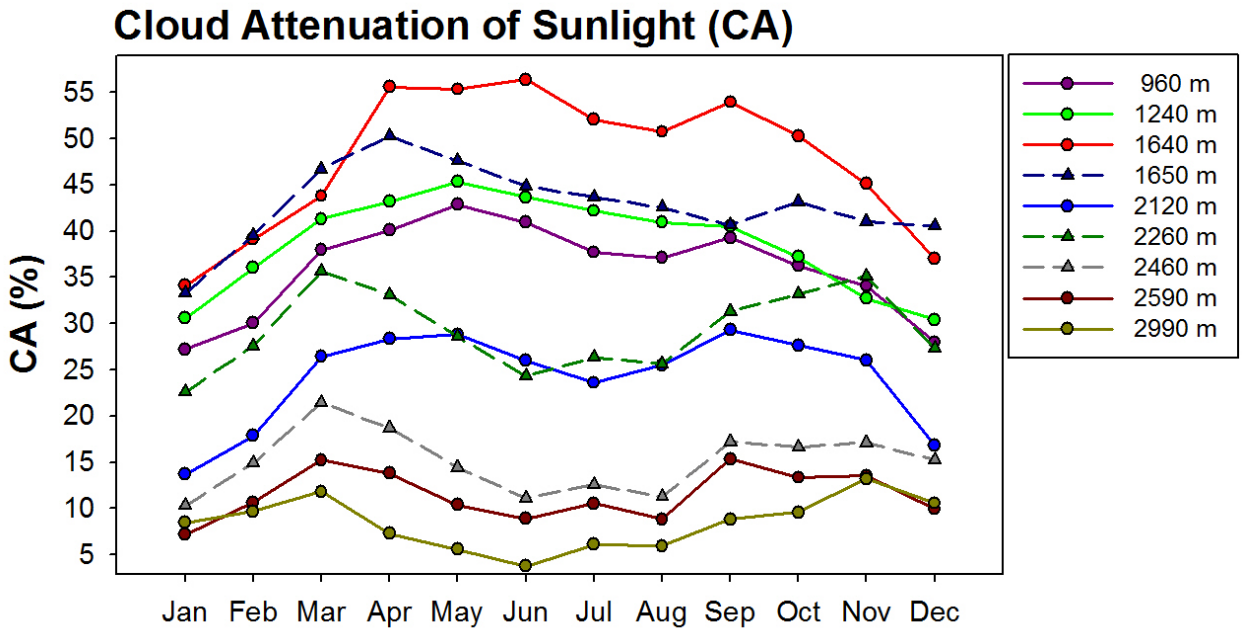

Figure 9: Mean annual cycle of daytime cloud attenuation of sunlight (CA); solid lines with a circle marker indicate leeward stations; dashed lines with a triangle marker indicate windward stations.

Table 5: Mean annual cycle of the cloud attenuation of sunlight (%).

Sta ID	Elev	Jan	Feb	Mar	Apr	May	Jun	Jul	Aug	Sep	Oct	Nov	Dec	Annual	Dry	Wet
HN-119	960	27.2	30.0	37.9	40.1	42.9	40.9	37.7	37.1	39.3	36.2	34.1	28.0	36.0	39.0	32.9
HN-141	1240	30.6	36.0	41.3	43.2	45.3	43.6	42.2	40.9	40.5	37.2	32.7	30.4	38.7	41.6	35.7
HN-106	1640	34.1	39.1	43.8	55.6	55.3	56.4	52.1	50.7	53.9	50.3	45.1	37.0	47.8	53.1	42.4
HN-164	1650	33.3	39.6	46.7	50.3	47.6	44.8	43.7	42.5	40.6	43.2	41.0	40.5	42.8	43.7	41.9
HN-151	2120	13.7	17.9	26.4	28.3	28.8	26.0	23.6	25.5	29.3	27.6	26.0	16.8	24.2	26.8	21.5
HN-162	2260	22.6	27.6	35.6	33.1	28.6	24.3	26.3	25.6	31.3	33.2	35.1	27.3	29.2	28.2	30.2
HN-161	2460	10.3	14.9	21.4	18.7	14.4	11.1	12.6	11.3	17.2	16.6	17.1	15.2	15.1	13.9	16.3
HN-152	2590	7.2	10.6	15.2	13.8	10.4	8.9	10.5	8.8	15.3	13.3	13.5	9.9	11.5	11.2	11.7
HN-153	2990	8.5	9.7	11.8	7.3	5.6	3.7	6.1	5.9	8.8	9.5	13.2	10.5	8.4	6.6	10.2

Diurnal profiles for the dry season (Figure 10) show a noticeable increase in afternoon cloud attenuation at all leeward stations with the greatest afternoon cloudiness occurring within the cloud zone (1640 m). Windward diurnal cycles are relatively constant throughout the day during both seasons. Wet season diurnal patterns are similar to those of the dry season; however, in general, much clearer conditions are observed throughout the day in the wet season. The influence of TWI frequency on cloud frequency is apparent during both the morning and afternoon hours. During the month of June (which has the highest TWI frequency of occurrence) the highest elevations show less cloud frequency than in the month of March (which has the

lowest TWI frequency of occurrence) during both the morning (7 AM) and afternoon (3 PM) hours (Figure 4).

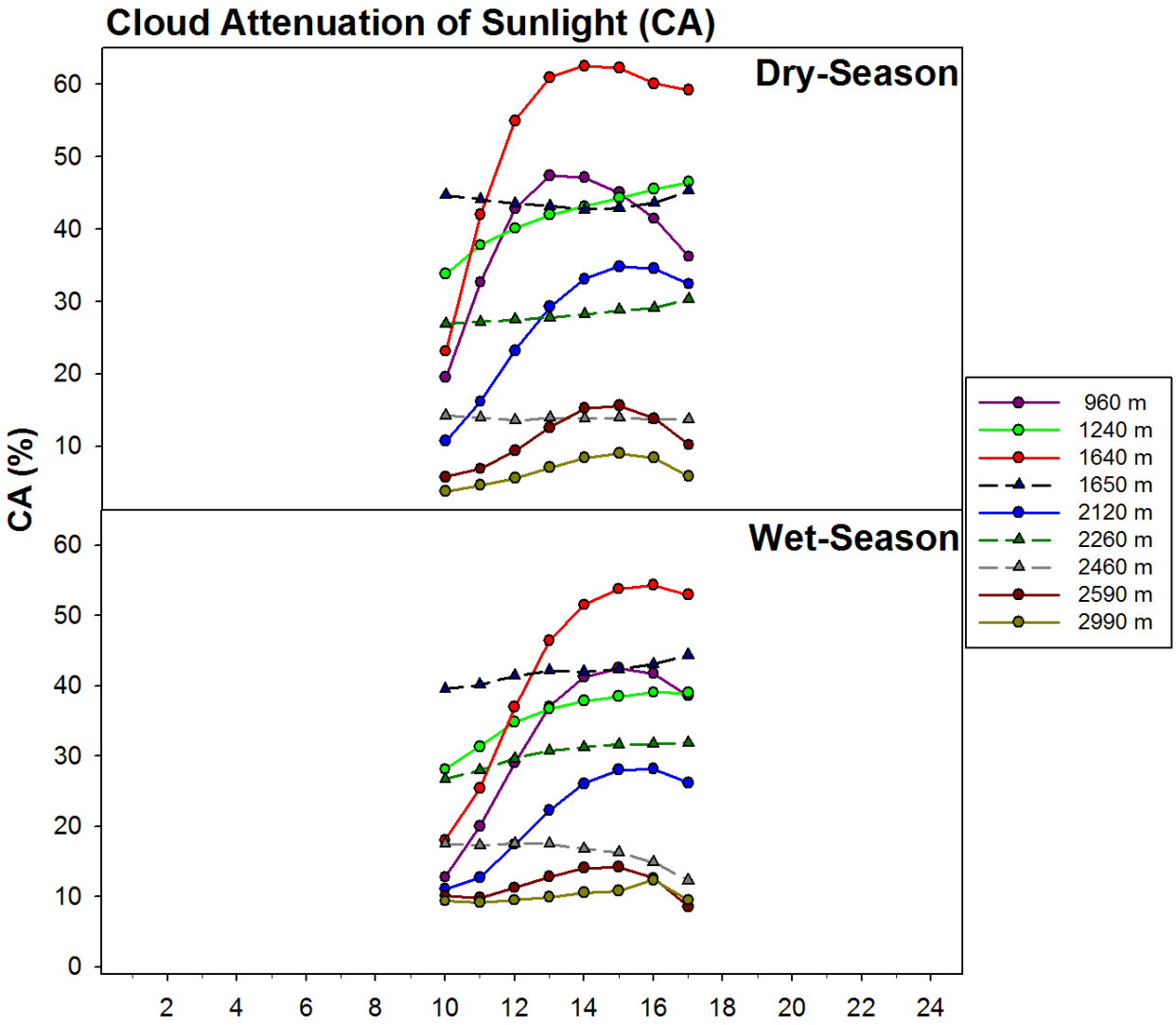

Figure 10**:** Diurnal cycles of cloud attenuation of sunlight for the dry (top) and wet (bottom) season; solid lines with a circle marker indicate leeward stations; dashed lines with a triangle marker indicate windward stations.

Vertical profiles of CA show the decreasing effects of cloud cover with elevation above the cloud zone (Figure 11). Between 1640 and 2990 m along the leeward transect cloud cover is reduced by 47 and 32% for the dry and wet seasons respectively. Along the windward transect decreases in cloud cover between 1650 and 2460 are 30 and 26% for dry and wet seasons, respectively.

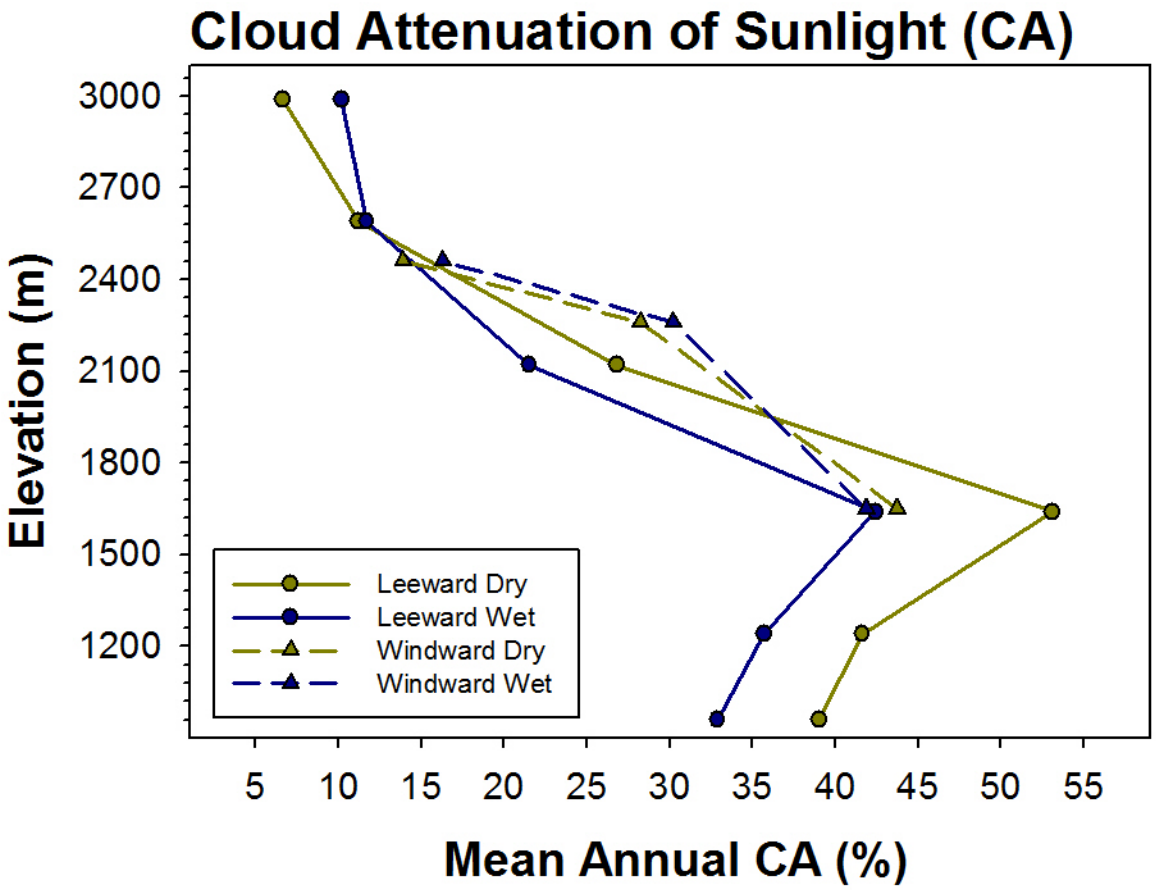

Figure 11: Vertical profiles of mean annual daytime cloud attenuation of sunlight, along leeward (solid line, circle marker) and windward (dashed line, triangle marker) elevation transects, or dry (yellow) and wet (blue) seasons.

4.3 Net Radiation

The difference between the absorbed and emitted radiation at all wavelengths is termed "Net Radiation" (R_n). At the surface, incoming (downward) shortwave (solar) and longwave (atmospheric) radiation add energy, while outgoing (upward) reflected shortwave and emitted longwave radiation remove energy. As a quantitative measure of the chief source of energy for all environmental processes, R_n is a fundamentally important variable in determining local climate and hydrological flows. R_n at the surface is used to heat the biomass, soil and overlying air and to evaporate water. Net radiation is positive during the day and negative at night, and generally higher during the summer than the winter. Across the globe, mean annual R_n is positive at low latitudes and negative at high latitudes. These variations in time and space drive the diurnal and annual cycles in climate and help explain the global distribution of climates. The same effects can be seen at the local scale, especially where extreme spatial gradients in radiation are found. Therefore, knowledge of the spatial and temporal variations in R_n is essential for understanding natural processes on Haleakalā.

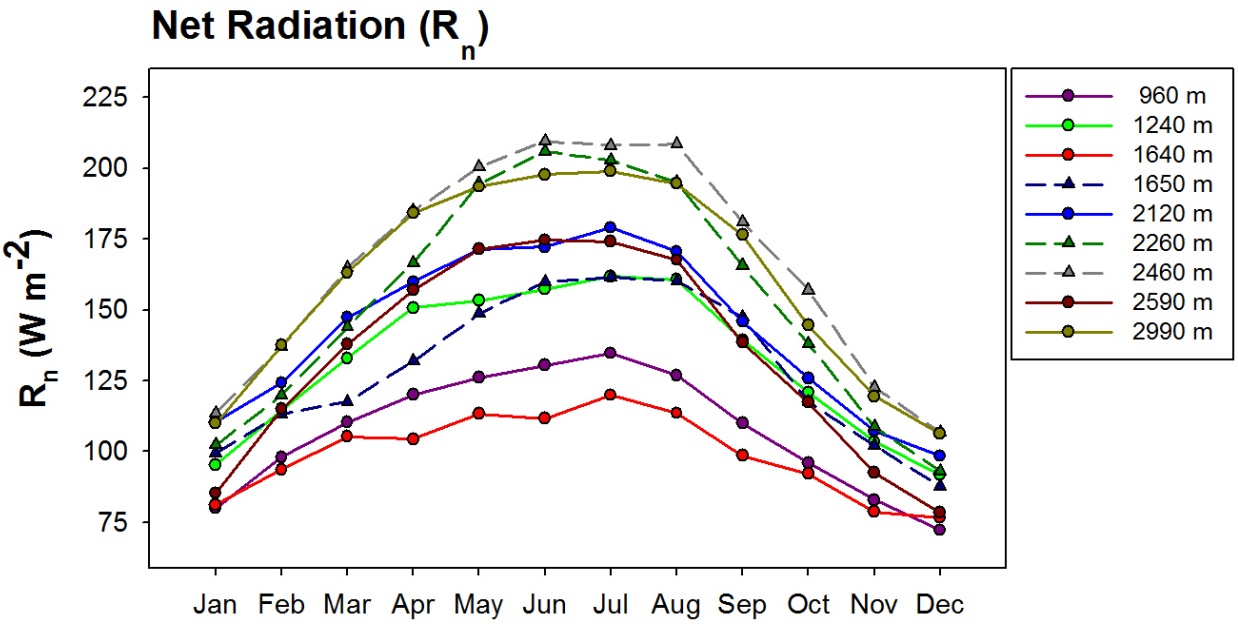

Figure 12: Mean annual cycle of net radiation (R_n); solid lines with a circle marker indicate leeward stations; dashed lines with a triangle marker indicate windward stations.

Table 6: Mean annual cycle of net radiation (W m^{-2}).

Sta ID	Elev	Jan	Feb	Mar	Apr	May	Jun	Jul	Aug	Sep	Oct	Nov	Dec	Annual	Dry	Wet
HN-119	960	80	98	110	120	126	130	135	127	110	96	83	72	107	121	94
HN-141	1240	95	115	133	151	153	157	162	161	139	121	104	92	132	149	115
HN-106	1640	81	94	105	104	113	112	120	114	99	92	79	77	99	108	90
HN-164	1650	100	113	118	132	149	160	162	160	147	118	102	88	129	149	109
HN-151	2120	110	124	147	160	171	172	179	171	146	126	107	98	143	161	125
HN-162	2260	102	120	144	167	195	206	203	195	166	138	109	93	153	184	122
HN-161	2460	114	137	165	185	200	209	208	208	181	157	123	107	166	194	138
HN-152	2590	85	115	138	157	171	175	174	168	139	117	93	79	134	157	111
HN-153	2990	110	138	163	184	193	198	199	195	176	145	119	106	161	184	137

The annual R_n peak for the HaleNet stations occurs in July at six stations and June at three stations (Figure 12; Table 6) although differences were very small between the two months (1 to 8 W m^{-2}). R_n minima occurred in December for all nine stations analyzed. The annual cycles of R_n follow those of the solar radiation cycles with the higher values occurring during the high-sun, dry season months and lower values occurring in the low-sun, wet season months.

The diurnal patterns of R_n for the dry and wet seasons resemble solar radiation patterns during the daylight hours (Figure 13). At night, longwave radiation loss to space increases with elevation along both transects, as indicated by the greater negative values. Mid-elevation sites

are often beneath a cloud layer that persists after dark. As a result, longwave radiation loss is reduced, but increases in the early morning hours as the sky begins to clear. For the high-elevation stations, which are typically above the cloud layer, longwave radiation tends to decrease throughout the night as the ground cools. In general, there is a much greater nighttime longwave radiation loss along the leeward transect.

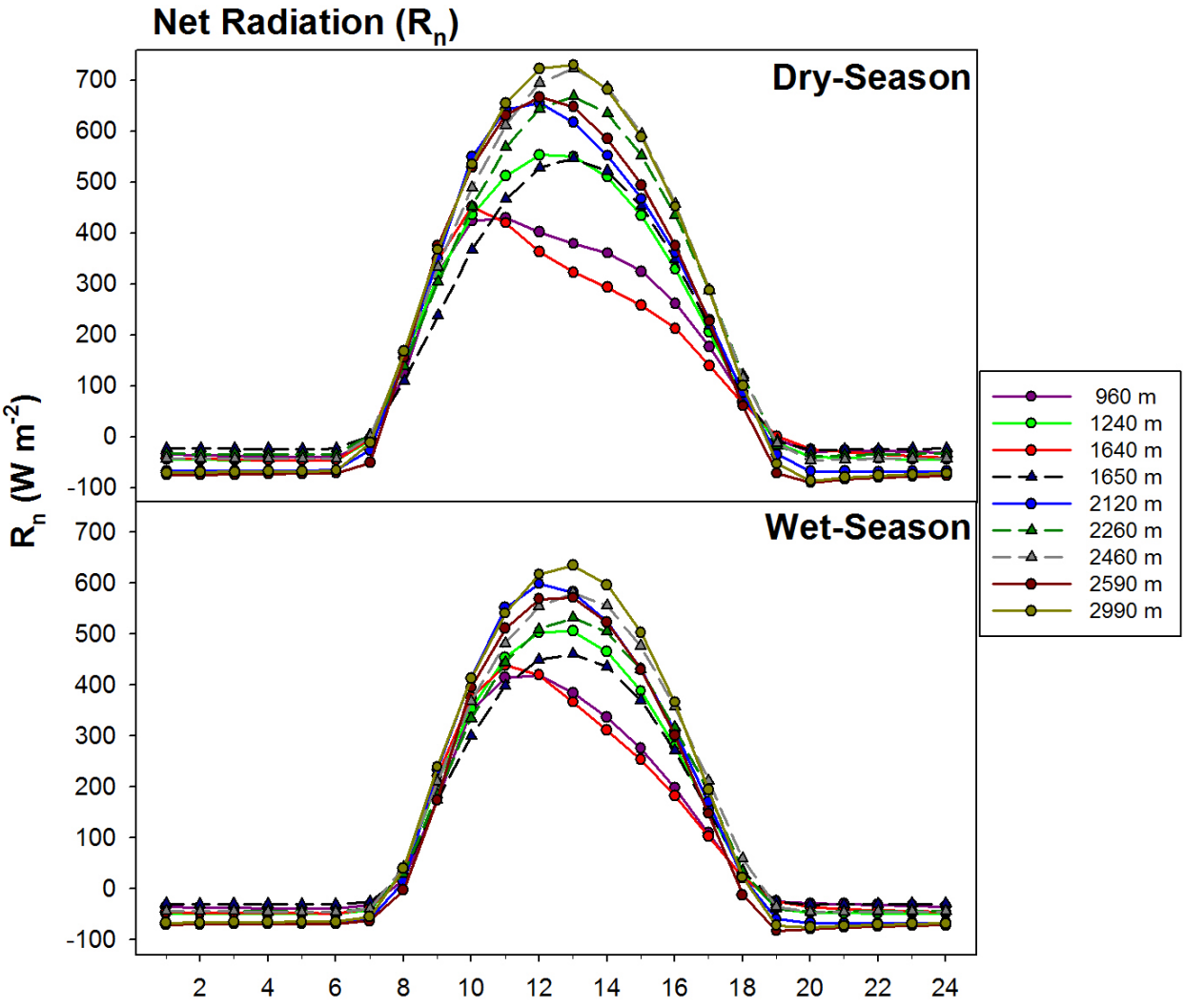

Figure 13: Diurnal cycles of net radiation for the dry (top) and wet (bottom) season; solid lines with a circle marker indicate leeward stations; dashed lines with a triangle marker indicate windward stations.

R_n increases with elevation along the windward transects for both seasons (Figure 14). Vertical profiles of R_n do not show consistent relationships with elevation along the leeward transect. The effects of clouds and clear atmosphere changes with elevation do not explain all of the variability. Differences in R_n can be explained by additional factors including albedo, and surface temperature. Vegetation should have an effect on decreasing surface temperature (less longwave outgoing radiation) and lowering surface albedo (less shortwave outgoing radiation) thus explaining higher R_n along the windward transect which is more vegetated and potentially explaining the increased R_n at HN-141 (1240 m) which is located within a leeward dry-land forest preserve (Section 8.1).

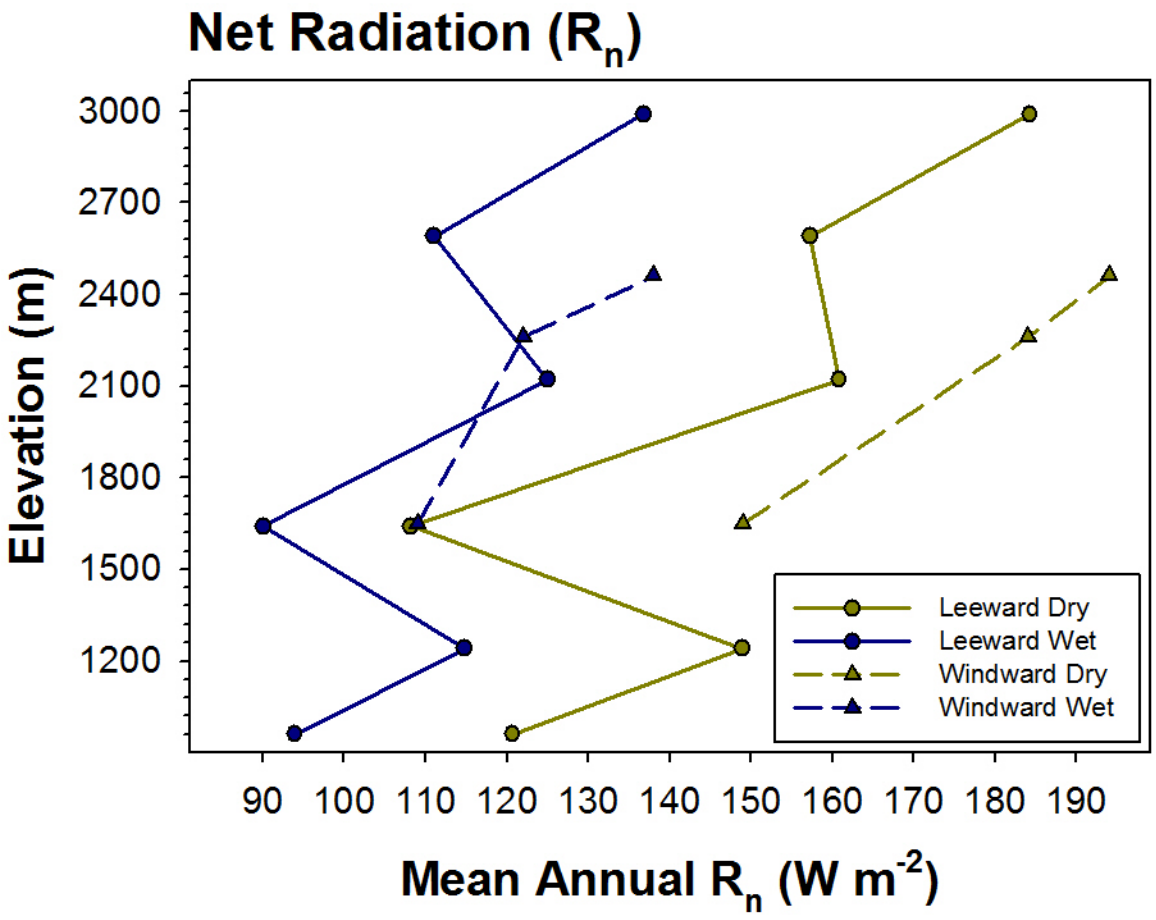

Figure 14: Vertical profiles of mean annual net radiation along leeward (solid line, circle marker) and windward (dashed line, triangle marker) elevation transects, or dry (yellow) and wet (blue) seasons.

4.4 Temperature

Much of the solar radiation transmitted through the atmosphere is absorbed at the Earth's surface, increasing its temperature. The surface, in turn, warms the lower atmosphere through conduction and longwave radiation emission (by the surface) and absorption (by the air). Surface air temperature (T_a) on a mountain slope is determined by R_n, but also by the temperature of the free atmosphere at a given elevation.

Hawai‘i has the consistently small annual T_a cycle characteristic of marine tropical climates (Figure 15). The differences between the coldest and warmest months (Table 7) is small (2.6 to 3.7 °C) with the highest mean monthly T_a values occurring primarily in August (September for 1650 m station) and lowest values occurring in February for all of the leeward stations and the mid-elevation windward station and in March and April for the 2260 m and 2460 m high-elevation windward stations, respectively. The differences in the timing of the lowest monthly T_a values on the windward transect are most likely explained by variations in cloud cover.

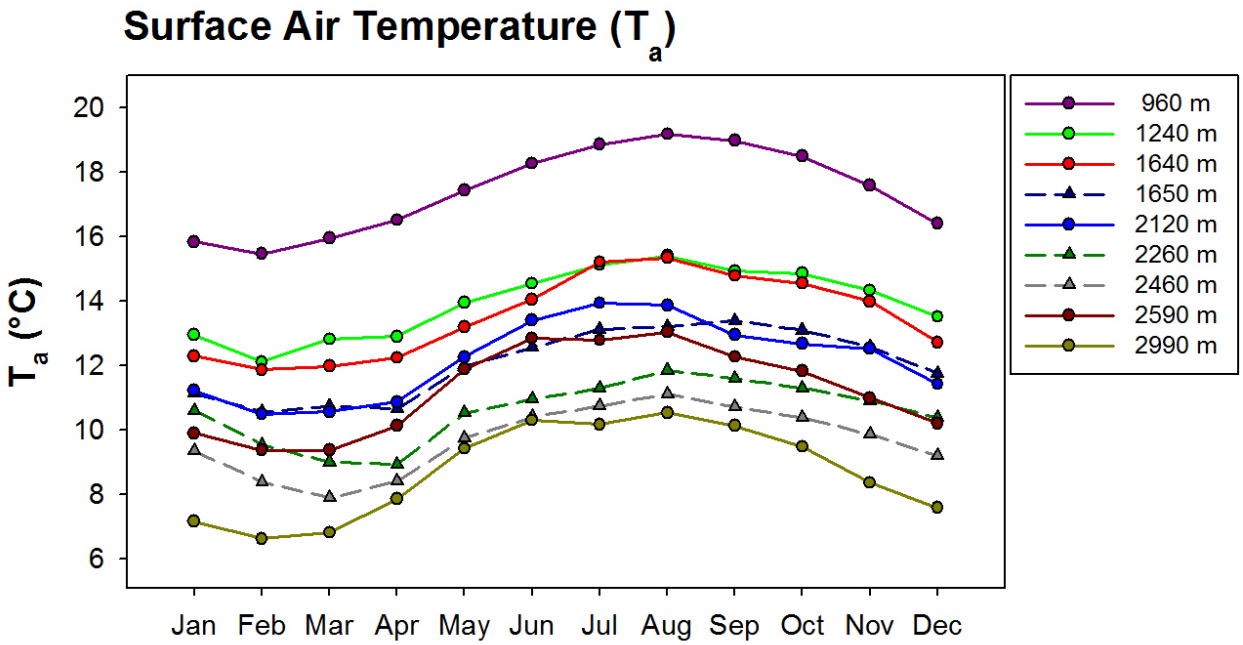

Figure 15: Mean annual cycle of surface air temperature (T_a); solid lines with a circle marker indicate leeward stations; dashed lines with a triangle marker indicate windward stations

Table 7: Mean annual cycle of surface air temperature (°C).

Sta ID	Elev	Jan	Feb	Mar	Apr	May	Jun	Jul	Aug	Sep	Oct	Nov	Dec	Annual	Dry	Wet
HN-119	960	15.8	15.5	16.0	16.5	17.4	18.3	18.9	19.2	19.0	18.5	17.6	16.4	17.4	18.5	16.3
HN-141	1240	12.9	12.1	12.8	12.9	14.0	14.5	15.1	15.4	14.9	14.9	14.3	13.5	14.0	14.8	13.1
HN-106	1640	12.3	11.9	12.0	12.2	13.2	14.1	15.2	15.4	14.8	14.6	14.0	12.7	13.5	14.5	12.5
HN-164	1650	11.1	10.6	10.7	10.7	12.0	12.6	13.1	13.2	13.4	13.1	12.6	11.8	12.1	12.9	11.2
HN-151	2120	11.2	10.5	10.6	10.9	12.3	13.4	13.9	13.9	13.0	12.7	12.5	11.4	12.2	13.2	11.2
HN-162	2260	10.6	9.5	9.0	8.9	10.5	11.0	11.3	11.9	11.6	11.3	10.9	10.4	10.6	11.3	9.9
HN-161	2460	9.3	8.4	7.9	8.4	9.8	10.4	10.7	11.1	10.7	10.4	9.9	9.2	9.7	10.5	8.8
HN-152	2590	9.9	9.4	9.4	10.1	11.9	12.8	12.8	13.0	12.3	11.8	11.0	10.2	11.2	12.4	10.0
HN-153	2990	7.2	6.6	6.8	7.8	9.4	10.3	10.2	10.5	10.1	9.5	8.4	7.6	8.7	10.0	7.4

The diurnal temperature cycles at all stations are marked by an abrupt change at sunrise and sunset and (Figure 16). During the dry season, when cloudy conditions are most common in the afternoon hours, temperature is relatively stable across the leeward transect between 1240 and 2120 m due to the well-mixed air within the cloud zone. The stations located below (above) this zone exhibit a more pronounced diurnal cycle and are much cooler (warmer) due to the presence (absence) of clouds. For the wet season, clearer conditions promote a more distinct elevation-dependent relationship although the effects of clouds are still apparent. Again, the

onset of afternoon clouds is most noticeable at the stations located within the heart of the cloud zone on both transects, marked by a distinct temperature decrease between 11:00 and 12:00 h.

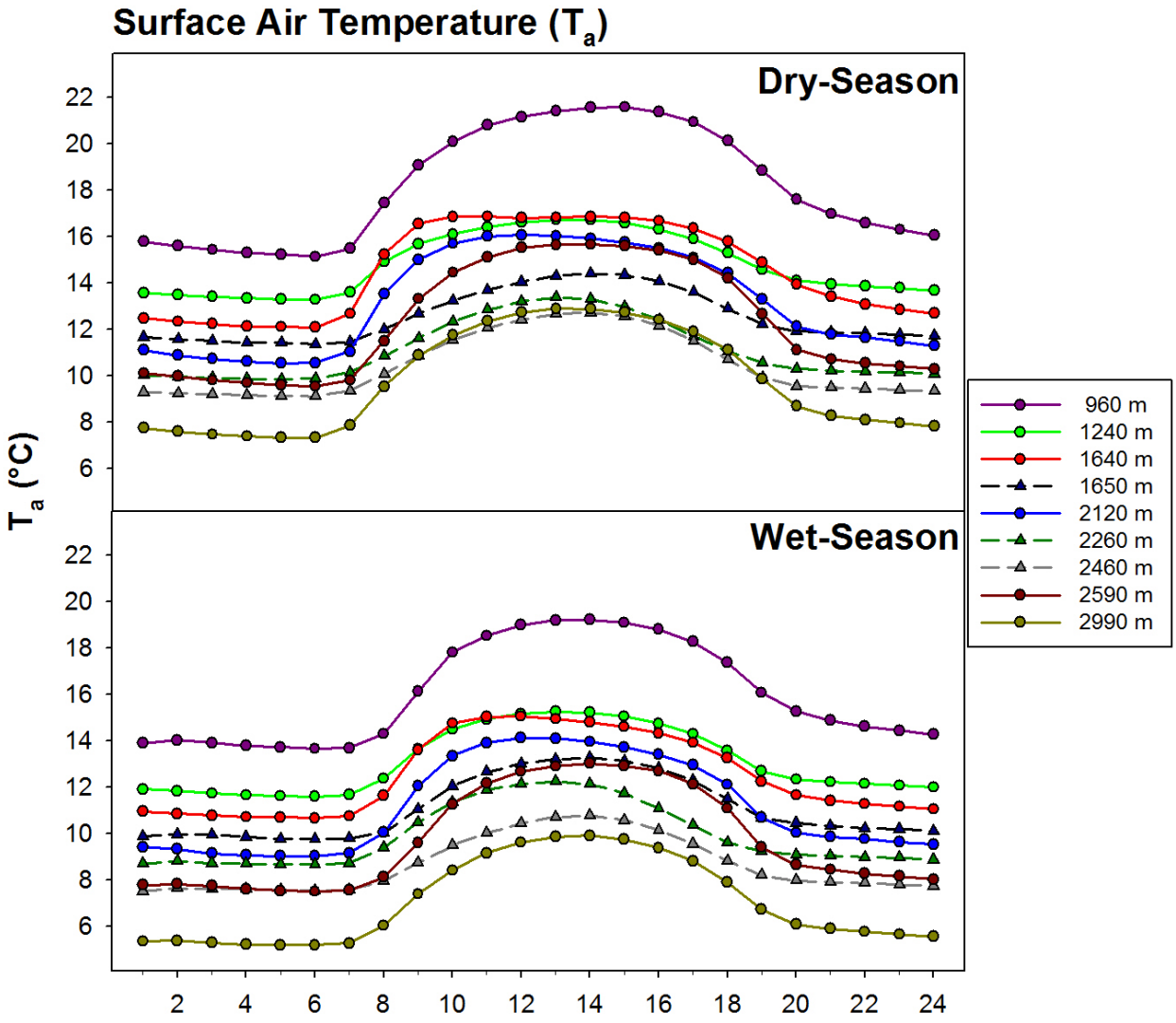

Figure 16**:** Diurnal cycles of surface air temperature for the dry (top) and wet (bottom) season; solid lines with a circle marker indicate leeward stations; dashed lines with a triangle marker indicate windward stations.

A clear pattern of decreasing temperatures with increasing elevation is seen, although the rate at which temperatures decrease is not constant along each transect (Figure 17). Increases in temperature with elevation that occur within the TWI layer are not directly identifiable at this vertical resolution and are smoothed out by vertical fluctuations in the TWI level. However,

temperature lapse rates (the rate of temperature decrease with elevation) indicate a clear relationship between elevation and the stations affected by the inversion and the moist conditions that exist within the cloud zone below it. Temperature lapse rates occurring on the leeward transect below HN-141 (1240 m) and above HN-152 (2590 m) are greater than temperature lapse rates occurring between these points. These lower lapse rates can be explained, in part, by the release of latent energy within the cloud zone, so that rising air cools at the wet adiabatic lapse rate (approximately half of the dry adiabatic lapse rate) within the cloud. In addition, the effects of increased temperature due to the presence of the inversion may have a dampening effect on lapse rates. Since the air is generally unsaturated below the LCL and above the TWI, lapse rates are greater there. The presence of the TWI and the subsequent increase in Ta associated with it have a dampening effect on the lapse rates as well.

The data indicate noticeably lower temperatures at windward stations compared with leeward stations at similar elevations. For example, stations located at 1640 m and 1650 m on leeward and windward exposures, respectively, have an annual T_a difference of 1.4˚C despite only a 10 m difference in elevation. Under normal moist adiabatic conditions the temperature lapse rate would be 0.64˚C per 100 m (2. 6˚C) between these two sites which is 1.2˚C greater than observed. Warmer leeward T_a is driven primarily by a difference in partitioning of net radiation. On the Windward side of the island, where moisture is not limited, a high portion of net radiation is partitioned to latent energy which has a cooling effect on the atmosphere. On the leeward side of the island, where moisture is limited, a large portion of net radiation is partitioned to sensible heat energy, which has a warming effect on the atmosphere.

It is also interesting to note that the two leeward stations located within the cloud zone HN-141 (1240 m) and HN-106 (1640 m) which have only a 0.5˚ difference in mean annual T_a despite a vertical elevation difference of 400 m. This is most likely explained by the surface characteristics affecting the partitioning of available energy at the two sites. Active forest restoration at Auwahi (HN-141) appears to have lowered the air temperature there (see section 8.1).

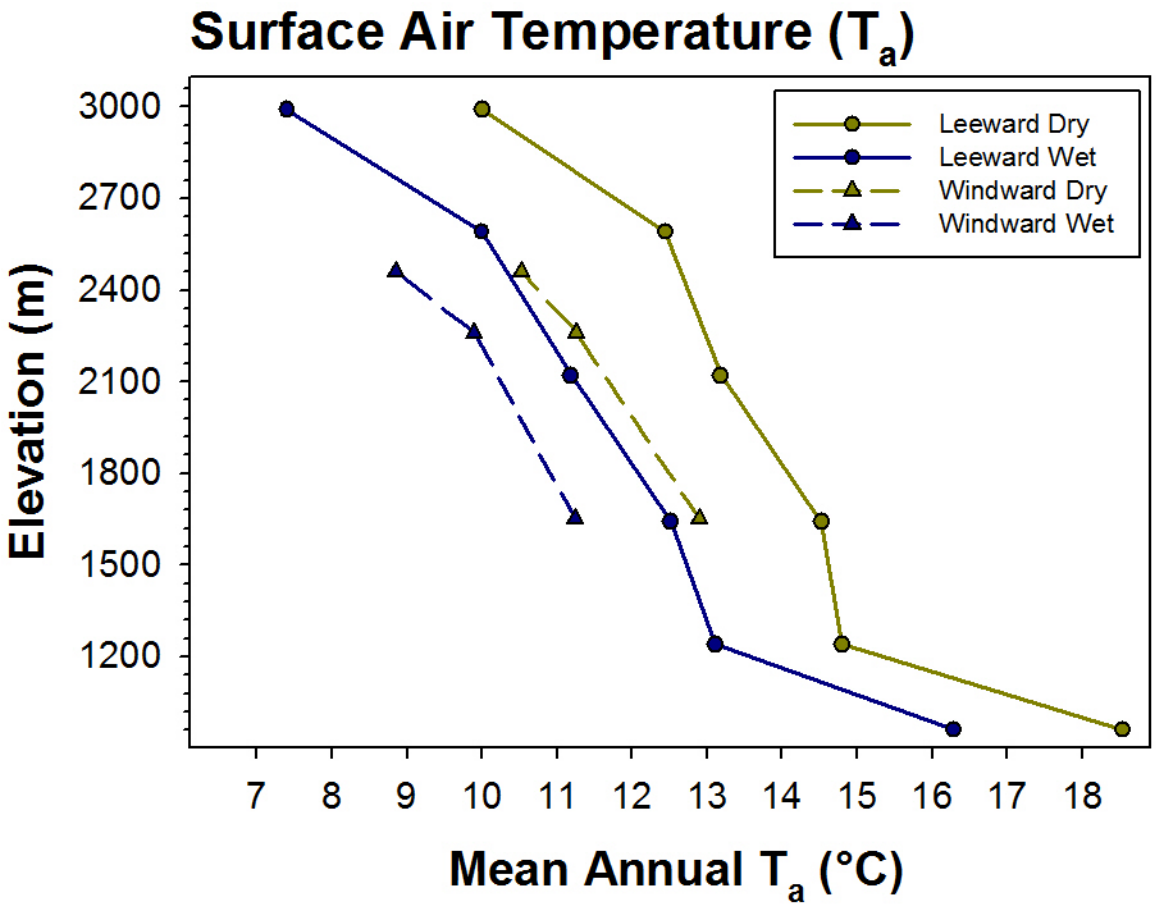

Figure 17: Vertical profiles of mean annual surface air temperature along leeward (solid line, circle marker) and windward (dashed line, triangle marker) elevation transects, or dry (yellow) and wet (blue) seasons.

4.5 Relative Humidity

Relative humidity (RH) is the ratio of water vapor in the air to the maximum amount of water vapor the air can hold. RH is a determining factor in the evaporation rate and once RH reaches 100%, air is considered saturated and cannot absorb any additional water vapor. RH is determined by both the amount of water vapor in the air and the air temperature (which determines the water vapor content at saturation). Because air can hold more water vapor at higher temperatures, an inverse relationship exists between RH and air temperature. On the mountain slopes of Haleakalā the relationship between relative humidity and temperature is much more complex, especially when considering the dominant effects of the TWI on moisture regimens at high elevations. The mean annual cycles of relative humidity at HaleNet stations are not very distinct (Figure 18). All of the stations experience their lowest mean monthly values in either January or December; however, the timing of the highest monthly values varies with elevation (Table 8). For the mid-elevation stations highest relative humidity is found between April and June, corresponding to a time of frequent TWI conditions. For high-elevation stations maxima occur between the months of September and November. These months correspond to times of decreased TWI frequency and for September the highest TWI base height. Stations located well below the inversion show fairly flat annual cycles. In general, difference between the highest and lowest mean monthly values increases with elevation and the greatest differences are found on the windward transect at high elevations. The smallest differences in monthly relative humidity occur within the cloud and marine zones located beneath the TWI.

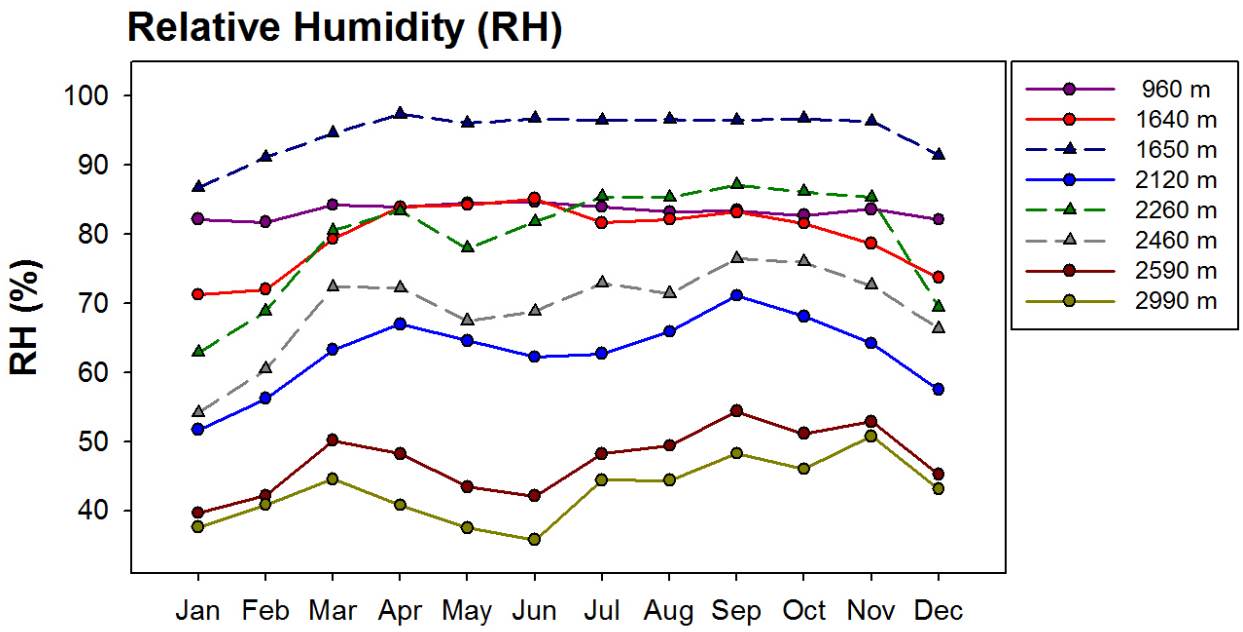

Figure 18: Mean annual relative humidity (RH); solid lines with a circle marker indicate leeward stations; dashed lines with a triangle marker indicate windward stations

Table 8: Mean annual cycle of relative humidity (%).

Sta ID	Elev	Jan	Feb	Mar	Apr	May	Jun	Jul	Aug	Sep	Oct	Nov	Dec	Annual	Dry	Wet
HN-119	960	82.2	81.8	84.3	83.9	84.5	84.7	84.0	83.3	83.4	82.7	83.6	82.1	83.4	83.8	83.0
HN-106	1640	71.3	72.1	79.3	83.9	84.2	85.1	81.7	82.2	83.2	81.6	78.7	73.7	79.7	83.0	76.5
HN-164	1650	86.8	91.1	94.6	97.4	96.1	96.7	96.5	96.6	96.5	96.7	96.3	91.4	94.7	96.5	92.9
HN-151	2120	51.7	56.2	63.3	67.0	64.6	62.3	62.7	65.9	71.1	68.1	64.2	57.5	62.9	65.8	60.0
HN-162	2260	62.9	68.9	80.5	83.4	77.9	81.8	85.5	85.3	87.1	86.2	85.3	69.5	79.5	84.0	75.1
HN-161	2460	54.2	60.5	72.4	72.3	67.5	68.8	72.9	71.4	76.5	76.0	72.6	66.4	69.3	72.2	66.4
HN-152	2590	39.7	42.2	50.2	48.2	43.5	42.1	48.3	49.4	54.4	51.2	52.9	45.2	47.3	48.1	46.4
HN-153	2990	37.6	40.8	44.6	40.8	37.5	35.8	44.4	44.4	48.3	46.0	50.8	43.1	42.8	42.7	42.9

Diurnal cycles of RH for the dry and wet seasons have distinct patterns for windward and leeward sites (Figure 19). On the leeward exposure, beginning in the cloud zone, relative humidity increases in the mid-morning and decreases in the late afternoon. Increases in RH are explained by the transport of moisture by upslope winds during the daylight hours. At station HN-119 (960 m) located just below the cloud zone relative humidity decreases in the afternoon hours due to the increase in temperature. In the evening hours relative humidity increases as temperature decreases. For windward station HN-164 (1650 m) located in the heart of the cloud zone , relative humidity remains relatively constant throughout the day suggesting that the effects of the air temperature cycle (which is very muted to start with) are offset by a cycle in water

vapor content (higher during the day to offset the higher saturation vapor pressure) because of consistently moist conditions driven by orographic cloud development.

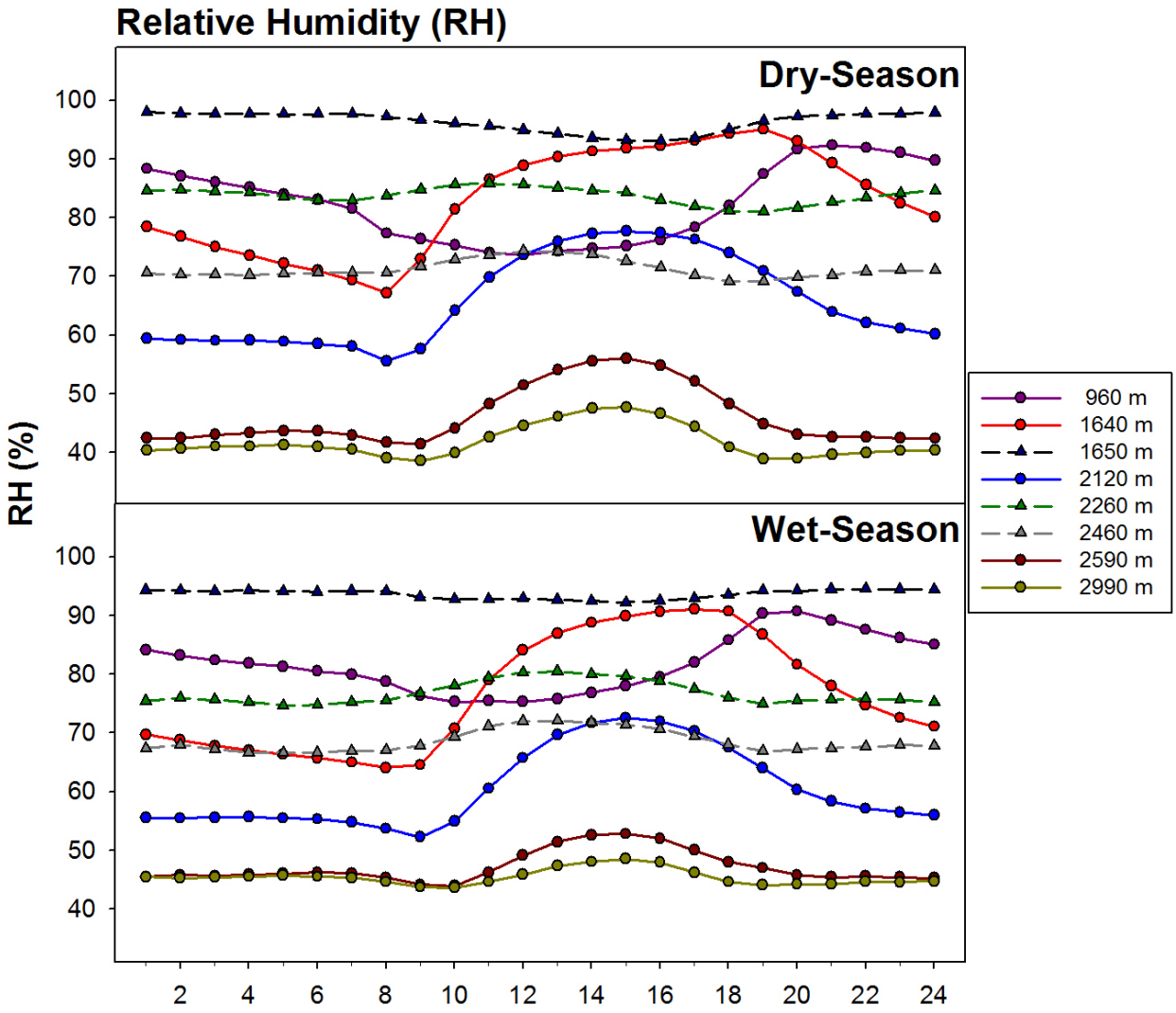

Figure 19**:** Diurnal cycles of relative humidity for the dry (top) and wet (bottom) season; solid lines with a circle marker indicate leeward stations; dashed lines with a triangle marker indicate windward stations.

In general, mean annual relative humidity decreases with elevation along both transects annually (Figure 20). The highest relative humidity values are found at the windward cloud zone station and, in general, windward stations have higher relative humidity than leeward stations at similar elevations. The lowest relative humidity values are found at the highest leeward stations

located well above the mean TWI base, where air is arid due to the isolating effects of the TWI which impedes the movement of moist marine air to high elevations.

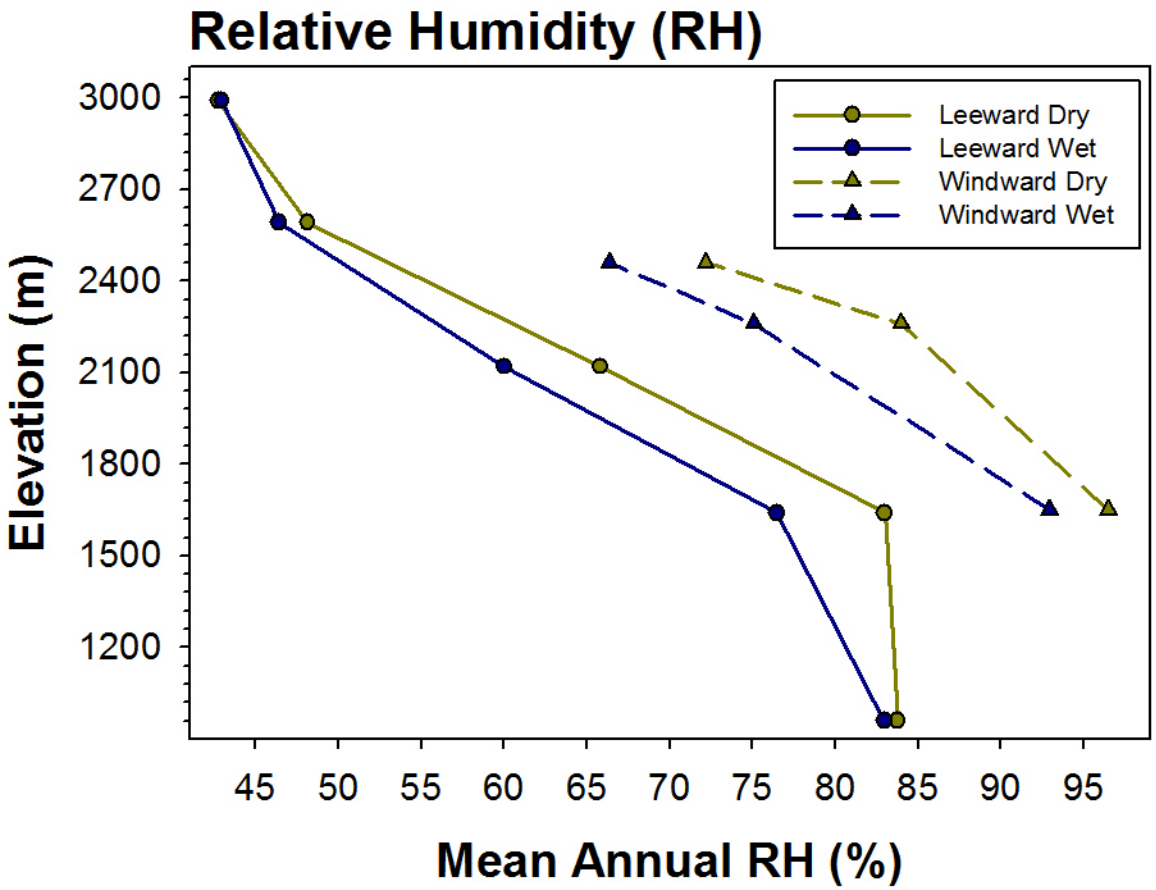

Figure 20: Vertical profiles of mean annual relative humidity along leeward (solid line, circle marker) and windward (dashed line, triangle marker) elevation transects, or dry (yellow) and wet (blue) seasons.

4.6 Vapor Pressure Deficit

The capacity of the air to hold water vapor is controlled by the air temperature. While relative humidity is a measure of the moistness of the air, expressed as a ratio of the water vapor content (e.g., the vapor pressure) to the saturation water vapor (e.g., the saturation vapor pressure), vapor pressure deficit (VPD) is a measure of the dryness of the air given as the saturation water vapor minus the vapor pressure.

The mean annual cycle of VPD has different patterns depending on location (Figure 21). A pronounced annual cycle with summer maxima are observed at the highest elevation leeward sites and a less pronounced annual cycle with winter maximum are observed along the windward transect and within the leeward cloud zone. For the highest-elevation stations maxima occurring in June and minima occurring in March (Table 9) correspond to the highest and lowest frequency of the TWI respectively (Figure 2). Despite the low temperatures found at high elevations, the predominantly dry-conditions found above the TWI are driving some of the highest VPD across the network.

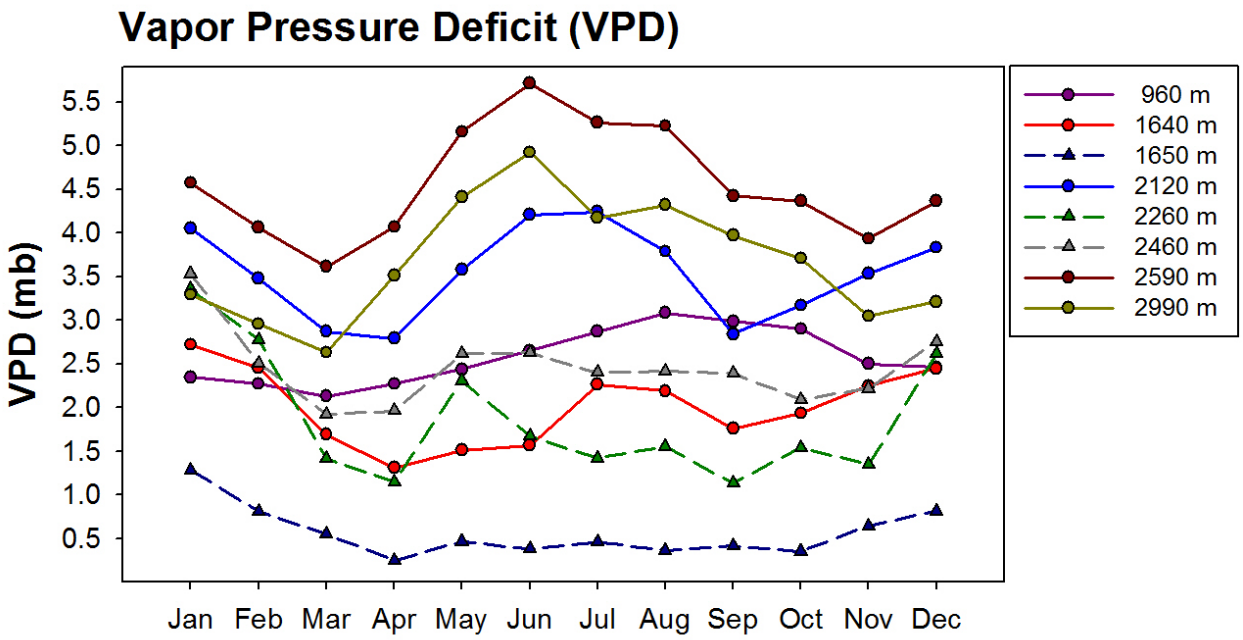

Figure 21: Mean annual cycle of vapor pressure deficit (VPD); solid lines with a circle marker indicate leeward stations; dashed lines with a triangle marker indicate windward stations.

Table 9: Mean annual cycle of vapor pressure deficit (mb).

Sta ID	Elev	Jan	Feb	Mar	Apr	May	Jun	Jul	Aug	Sep	Oct	Nov	Dec	Annual	Dry	Wet
HN-119	960	2.3	2.3	2.1	2.3	2.4	2.7	2.9	3.1	3.0	2.9	2.5	2.5	2.6	2.8	2.3
HN-106	1640	2.7	2.5	1.7	1.3	1.5	1.6	2.3	2.2	1.8	1.9	2.2	2.5	2.0	1.9	2.1
HN-164	1650	1.3	0.8	0.6	0.2	0.5	0.4	0.5	0.4	0.4	0.4	0.6	0.8	0.6	0.4	0.7
HN-151	2120	4.1	3.5	2.9	2.8	3.6	4.2	4.2	3.8	2.8	3.2	3.5	3.8	3.5	3.6	3.4
HN-162	2260	3.4	2.8	1.4	1.1	2.3	1.7	1.4	1.6	1.1	1.5	1.3	2.6	1.9	1.6	2.1
HN-161	2460	3.5	2.5	1.9	2.0	2.6	2.6	2.4	2.4	2.4	2.1	2.2	2.8	2.5	2.4	2.5
HN-152	2590	4.6	4.1	3.6	4.1	5.2	5.7	5.3	5.2	4.4	4.4	3.9	4.4	4.6	5.0	4.1
HN-153	2990	3.3	3.0	2.6	3.5	4.4	4.9	4.2	4.3	4.0	3.7	3.0	3.2	3.7	4.3	3.1

The diurnal cycle of vapor pressure deficit at each station (Figure 22) varies across elevation, exposure and time. For leeward stations located above and below the cloud zone, VPD follows a pattern similar to diurnal temperature profiles (Figure 23), where VPD increases as the air begins to warm. For leeward stations located within the cloud zone (1650 to 2120 m), a marked afternoon decrease in VPD becomes apparent as the air becomes saturated. For windward stations, VPD is fairly constant throughout the day.

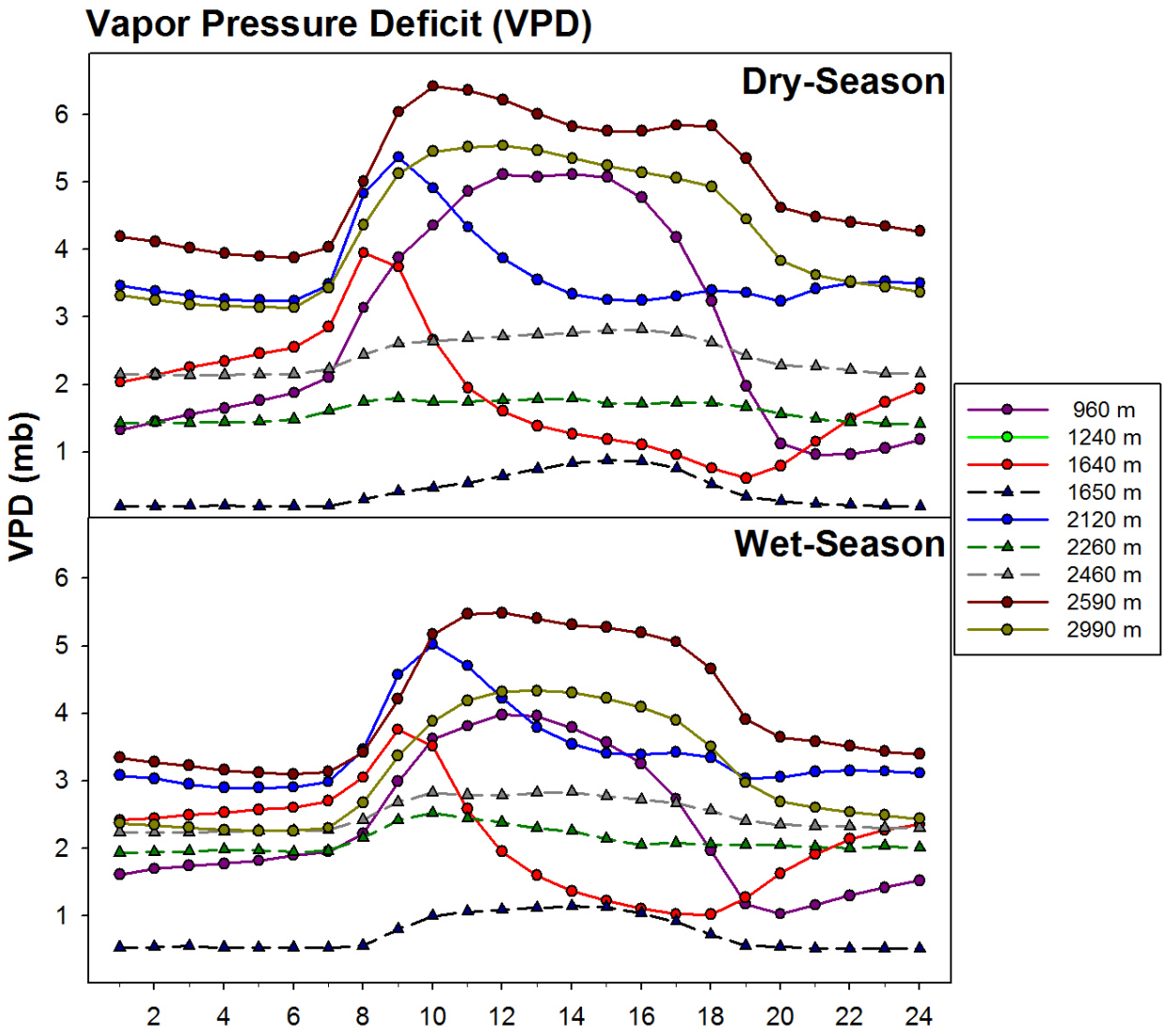

Figure 22**:** Diurnal cycles of vapor pressure deficit for the dry (top) and wet (bottom) season; solid lines with a circle marker indicate leeward stations; dashed lines with a triangle marker indicate windward stations.

Decreases in VPD are found on the leeward transect between 960 and 1650 m due to increases in humidity within the cloud zone. As relative humidity decreases from 1650 to 2590 an increase in VPD is observed. At the highest elevations cold temperatures drive decreases in VPD from 2590 to 2990 m. Leeward transects show a general increase in VPD with height.

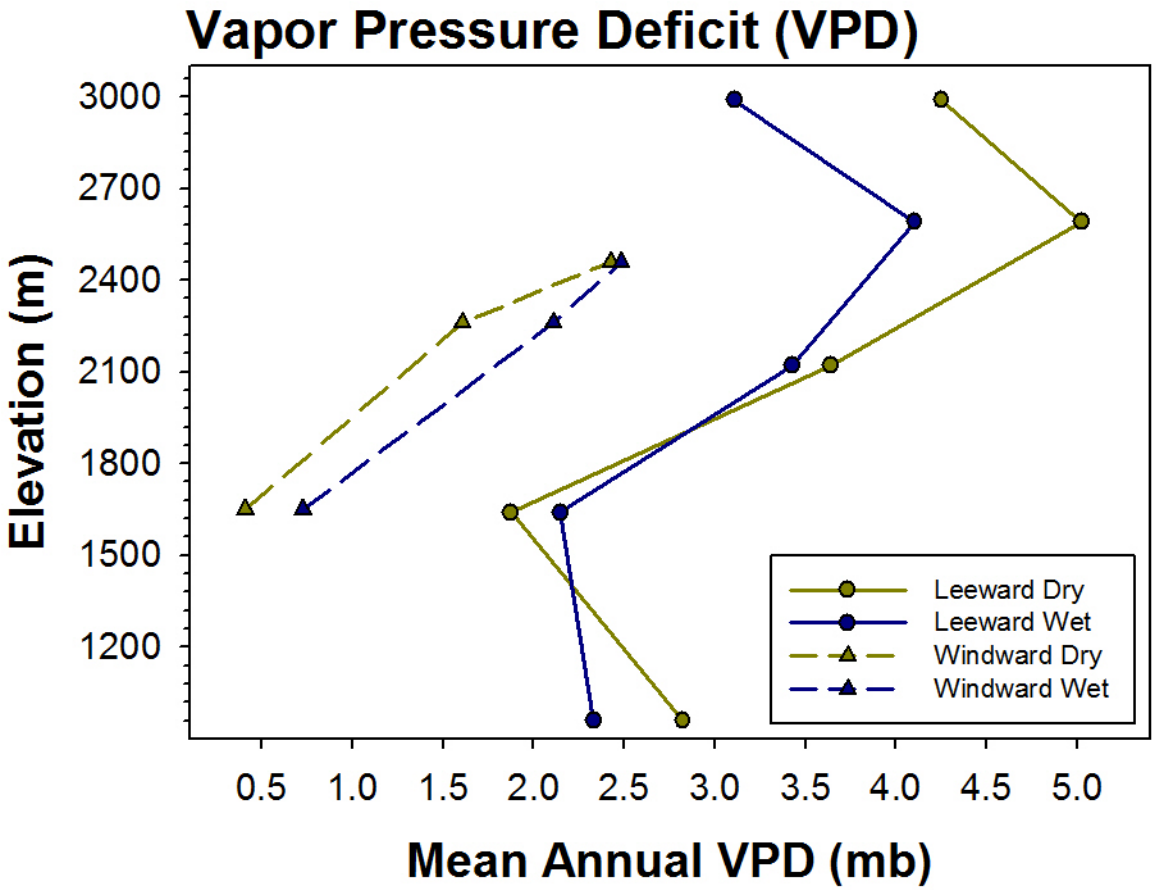

Figure 23: Vertical profiles of mean annual vapor pressure deficit along leeward (solid line, circle marker) and windward (dashed line, triangle marker) elevation transects, or dry (yellow) and wet (blue) seasons.

4.7 Wind Speed

The highest mountains of the Hawaiian Islands are also some of the windiest places in the archipelago. At more than 3000 m elevation, the summit area of Haleakalā is exposed to the stronger winds found in the free atmosphere at that level. At lower elevations, winds are reduced by friction with the surface. The wind characteristics at any particular site are highly variable due to the surface topography (i.e. vegetation and relief), orientation to the prevailing trade winds and the exposure of the instrumentation. For the HN stations analyzed in this study no clear annual wind speed (WS) cycle was observed (Figure 24). However, the three windward stations and the leeward summit station had their highest mean monthly values in either June or July (Table 10), which corresponds to the period of highest trade wind frequency (Figure 2). Three of the five remaining leeward stations had their highest monthly wind speeds in January (960 m, 1640 m and 2590 m), August (1240 m), and December (2120 m).

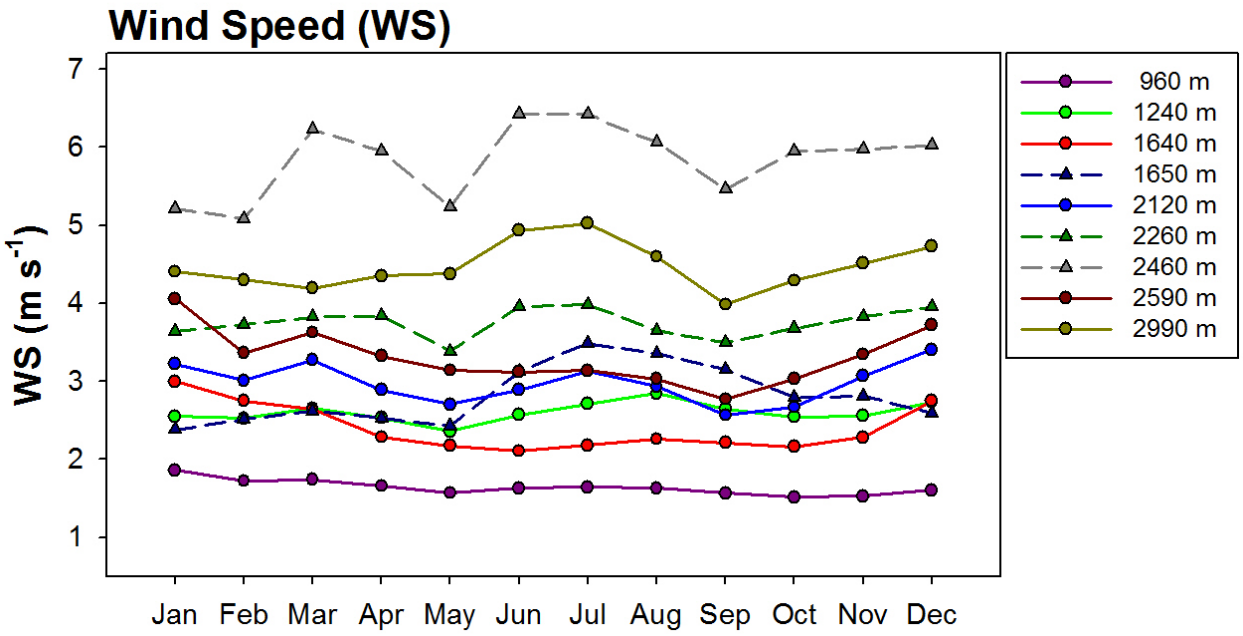

Figure 24: Mean annual cycle of wind speed (WS); solid lines with a circle marker indicate leeward stations; dashed lines with a triangle marker indicate windward stations

Table 10: Mean annual cycle of Wind Speed (m s^{-1}).

Sta ID	Elev	Jan	Feb	Mar	Apr	May	Jun	Jul	Aug	Sep	Oct	Nov	Dec	Annual	Dry	Wet
HN-119	960	1.9	1.7	1.7	1.7	1.6	1.6	1.6	1.6	1.6	1.5	1.5	1.6	1.6	1.6	1.7
HN-141	1240	2.5	2.5	2.7	2.5	2.4	2.6	2.7	2.8	2.6	2.5	2.6	2.7	2.6	2.6	2.6
HN-106	1640	3.0	2.7	2.6	2.3	2.2	2.1	2.2	2.3	2.2	2.2	2.3	2.7	2.4	2.2	2.6
HN-164	1650	2.4	2.5	2.6	2.5	2.4	3.1	3.5	3.4	3.2	2.8	2.8	2.6	2.8	3.1	2.6
HN-151	2120	3.2	3.0	3.3	2.9	2.7	2.9	3.1	2.9	2.6	2.7	3.1	3.4	3.0	2.8	3.1
HN-162	2260	3.6	3.7	3.8	3.8	3.4	4.0	4.0	3.6	3.5	3.7	3.8	4.0	3.7	3.7	3.8
HN-161	2460	5.2	5.1	6.2	5.9	5.2	6.4	6.4	6.1	5.5	5.9	6.0	6.0	5.8	5.9	5.7
HN-152	2590	4.1	3.4	3.6	3.3	3.1	3.1	3.1	3.0	2.8	3.0	3.3	3.7	3.3	3.0	3.6
HN-153	2990	4.4	4.3	4.2	4.4	4.4	4.9	5.0	4.6	4.0	4.3	4.5	4.7	4.5	4.5	4.4

Diurnal cycles of wind speed are most pronounced at leeward mid-elevation stations where winds diminish around the times of reversals in the direction of thermal slope winds in the mid-morning and early evening (Figure 25). During the day, slopes and overlying air are warmed, and the warm air moves convectively upslope. At night when the air cools and becomes dense, it moves downslope under the influence of gravity. The marked depressions in the diurnal cycle are indications of when these up and down slope shifts occur. At windward stations, a

distinct decrease in wind speed is seen in the afternoon hours at all of the stations, but most notably at the highest elevations. The drivers behind this decrease are not completely understood.

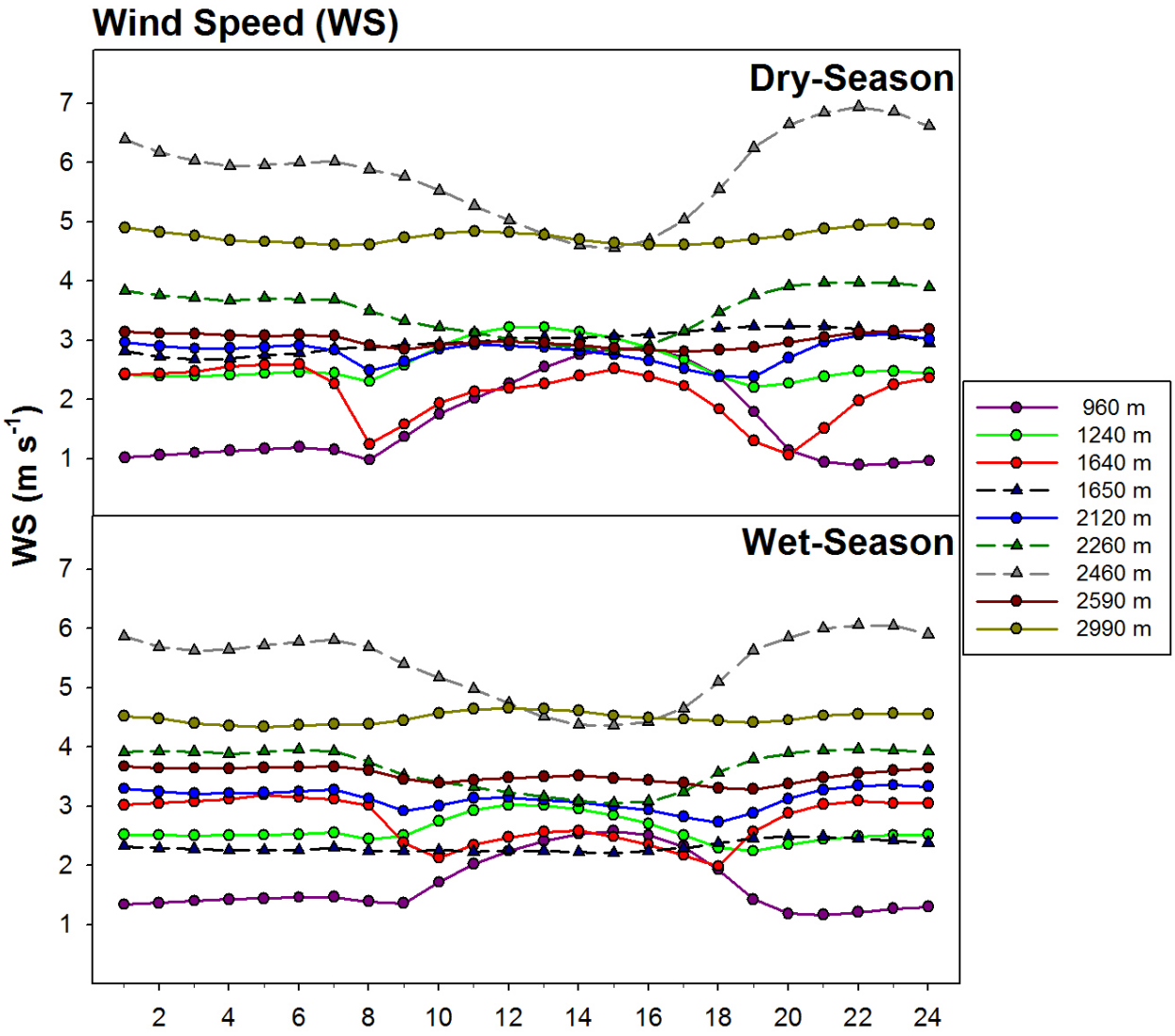

Figure 25: Diurnal cycles of wind speed for the dry (top) and wet (bottom) season; solid lines with a circle marker indicate leeward stations; dashed lines with a triangle marker indicate windward stations.

In general, mean annual wind speed increases with elevation in both the dry and wet seasons and along both windward and leeward gradients (Figure 26). The exception to this is the 1240 m station on the leeward transect, which has higher wind speeds than the station above it (1640 m) during the dry season (Table 10). This may be explained by the greater instrument exposure at the 1240 m station and the effect of winds that wrap around the north and south

exposures of the mountain and converge at this location. In general, leeward wind speed is greater in the summer and the winter. Wind speed on the windward side of the island is rather consistent throughout the year and the greatest wind speeds are found on the windward summit station located at 2460 m.

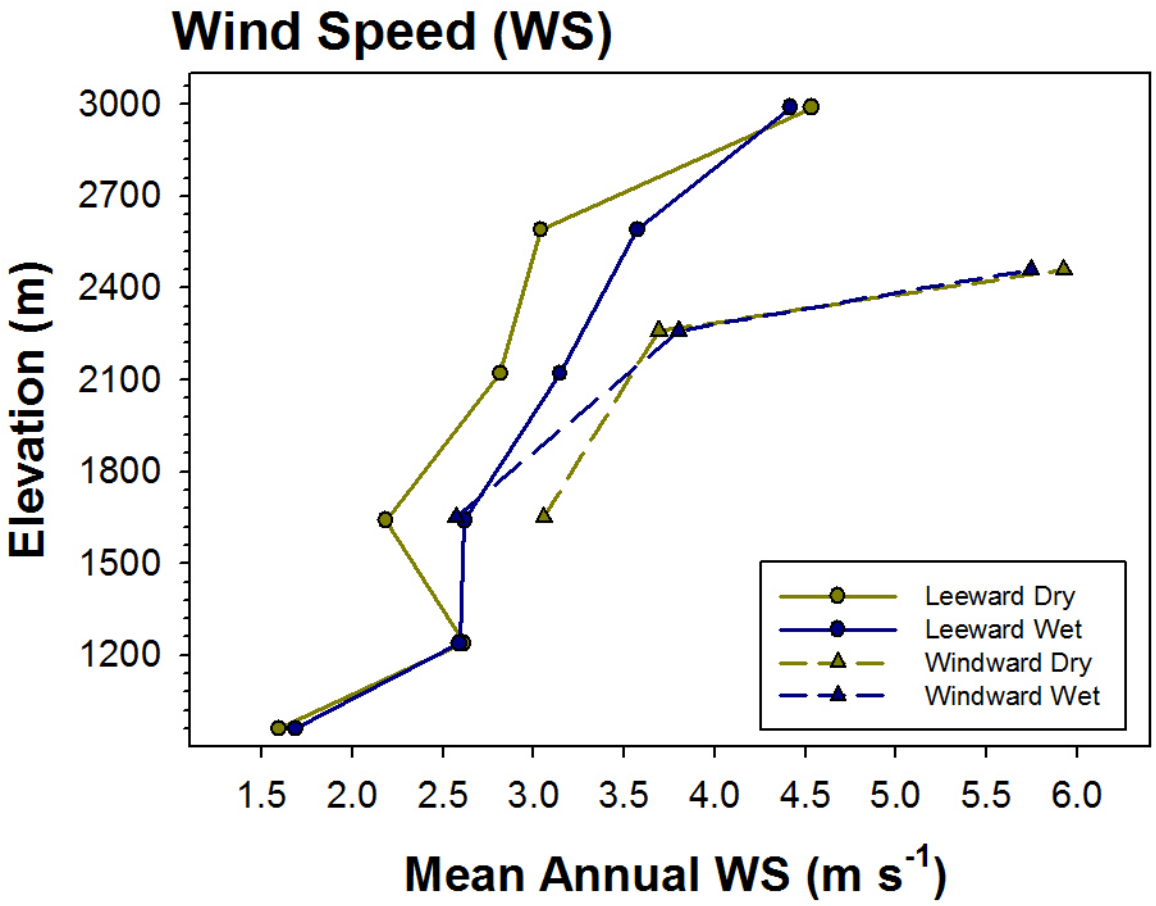

Figure 26: Vertical profiles of mean annual wind speed along leeward (solid line, circle marker)and windward (dashed line, triangle marker) elevation transects, or dry (yellow) and wet (blue) seasons.

4.8 Precipitation

In Hawai‘i, the interaction of mountainous topography, the persistence of the trade winds, the heating and cooling of the land and the consistent presence of the TWI create some of the most spatially diverse rainfall patterns found anywhere in the world (Giambelluca et al., 2013). Understanding mean rainfall patterns is important for a variety of resource management issues in Hawai‘i, including the assessment and protection of freshwater resources and the successful management of native ecosystems. Rainfall can be highly variable from year to year; however, the long-term mean annual cycle is in agreement with the traditional understanding of the Hawaiian wet and dry seasons (Figure 27). As expected, the highest mean monthly precipitation occurs in the wet season and the lowest monthly values occur in the dry season (Table 11). For the highest elevation stations, monthly precipitation peaks in March and in December and minima are found in May and June which correspond with the months of lowest and highest TWI frequency of occurrence, respectively (Figure 2). Windward stations are consistently wetter than leeward stations throughout the year.

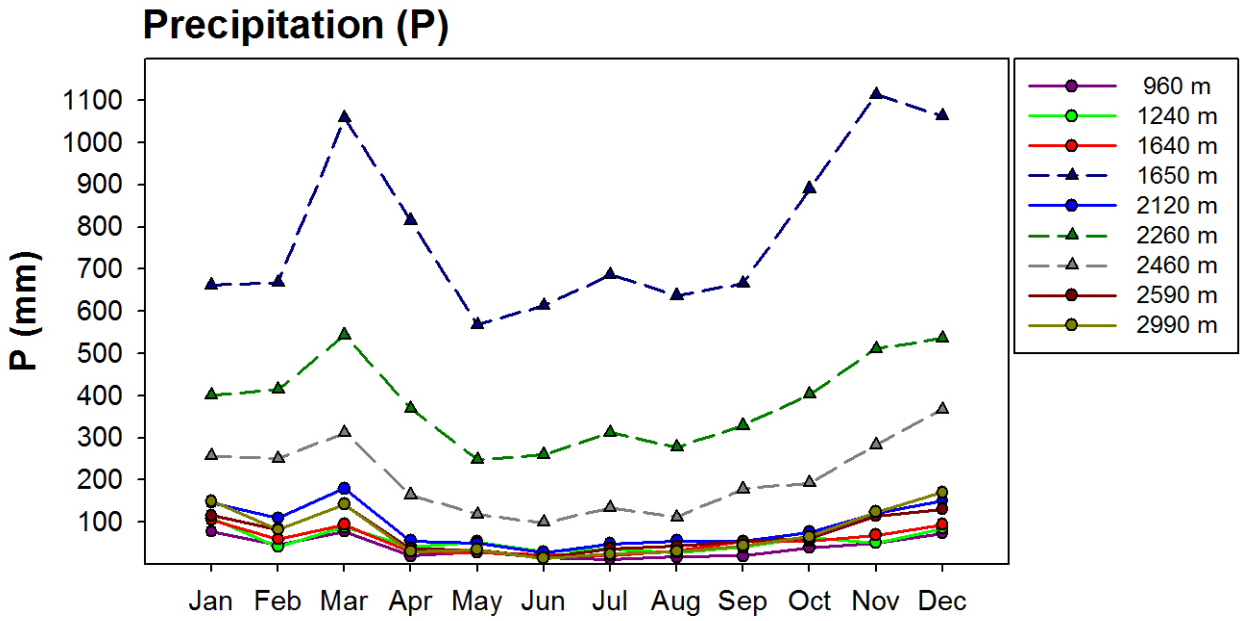

Figure 27: Mean annual cycle of precipitation (P); solid lines with a circle marker indicate leeward stations; dashed lines with a triangle marker indicate windward stations.

Table 11: Mean annual cycle of precipitation (mm).

Sta ID	Elev	Jan	Feb	Mar	Apr	May	Jun	Jul	Aug	Sep	Oct	Nov	Dec	Annual	Dry	Wet
HN-119	960	78	45	78	20	30	17	12	17	20	39	51	74	482	136	346
HN-141	1240	109	42	88	42	54	30	36	27	40	63	51	85	667	250	417
HN-106	1640	105	59	94	30	29	22	21	32	55	56	69	95	667	214	452
HN-164	1650	662	668	1059	816	569	613	686	637	666	891	1114	1063	9445	4063	5382
HN-151	2120	146	110	180	56	50	28	49	56	55	76	122	151	1078	313	765
HN-162	2260	401	414	544	369	248	261	313	278	329	403	511	536	4606	1831	2776
HN-161	2460	257	251	312	165	118	99	133	112	178	193	284	368	2469	834	1635
HN-152	2590	116	83	142	38	35	16	37	43	54	61	114	131	869	245	624
HN-153	2990	151	82	143	30	35	15	24	31	44	66	124	171	915	214	701

Where monthly values (Jan-Dec) are the Period-of-record average monthly sums for a period encompassing the start date of each station and an end date of October 2013; Annual is the twelve month sum; Dry is the May to October Sum; Wet is the November to April sum.

Diurnal profiles are unique for both leeward and windward exposures. On the Leeward exposure, there is a distinct afternoon maximum at all of the stations in the dry season and an afternoon maximum at the three mid elevation stations in the wet season (Figure 28). On the windward exposure there are distinct minima in the afternoon hours. These observations are

consistent with the general rule that rainfall peaks during the night over oceans and during the afternoon over the land.

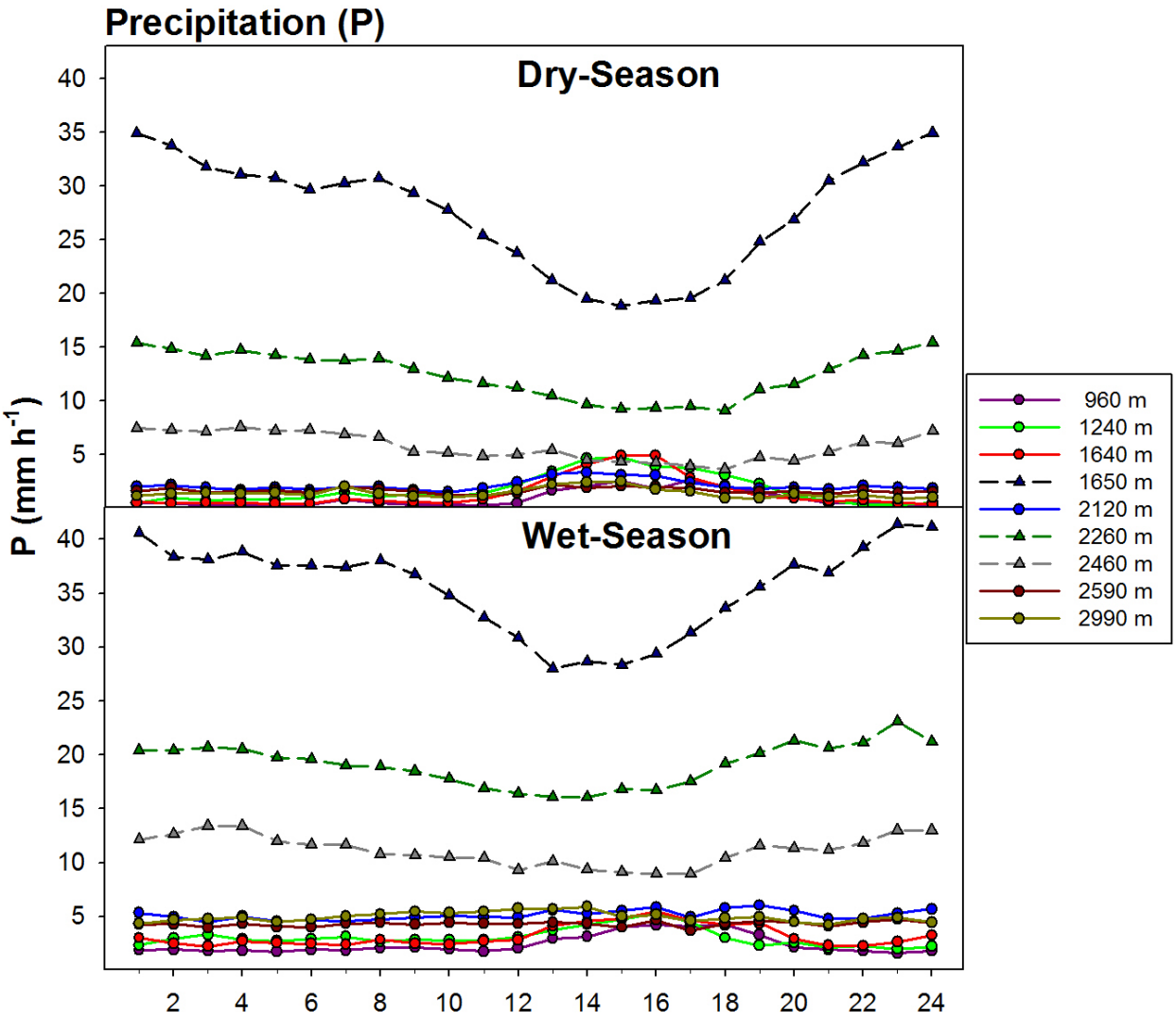

Figure 28**:** Diurnal cycles of precipitation for the dry (top) and wet (bottom) season; solid lines with a circle marker indicate leeward stations; dashed lines with a triangle marker indicate windward stations.

Precipitation gradients along the slopes of Haleakalā have many unique spatial characteristics (Figure 29). Along the leeward transect there is very little change in precipitation with elevation. This is most likely explained by the fact that the leeward transect does not follow a straight line up the mountain and also that most of the stations are located in close proximity to

the same isohyets (Figure 3). Along the windward transect precipitation is much greater than the leeward transect and there is a consistent decrease with elevation. Windward stations run perpendicular through several isohyets along the transect. During both the dry and wet seasons, precipitation is lowest at the 960 m station positioned directly below the cloud zone (Table 11). The highest rainfall totals are found at HN-164 (1650 m) in the heart of the windward cloud zone. Rainfall at this station is the highest of anywhere in the State (see section 8.3).

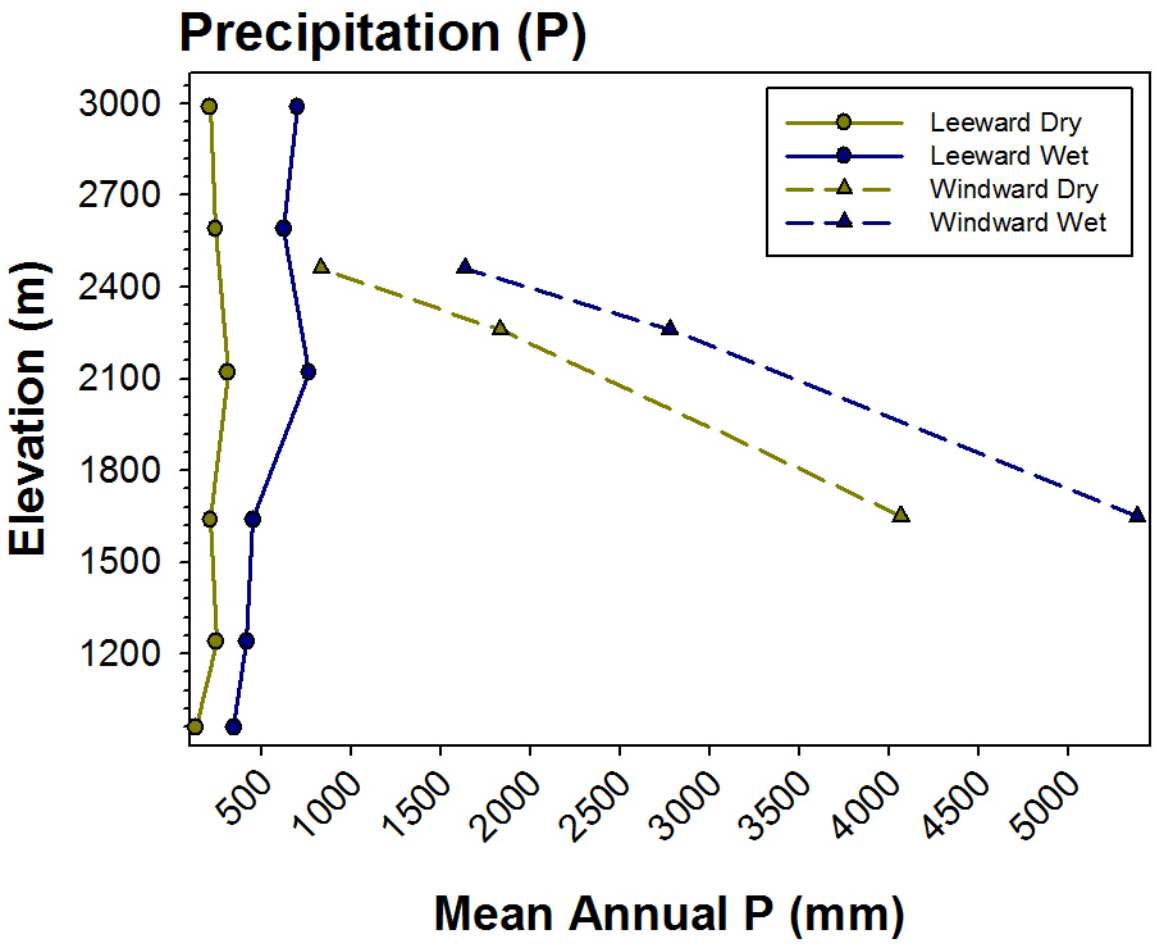

Figure 29: Vertical profiles of mean annual precipitation along leeward (solid line, circle marker) and windward (dashed line, triangle marker) elevation transects, or dry (yellow) and wet (blue) seasons.

4.9 Soil Moisture

Soil moisture (SM) is an important control on plant vitality. The moisture content of the soil depends on a number of factors including rainfall amount, soil properties, hill slope angle, plant transpiration and evaporation from the soil. Annual cycles of soil moisture are most pronounced at leeward mid-elevation stations located at or beneath the mean TWI observed throughout the dry season (Figure 30). For leeward stations located above the TWI, decreases in dry season soil moisture are identifiable but not as pronounced as the mid-elevation stations. For windward stations no apparent annual cycle was identified, with predominantly wet conditions observed throughout the year. For all stations, maximum values occur in the wet season and minima occur in the dry season (Table 12).

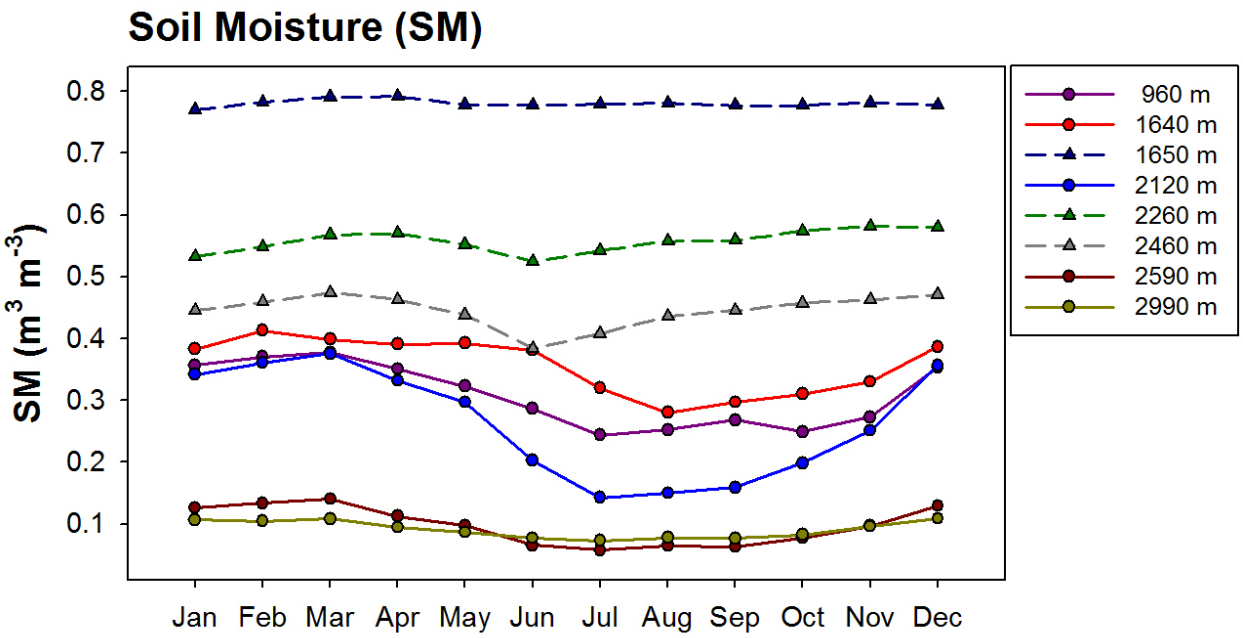

Figure 30: Mean annual cycle of soil moisture (SM); solid lines with a circle marker indicate leeward stations; dashed lines with a triangle marker indicate windward stations.

Table 12: Mean annual cycle of soil moisture (m^3 m^{-3}).

Sta ID	Elev	Jan	Feb	Mar	Apr	May	Jun	Jul	Aug	Sep	Oct	Nov	Dec	Annual	Dry	Wet
HN-119	960	0.36	0.37	0.38	0.35	0.32	0.29	0.24	0.25	0.27	0.25	0.27	0.35	0.31	0.27	0.35
HN-106	1640	0.38	0.41	0.40	0.39	0.39	0.38	0.32	0.28	0.30	0.31	0.33	0.39	0.36	0.33	0.38
HN-164	1650	0.77	0.78	0.79	0.79	0.78	0.78	0.78	0.78	0.78	0.78	0.78	0.78	0.78	0.78	0.78
HN-151	2120	0.34	0.36	0.38	0.33	0.30	0.20	0.14	0.15	0.16	0.20	0.25	0.36	0.26	0.19	0.34
HN-162	2260	0.53	0.55	0.57	0.57	0.55	0.52	0.54	0.56	0.56	0.57	0.58	0.58	0.56	0.55	0.56
HN-161	2460	0.45	0.46	0.47	0.46	0.44	0.38	0.41	0.44	0.45	0.46	0.46	0.47	0.45	0.43	0.46
HN-152	2590	0.13	0.13	0.14	0.11	0.10	0.07	0.06	0.06	0.06	0.08	0.10	0.13	0.10	0.07	0.12
HN-153	2990	0.11	0.10	0.11	0.09	0.09	0.08	0.07	0.08	0.08	0.08	0.10	0.11	0.09	0.08	0.10

Where, monthly values (Jan-Dec) are the Period-of-record average monthly values for a period encompassing the start date of each station and an end date of October 2011. Annual is the twelve month average value, Dry is the May to October average value; Wet is the November to April average value; yellow highlighted squares indicate monthly maxima; blue highlighted squares indicate monthly minima.

Differences in soil moisture are found across the elevation gradient (Figure 31). Slight increases in soil moisture are found between the 960 and 1640 m leeward stations as gradients transition into the cloud zone and decreases as gradients transition out of the cloud zone along the leeward transect. There is very little difference between the two highest-elevation stations, which are located in areas with highly porous soils and little vegetation cover. In general, the

leeward transect exhibited uniform spatial patterns with slightly higher values in the wet season. The largest difference between seasons occurs at the 2120 m station, which has the highest precipitation along the leeward transect (Figure 29) as well as one of the largest differences in dry and wet season precipitation among the stations (Table 11). For the windward transect, soil moisture decreases with increasing elevation but conditions are similar in the two seasons.

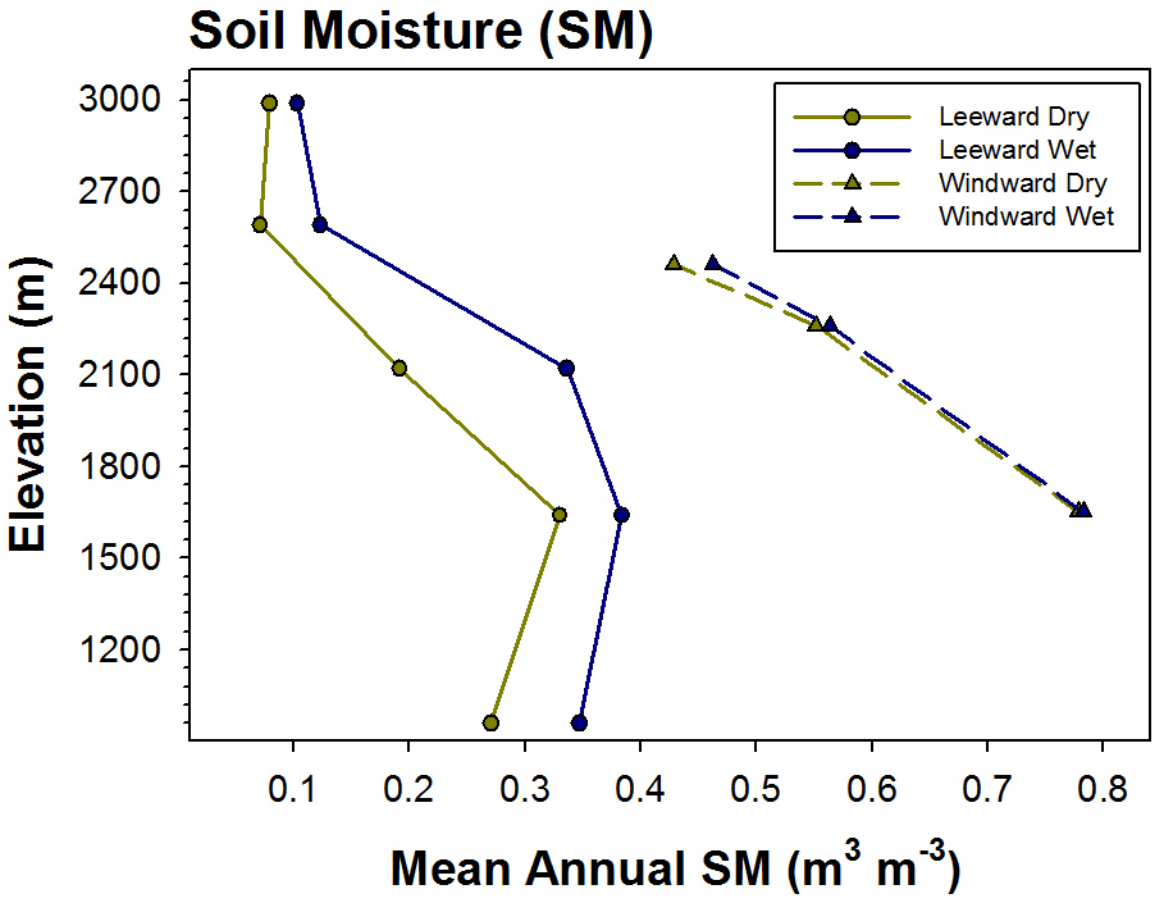

Figure 31: Vertical profiles of mean annual soil moisture along leeward (solid line, circle marker) and windward (dashed line, triangle marker) elevation transects, or dry (yellow) and wet (blue) seasons.

4.10 Soil Heat Flux

Soil heat flux (SHF) is the gain or loss of stored sensible heat energy within the soil. The rate at which this exchange occurs between the surface and the underlying soil depends on the temperature gradient and thermal conductivity of the soil (Bonan 2008). Spatial and temporal variations in soil heat flux are driven by net radiation and surface characteristics (Giambelluca et al., 2014). Annual soil heat flux (Figure 32) is in general agreement with expected patterns related to net radiation (Figure 12). In general, soil temperature increases during the warmer half of the year, which happens to correspond to the dry season in Hawai‘i, in response to a period of positive soil heat flux (Table 13). Similarly, the reduction of soil temperature during the cool (wet) season is a manifestation of negative soil heat flux. The annual cycle of SHF is most pronounced at the three highest-elevation stations, where the highest mean monthly values occur between May and June and the lowest monthly means occur between November and December. These three stations also have the largest annual cycle for net and solar radiation. Stations located at mid elevations show annual cycles that are less pronounced. It is interesting to note that the highest mean monthly SHF at the 2120 m station occurs in March, which corresponds directly with the month of low TWI frequency (Figure 2).

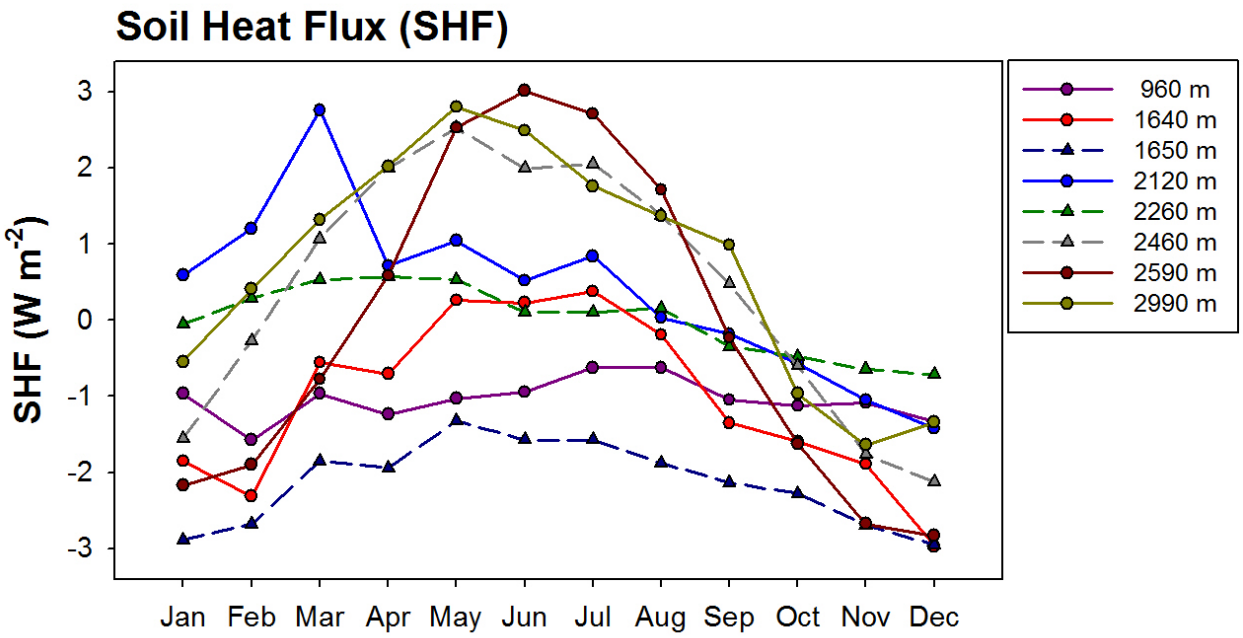

Figure 32: Mean annual cycle of soil heat flux (SHF); solid lines with a circle marker indicate leeward stations; dashed lines with a triangle marker indicate windward stations.

Table 13: Mean annual cycle of soil heat flux (W m^{-2}).

Sta ID	Elev	Jan	Feb	Mar	Apr	May	Jun	Jul	Aug	Sep	Oct	Nov	Dec	Annual	Dry	Wet
HN-119	960	-1.0	-1.6	-1.0	-1.2	-1.0	-0.9	-0.6	-0.6	-1.0	-1.1	-1.1	-1.3	-1.0	-0.9	-1.2
HN-106	1640	-1.9	-2.3	-0.6	-0.7	0.3	0.2	0.4	-0.2	-1.4	-1.6	-1.9	-3.0	-1.0	-0.4	-1.7
HN-164	1650	-2.9	-2.7	-1.9	-1.9	-1.3	-1.6	-1.6	-1.9	-2.1	-2.3	-2.7	-3.0	-2.1	-1.8	-2.5
HN-151	2120	0.6	1.2	2.8	0.7	1.0	0.5	0.8	0.0	-0.2	-0.6	-1.0	-1.4	0.4	0.3	0.5
HN-162	2260	-0.1	0.3	0.5	0.6	0.5	0.1	0.1	0.1	-0.3	-0.5	-0.6	-0.7	0.0	0.0	0.0
HN-161	2460	-1.6	-0.3	1.1	2.0	2.5	2.0	2.1	1.4	0.5	-0.6	-1.8	-2.1	0.4	1.3	-0.4
HN-152	2590	-2.2	-1.9	-0.8	0.6	2.5	3.0	2.7	1.7	-0.2	-1.6	-2.7	-2.8	-0.1	1.4	-1.6
HN-153	2990	-0.5	0.4	1.3	2.0	2.8	2.5	1.8	1.4	1.0	-1.0	-1.6	-1.3	0.7	1.4	0.0

Diurnal soil heat flux (Figure 33) is in general agreement with expected patterns related to net radiation (Figure 13). Patterns are similar for both seasons; however, the range in values is greater in the dry season, because of the higher daytime net radiation. On the leeward side of the island, the effects of clouds can be clearly identified by a marked decrease during the afternoon hours at mid elevations. For windward stations, where persistently cloudy conditions prevail (1650 to 2260 m), the diurnal cycle of SHF is the least pronounced.

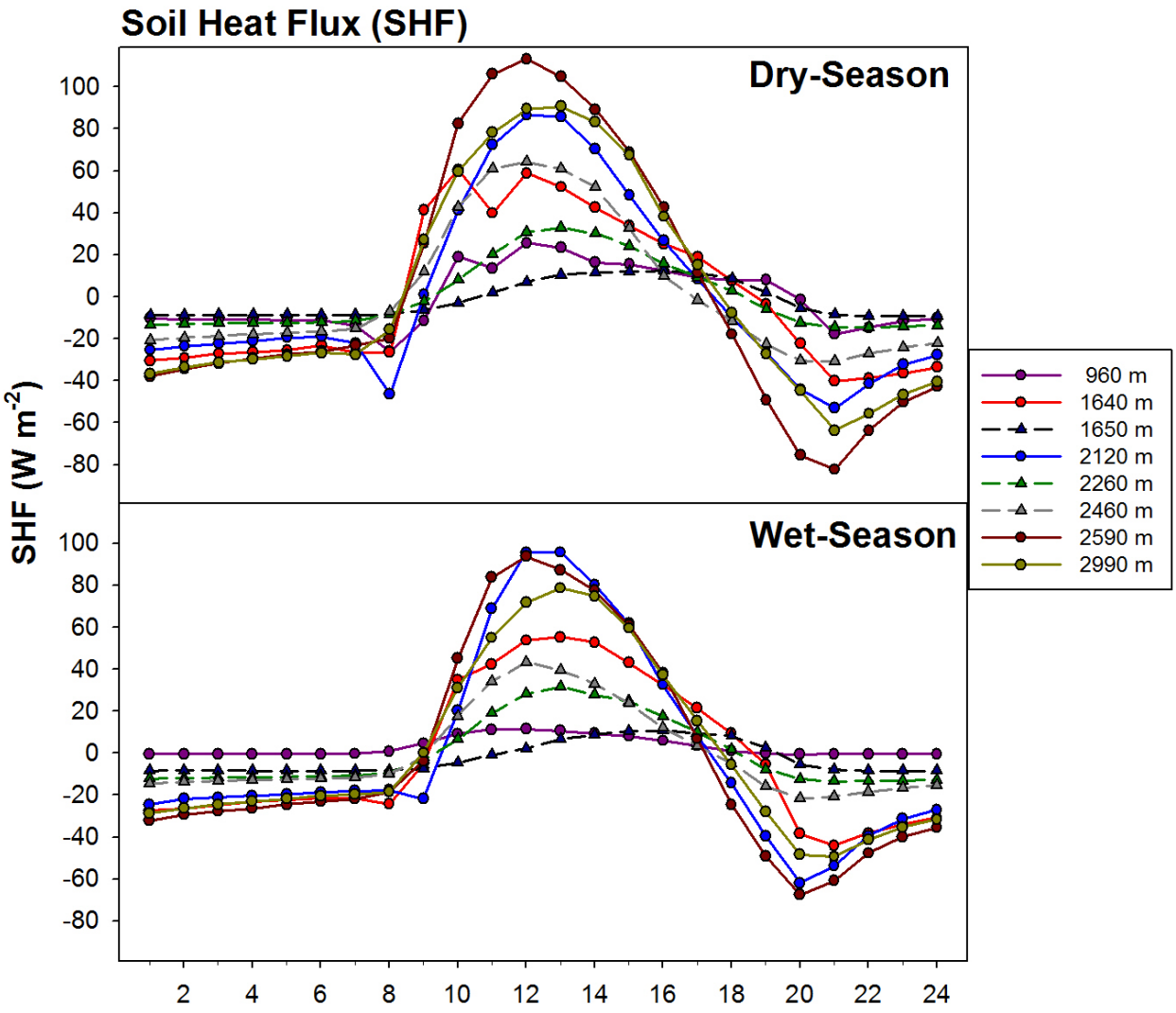

Figure 33: Diurnal cycles of soil heat flux for the dry (top) and wet (bottom) season; solid lines with a circle marker indicate leeward stations; dashed lines with a triangle marker indicate windward stations.

4.11 Potential Evapotranspiration

Potential evapotranspiration (PET) is used as a metric to describe the influences that climate has on plant transpiration, wet-canopy evaporation, and soil evaporation. In any environment PET can be used as a proxy to understand plant water relations. The moisture content and temperature of the air, the intensity of the wind, and the available energy at the surface are all factors that determine the rate at which water evaporates (Dunne and Leopold, 1978). The annual cycle of PET (Figure 34) is similar to the annual cycle of solar radiation with the highest mean monthly values occurring in either June for the highest-elevation stations or July for the mid-elevation stations and the lowest monthly values occurring in either November or December (Table 14). Annual cycles are the most pronounced at the high-elevation sites located above the mean TWI where fluctuations in available energy and moisture regimens are the greatest throughout the year. Mid-elevation stations located within the cloud and sub-cloud zones experience a less pronounced annual cycle due to the consistently high humidity and damped radiation cycle.

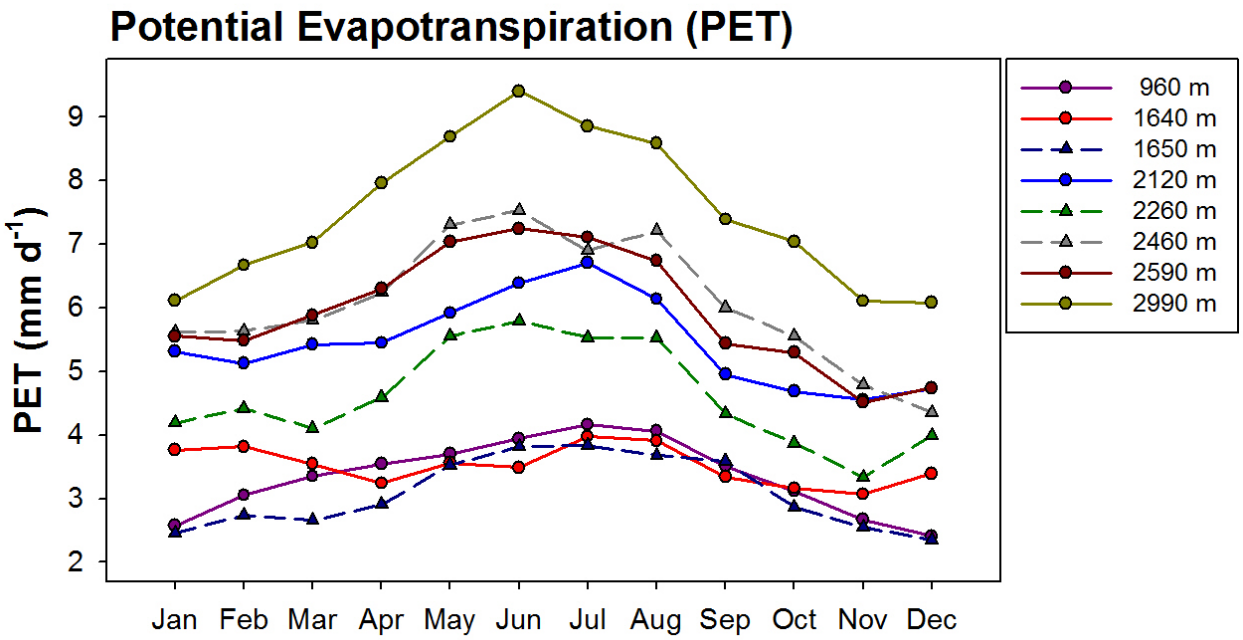

Figure 34: Mean annual cycle of potential evapotranspiration (PET); solid lines with a circle marker indicate leeward stations; dashed lines with a triangle marker indicate windward stations.

Table 14: Mean annual cycle of potential evapotranspiration (mm d^{-1}).

Sta ID	Elev	Jan	Feb	Mar	Apr	May	Jun	Jul	Aug	Sep	Oct	Nov	Dec	Annual	Dry	Wet
HN-119	960	2.6	3.1	3.4	3.5	3.7	3.9	4.2	4.1	3.5	3.1	2.7	2.4	3.3	3.7	2.9
HN-106	1640	3.8	3.8	3.5	3.2	3.6	3.5	4.0	3.9	3.3	3.2	3.1	3.4	3.5	3.6	3.5
HN-164	1650	2.5	2.7	2.7	2.9	3.5	3.8	3.8	3.7	3.6	2.9	2.5	2.4	3.1	3.6	2.6
HN-151	2120	5.3	5.1	5.4	5.4	5.9	6.4	6.7	6.1	5.0	4.7	4.6	4.7	5.4	5.8	5.1
HN-162	2260	4.2	4.4	4.1	4.6	5.5	5.8	5.5	5.5	4.3	3.9	3.3	4.0	4.6	5.1	4.1
HN-161	2460	5.6	5.6	5.8	6.2	7.3	7.5	6.9	7.2	6.0	5.6	4.8	4.3	6.1	6.7	5.4
HN-152	2590	5.6	5.5	5.9	6.3	7.0	7.2	7.1	6.7	5.4	5.3	4.5	4.7	5.9	6.5	5.4
HN-153	2990	6.1	6.7	7.0	8.0	8.7	9.4	8.9	8.6	7.4	7.0	6.1	6.1	7.5	8.3	6.7

Diurnal profiles of PET are similar to solar and net radiation profiles with low values occurring in morning, increase at sunrise, and decrease after the solar zenith hour (Figure 35). The increases in clouds and subsequent decrease in PET are observed at the leeward mid-elevation stations especially during the dry season when the TWI frequency is higher. Afternoon clouds limit the amount of energy received at the surface, decrease daytime temperatures, and increase the relative humidity, all of which contribute to lower PET. These effects are most notable at the 1640 m station in the heart of the leeward cloud zone.

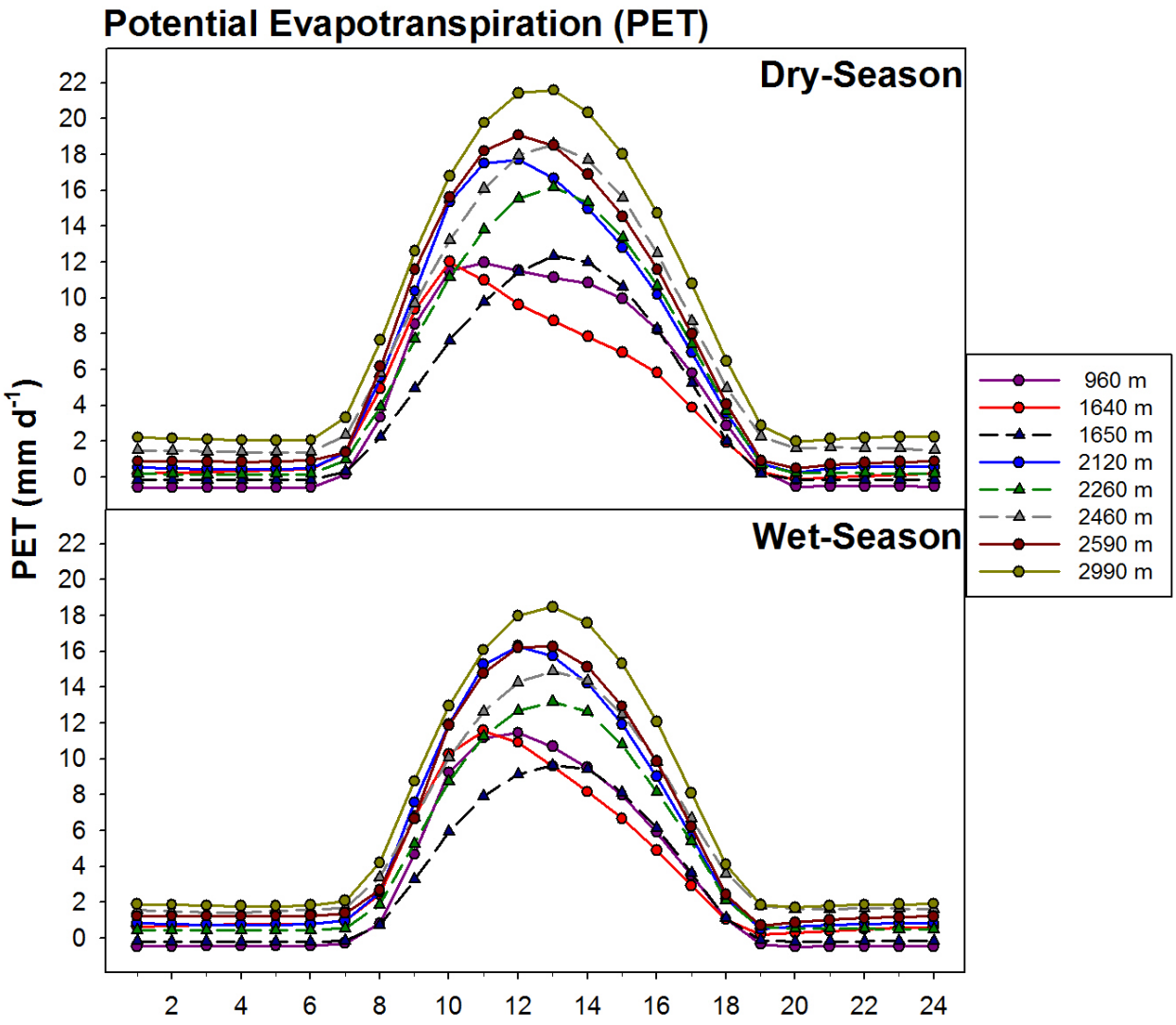

Figure 35**:** Diurnal cycles of potential evapotranspiration for the dry (top) and wet (bottom) season; solid lines with a circle marker indicate leeward stations; dashed lines with a triangle marker indicate windward stations.

Increases in elevation are associated with increases in PET along both windward and leeward transects (Figure 36). An exception to this is found at leeward station HN-106 (1640 m) where there is a slight decrease in PET is observed during the dry season. This is explained by dry season decreases in net radiation (Table 6) and similar relative humidity (Table 8) observed at the 960 m and 1640 m station, as discussed earlier. In general lower PET values are found at the mid-elevations where humidity is high and available energy is reduced by cloud attenuation of sunlight. Windward PET profiles show consistent increases in PET with increases in elevation. The range in dry and wet season minimum and maximum mean monthly values

increases with elevation above the cloud zone and the largest difference occurs at the leeward summit station (Table 14).

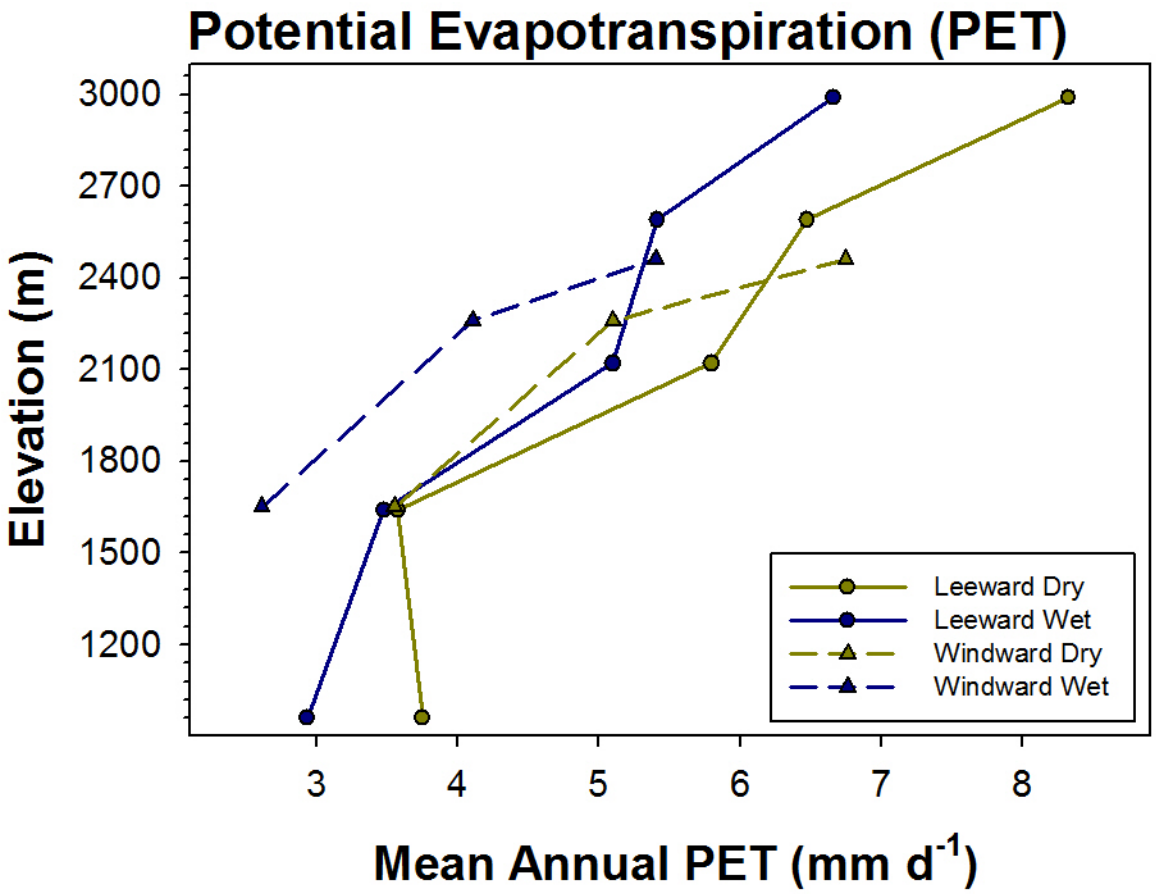

Figure 36: Vertical profiles of mean annual potential evapotranspiration along leeward (solid line, circle marker) and windward (dashed line, triangle marker) elevation transects, or dry (yellow) and wet (blue) seasons.

5. Period-of-Record Changes in Climate

The long-term (period-of-record) trends in climate variables for eight of the HaleNet stations are shown in this section. Seasonal anomalies were assessed for six of the measured (K_d, R_n, T_a, RH, WS, and P) and three of the derived (VPD, PET, and CA) variables discussed in section 4 as well as the zero precipitation days variable (ZP; discussed in section 3.3). Data were subdivided and assessed by season, elevation and exposure to the prevailing trade winds. Mid-elevation leeward stations include HN-119 (960 m) and HN-106 (1640 m; for P and ZP only). The mid-elevation windward station is HN-164 (1650 m). High-elevation leeward stations include HN-151 (2120 m), HN-152 (2590 m) and HN-153 (2990 m). High-elevation windward stations include HN-162 (2260 m), HN-161 (2460 m). The variables were evaluated for trends based on the period of record of data at each station (Table 2). Linear regression was used to characterize the behavior of climate variables over time and only time series with at least 15 years of data were used in this analysis.

Period-of-record trends in K_d vary with elevation and season (Figure 37). Statistically significant increases in dry season solar radiation (0.7 to 1.2 W m^{-2} yr^{-1}) were found at four of the five high-elevation stations located at or above the mean TWI base height (Table 15). Non-significant decreases in K_d were found below the TWI mean base height and a statistically significant decrease (-0.6 W m^{-2} yr^{-1}) is found at the leeward mid-elevation station located just below the cloud zone at HN-119 (960 m). For the wet season, regression slopes were negative at all stations except HN-151 (2120 m) on the leeward transect and only mid-elevation station HN-164 (1650 m) on the leeward transect was identified as statistically significant (-1.2 W m^{-2} yr^{-1}). A comprehensive analysis of high-elevation, long-term trends in solar radiation can be found in Longman et al. (2014).

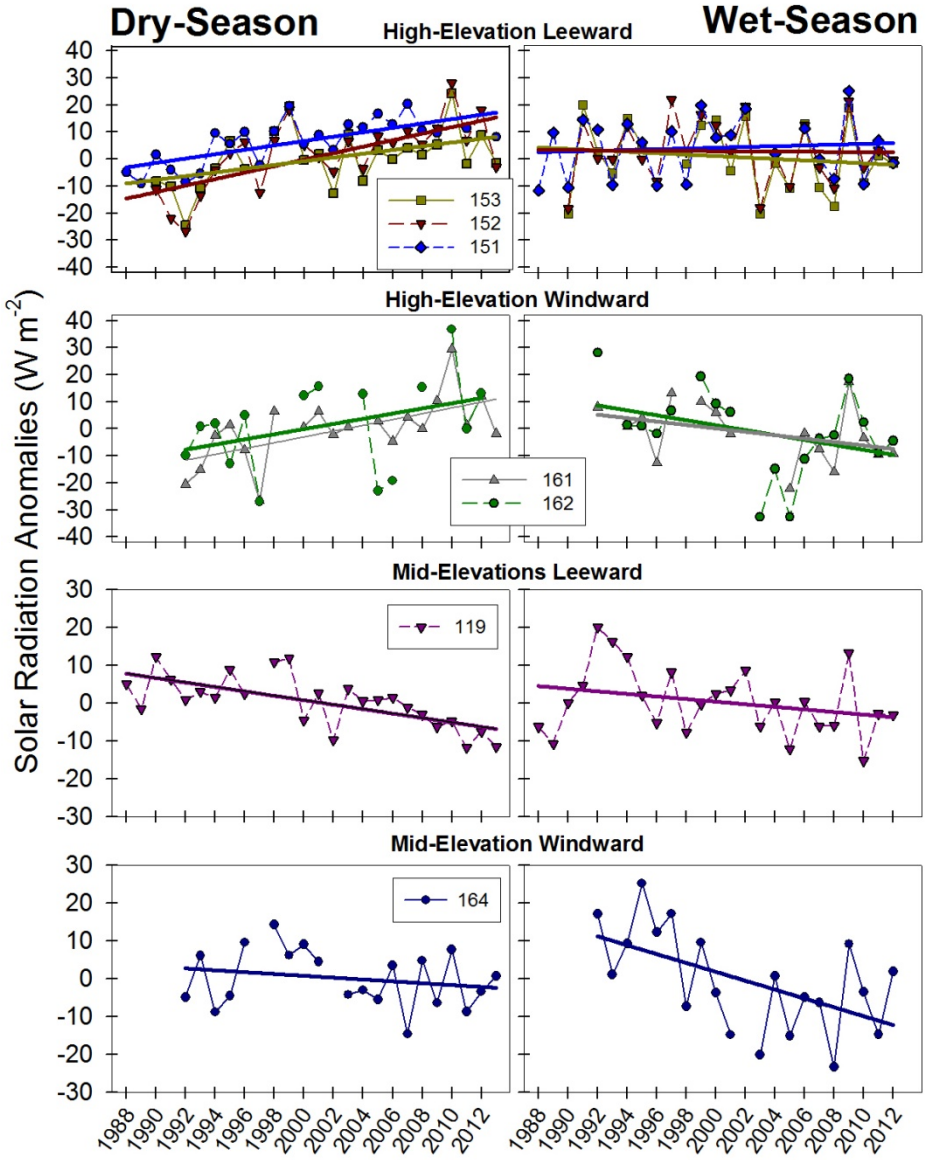

Figure 37**:** Time series of solar radiation for dry (left) and wet (right) seasons.

Table 15: Temporal trends in seasonal solar radiation over the period of 1988 to 2013.

		Dry-Season					Wet-Season				
Sta.	Elev.(m)	Trend (W m^{-2} yr^{-1})	n	r^2	SE	p	Trend (W m^{-2} yr^{-1})	n	r^2	SE	p
HN119	960	-0.6	25	0.448	0.14	0.000	-0.3	25	0.079	0.24	0.174
HN164	1650	-0.2	20	0.047	0.26	0.360	-1.2	20	0.312	0.41	0.011
HN151	2120	0.8	24	0.491	0.18	0.000	0.1	23	0.009	0.19	0.663
HN162	2260	1.0	15	0.144	0.64	0.162	-1.3	18	0.131	1.08	0.140
HN161	2460	1.1	20	0.372	0.33	0.004	-0.6	16	0.146	0.41	0.145
HN152	2590	1.2	24	0.450	0.28	0.000	-0.1	23	0.000	0.26	0.701
HN153	2990	0.7	23	0.217	0.29	0.025	-0.4	21	0.021	0.26	0.172

Trend is the slope of the regression line, n is the number of seasonal values; r^2 is the coefficient of determination; SE is the standard error of the slope (same units as Trend); p is a measure of statistical significance. Note: highlighted p-values indicated significant trends.

Period-of-record changes in CA were assessed for 7 HaleNet stations during the dry and wet seasons (Figure 38). For the dry season, increase in CA were identified at mid-elevation station HN-119 (960 m) on the leeward transect (0.2 % yr^{-1}) and significant decreases in CA were found at HN-151 (2120 m), HN-152 (2590 m) and HN-153 (2990 m) at high elevation on the leeward transect (-0.2 to -0.3 % yr^{-1}) and at the windward summit station HN-161(2460 m; -0.5 % yr^{-1}; Table 16). For the wet season, increases in CA were found at all of the stations analyzed, significant at the mid-elevation windward station HN-164 (1650 m)(0.4 % yr^{-1}).

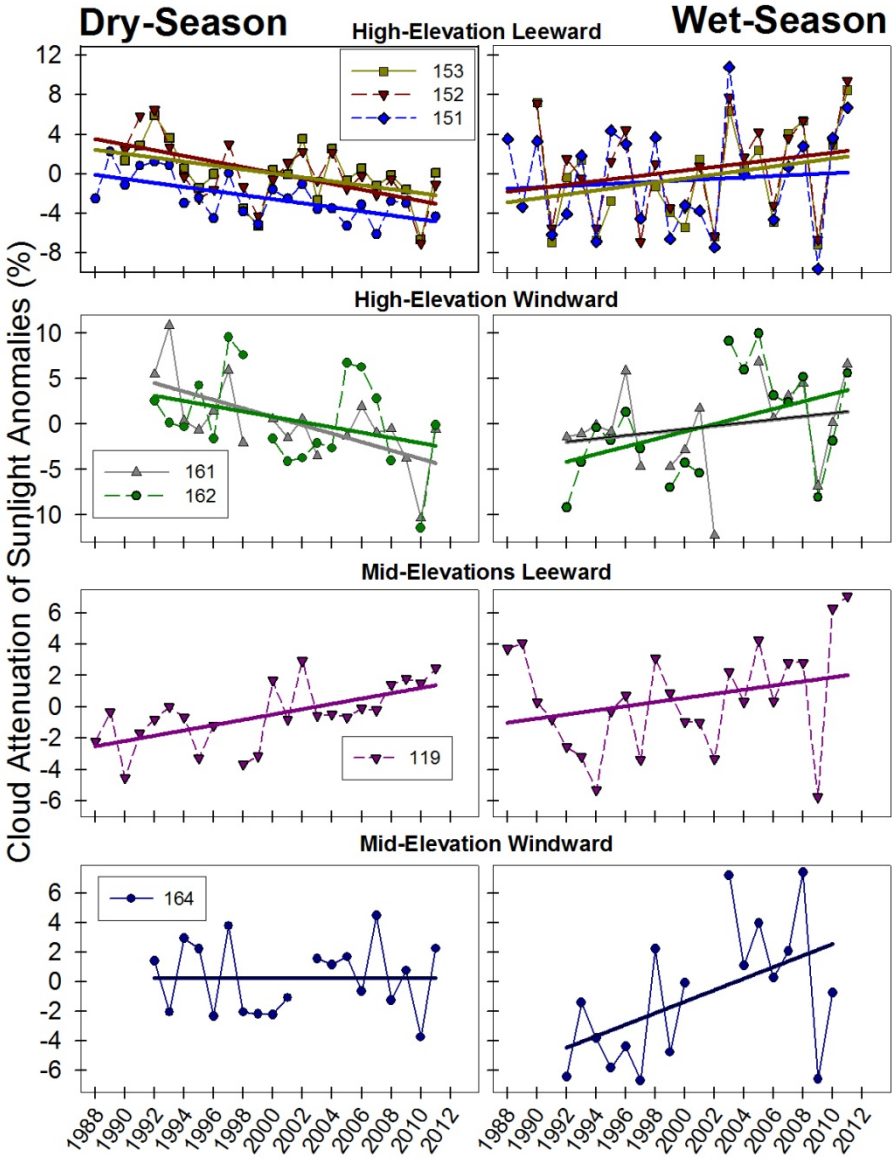

Figure 38: Time series of cloud attenuation of sunlight for dry (left) and wet (right) seasons.

Table 16: Temporal trends in seasonal cloud attenuation of sunlight over the period of 1988 to 2013.

		Dry-Season					Wet-Season				
Sta.	Elev.(m)	Trend (% yr^{-1})	n	r^2	SE	p	Trend (% yr^{-1})	n	r^2	SE	p
HN119	960	0.2	23	0.383	0.05	0.002	0.1	24	0.074	0.10	0.197
HN164	1650	0.0	19	0.000	0.10	0.978	0.4	17	0.254	0.17	0.039
HN151	2120	-0.2	23	0.396	0.06	0.001	0.2	24	0.033	0.20	0.394
HN162	2260	-0.2	15	0.099	0.19	0.254	0.4	18	0.20	0.21	0.065
HN161	2460	-0.5	18	0.417	0.14	0.004	0.2	17	0.048	0.20	0.400
HN152	2590	-0.3	22	0.350	0.09	0.004	0.2	22	0.056	0.17	0.291
HN153	2990	-0.2	21	0.198	0.09	0.043	0.1	21	0.003	0.26	0.817

Period-of-record changes in R_n were assessed for six stations during the dry season and five stations during the wet season (Figure 39). Decreases in R_n were found in both the dry and wet seasons. A statistically significant dry season decrease in R_n (-0.5 W m^{-2}) was identified at the lowest elevation (960 m) leeward station in the network (HN-119) (Table 17). For the wet season statistically significant decreases in R_n were found at HN-119 (960 m), HN-151 (2120 m), and HN-153 (2990 m) (-0.8, -0.5, and -0.7 W m^{-2} yr^{-1}, respectively).

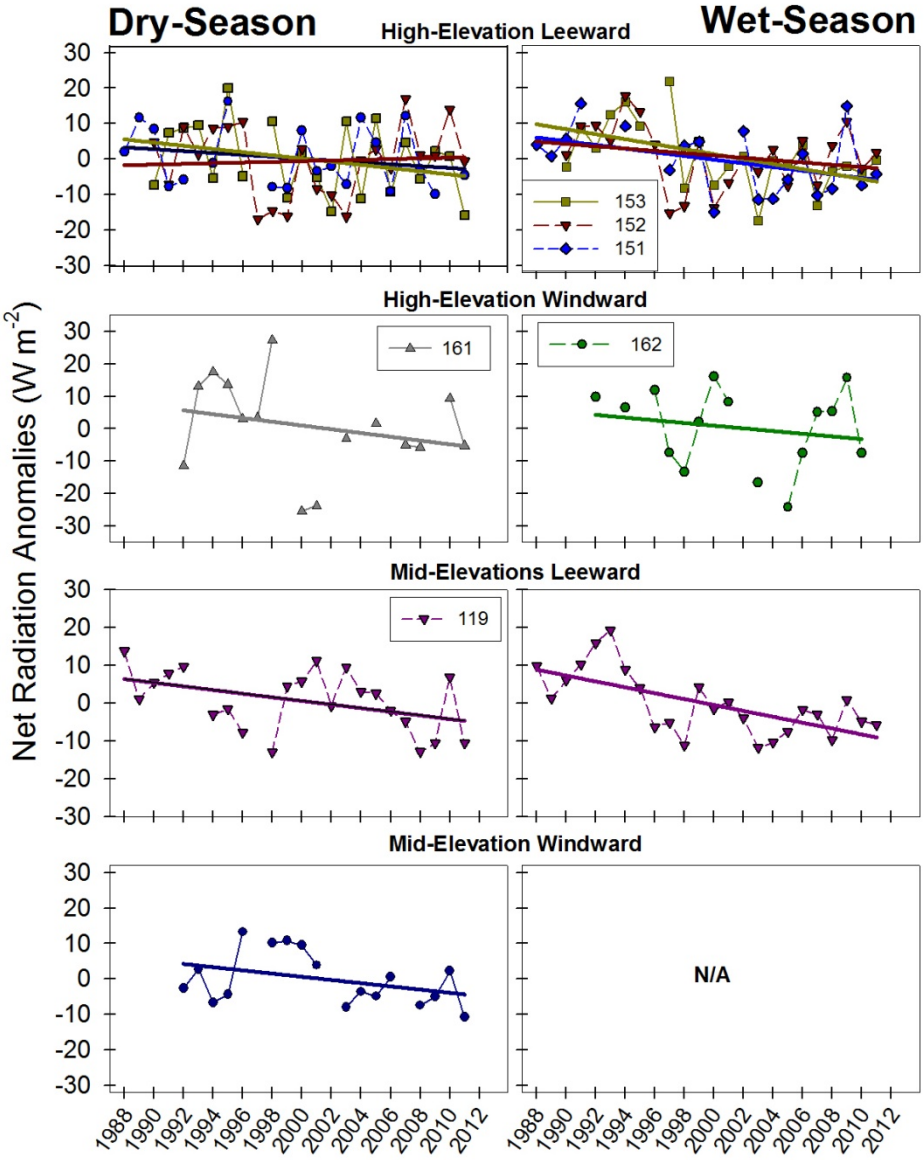

Figure 39: Time series of net radiation for dry (left) and wet (right) seasons.

Table 17: Temporal trends in seasonal net radiation over the period of 1988 to 2013.

		Dry-Season					Wet-Season				
Sta.	Elev.(m)	Trend (W m^{-2} yr^{-1})	n	r^2	SE	p	Trend (W m^{-2} yr^{-1})	n	r^2	SE	p
HN119	960	-0.5	22	0.187	0.22	0.045	-0.8	24	0.423	0.19	0.001
HN164	1650	-0.3	18	0.111	0.26	0.177		14			
HN151	2120	-0.3	20	0.051	0.27	0.339	-0.5	19	0.182	0.27	0.069
HN162	2260		14				-0.4	15	0.037	0.59	0.492
HN161	2460	-0.6	15	0.064	0.61	0.362		12			
HN152	2590	0.1	22	0.004	0.35	0.783	-0.3	22	0.057	0.30	0.285
HN153	2990	-0.4	21	0.089	0.33	0.188	-0.7	21	0.244	0.28	0.023

Period-of-record changes in T_a were assessed for seven stations during the wet and dry seasons (Figure 40). Decreases in T_a were identified at all of the stations analyzed for both dry and wet seasons (except for HN-151 (2120 m) during the dry season). Statistically significant decreases in Ta (-0.04 to -0.08˚C yr^{-1}) were identified at three windward locations and at the leeward summit station (Table 18). During the wet season significant decreases were identified at all of the stations (-0.02 to -0.08 ˚C yr^{-1}) except for HN-151 (2120 m).

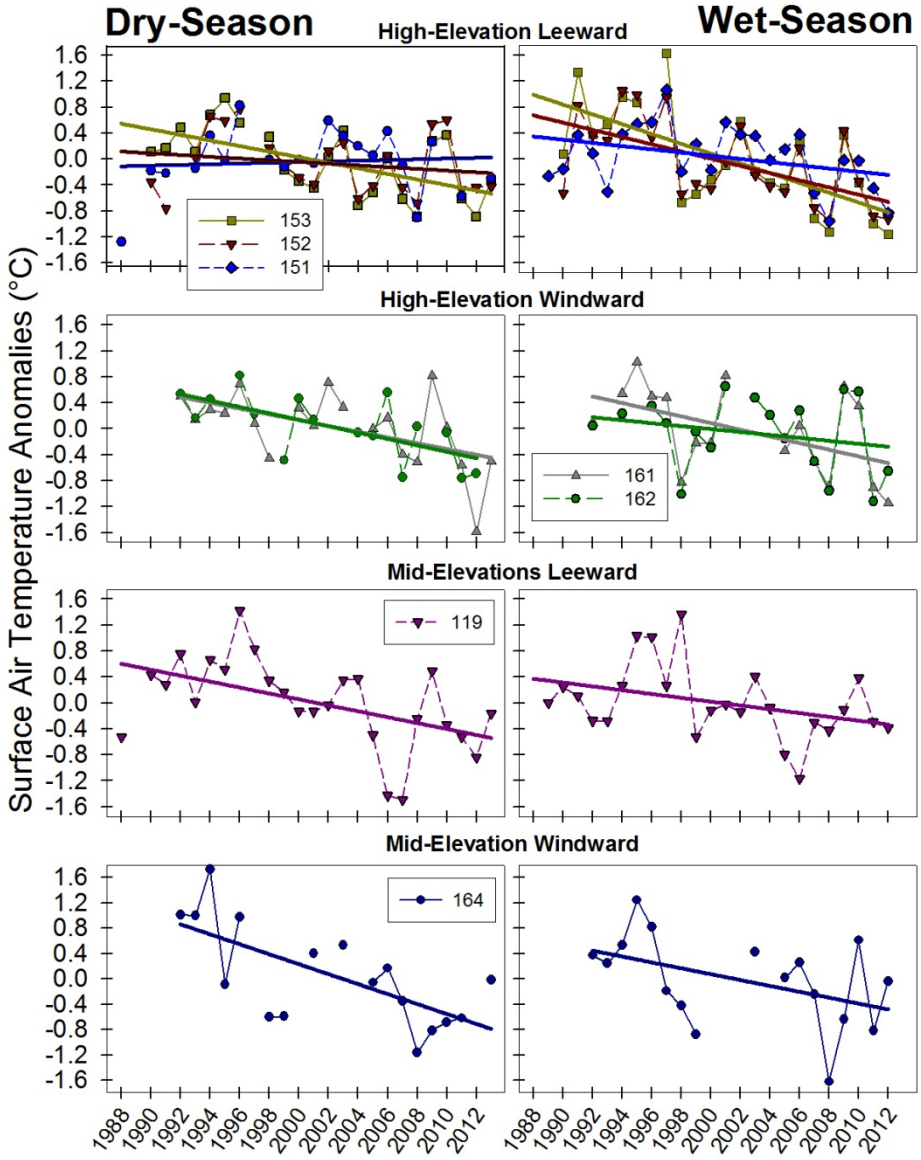

Figure 40: Time series of surface air temperature for dry (left) and wet (right) seasons.

Table 18: Temporal trends in seasonal air temperature over the period of 1988 to 2013.

		Dry-Season					Wet-Season				
Sta.	Elev.(m)	Trend (˚C yr^{-1})	n	r^2	SE	p	Trend (˚C yr^{-1})	n	r^2	SE	p
HN119	960	-0.05	25	0.255	0.02	0.010	-0.03	24	0.134	0.02	0.078
HN164	1650	-0.08	17	0.456	0.02	0.003	-0.04	17	0.193	0.02	0.078
HN151	2120	0.01	21	0.007	0.02	0.726	-0.02	24	0.131	0.01	0.082
HN162	2260	-0.05	16	0.443	0.02	0.005	-0.02	18	0.050	0.02	0.373
HN161	2460	-0.04	20	0.277	0.02	0.017	-0.05	17	0.241	0.02	0.045
HN152	2590	-0.01	22	0.039	0.01	0.381	-0.06	23	0.345	0.02	0.003
HN153	2990	-0.04	23	0.347	0.01	0.003	-0.08	22	0.437	0.02	0.001

Period-of-record changes in RH were assessed for six stations during the dry and wet seasons (Figure 41). For the dry season decreasing trends were identified at all elevations. Statistically significant decreases (-0.3 to -0.5% yr^{-1}) were identified at three of the four high elevation stations analyzed: HN-151 (2120 m), HN-161 (2460 m) and HN-152 (2590 m) (Table 19). For the wet season the highest-elevation stations showed an increase in RH, significant at windward station HN-161 (2460 m) (0.3 % yr^{-1}).

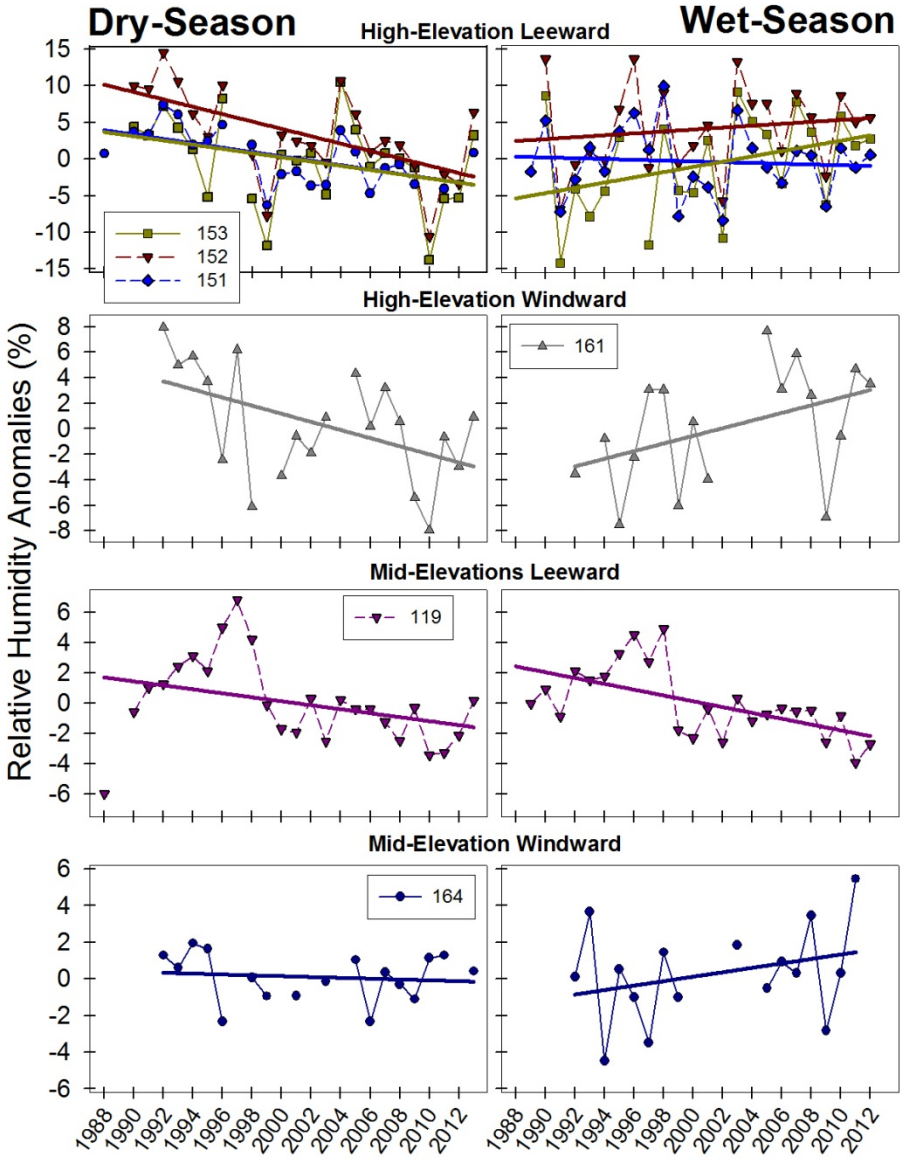

Figure 41: Time series of relative humidity for dry (left) and wet (right) seasons.

Table 19: Temporal trends in seasonal relative humidity over the period of 1988 to 2013.

		Dry-Season					Wet-Season				
Sta.	Elev.(m)	Trend (% yr^{-1})	n	r^2	SE	p	Trend (% yr^{-1})	n	r^2	SE	p
HN119	960	-0.1	25	0.117	0.08	0.095	-0.2	24	0.346	0.06	0.003
HN164	1650	0.0	17	0.017	0.05	0.621	0.1	16	0.094	0.10	0.248
HN151	2120	-0.3	22	0.332	0.09	0.005	-0.1	24	0.007	0.14	0.708
HN162	2260		13					14			
HN161	2460	-0.3	20	0.244	0.13	0.027	0.3	17	0.180	0.16	0.090
HN152	2590	-0.5	23	0.345	0.15	0.003	0.1	23	0.023	0.19	0.488
HN153	2990	-0.3	23	0.120	0.17	0.105	0.4	22	0.129	0.21	0.101

Period-of-record changes in VPD were assessed for six HaleNet stations during the dry and wet seasons (Figure 42). For the dry season increases in VPD were found at 5 of the 6 stations analyzed (Table 20) with a significant increases identified at HN-119 (2120 m, 0.02 mb yr^{-1}), HN-151 (2120 m, 0.04 mb yr^{-1}) and HN-152 (2590 m, 0.04 mb yr^{-1}). For the wet season, a significant increase in VPD was identified at the leeward 960 m station (0.02 mb yr^{-1}) and significant decreases were identified at HN-152 (2590 m) and HN-153 (2990 m) which are also part of the leeward transect (-0.03 and -0.05 mb yr^{-1}, respectively).

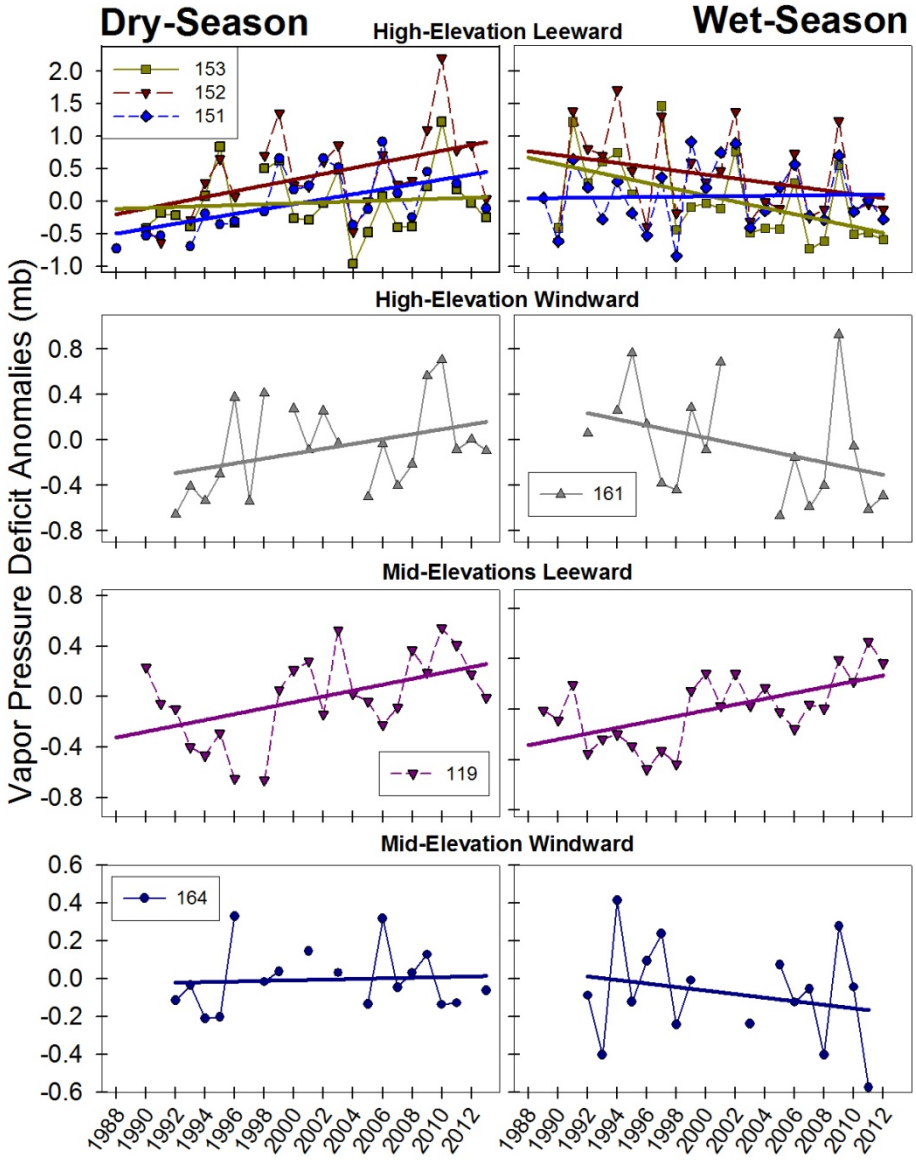

Figure 42: Time series of vapor pressure deficit for dry (left) and wet (right) seasons.

Table 20: Temporal trends in seasonal vapor pressure deficit over the period of 1988 to 2013.

		Dry-Season					Wet-Season				
Sta.	Elev.(m)	Trend (mb yr^{-1})	n	r^2	SE	p	Trend (mb yr^{-1})	n	r^2	SE	p
HN119	960	0.02	23	0.242	0.01	0.017	0.02	24	0.354	0.01	0.002
HN164	1650	0.00	17	0.005	0.01	0.796	-0.01	16	0.053	0.01	0.389
HN151	2120	0.04	21	0.331	0.01	0.006	0.00	24	0.001	0.01	0.867
HN162	2260		12					13			
HN161	2460	0.02	20	0.130	0.01	0.118	-0.03	17	0.127	0.02	0.161
HN152	2590	0.04	22	0.227	0.02	0.025	-0.03	23	0.092	0.02	0.160
HN153	2990	0.01	23	0.011	0.01	0.637	-0.05	22	0.274	0.02	0.013

Period-of-record changes in WS were assessed for six HaleNet stations during the dry and wet seasons (Figure 43). During the dry season, a significant increase in wind speed was observed at the leeward summit station (0.04 m s^{-1} yr^{-1}) and slight decreases in WS were observed along the windward transect, significant at HN-162 (2260 m; -0.05 m s^{-1} yr^{-1}; Table 21). For the wet season decreases in WS were observed at all of the stations except the leeward summit station at HN-153 (2990 m), significant at HN-119 (960 m; -0.02 m s^{-1} yr^{-1}) and HN-152 (2590 m; -0.04 m s^{-1} yr^{-1}) on the leeward transect and HN-162 (2260 m; -0.06 m s^{-1} yr^{-1}) on windward transect.

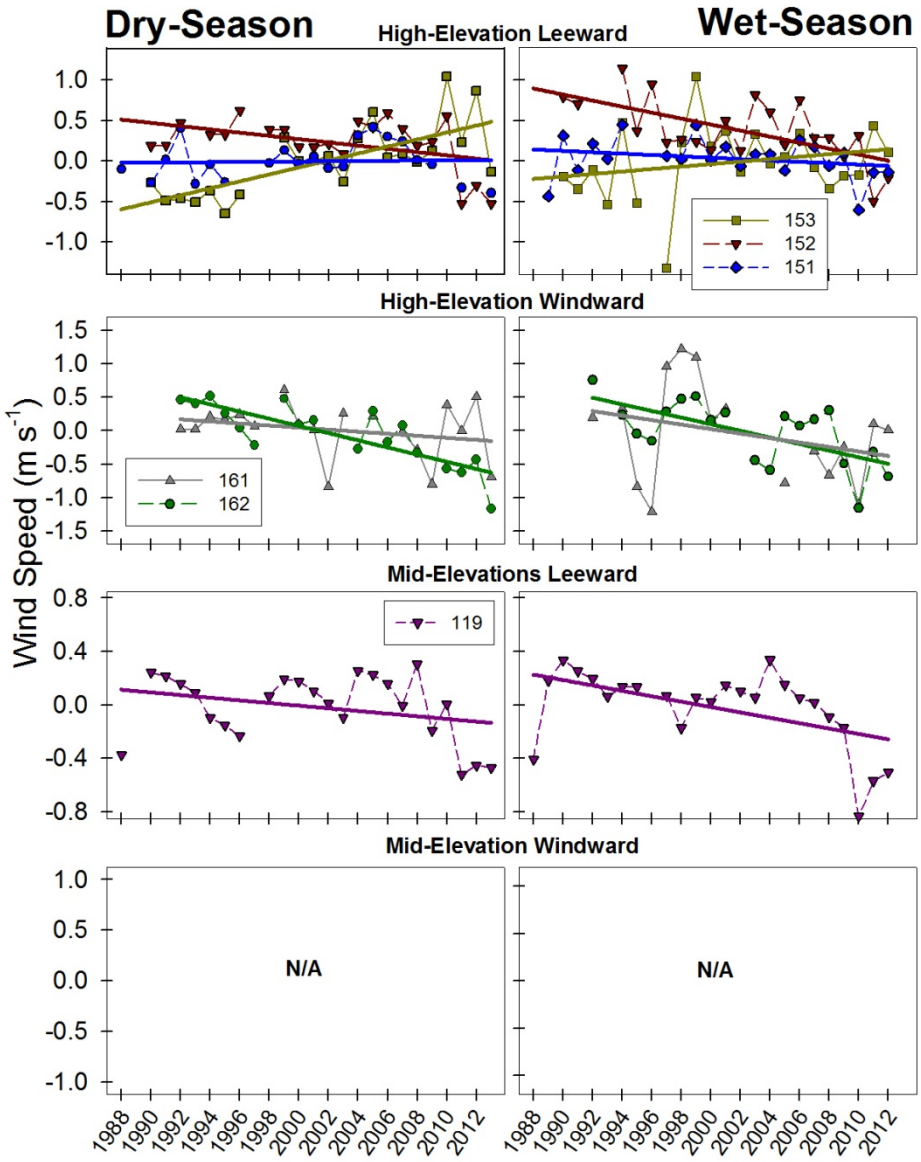

Figure 43: Time series of wind speed for dry (left) and wet (right) seasons.

Table 21: Temporal trends in seasonal wind speed over the period of 1988 to 2013.

		Dry-Season					Wet-Season				
Sta.	Elev.(m)	Trend ($m\ s^{-1}\ yr^{-1}$)	n	r^2	SE	p	Trend ($m\ s^{-1}\ yr^{-1}$)	n	r^2	SE	p
HN119	960	-0.01	24	0.092	0.01	0.150	-0.02	24	0.265	0.01	0.010
HN164	1650		14					14			
HN151	2120	0.00	21	0.002	0.01	0.851	-0.01	22	0.060	0.01	0.272
HN162	2260	-0.05	18	0.652	0.01	0.000	-0.05	19	0.396	0.02	0.004
HN161	2460	-0.02	19	0.069	0.01	0.276	-0.03	16	0.092	0.03	0.255
HN152	2590	-0.02	22	0.200	0.01	0.037	-0.04	21	0.389	0.01	0.003
HN153	2990	0.04	22	0.514	0.01	0.000	0.02	22	0.050	0.01	0.318

Period-of-record changes in P were assessed for eight HaleNet stations during the dry and wet seasons (Figure 44). For the dry season significant decreases in P (1.1 to 13.1 mm yr^{-1}) were identified at all of the stations except HN-119 (960 m) (Table 22). For the wet season, six of the eight stations analyzed show decreasing trends in P, none of which were determined to be significant.

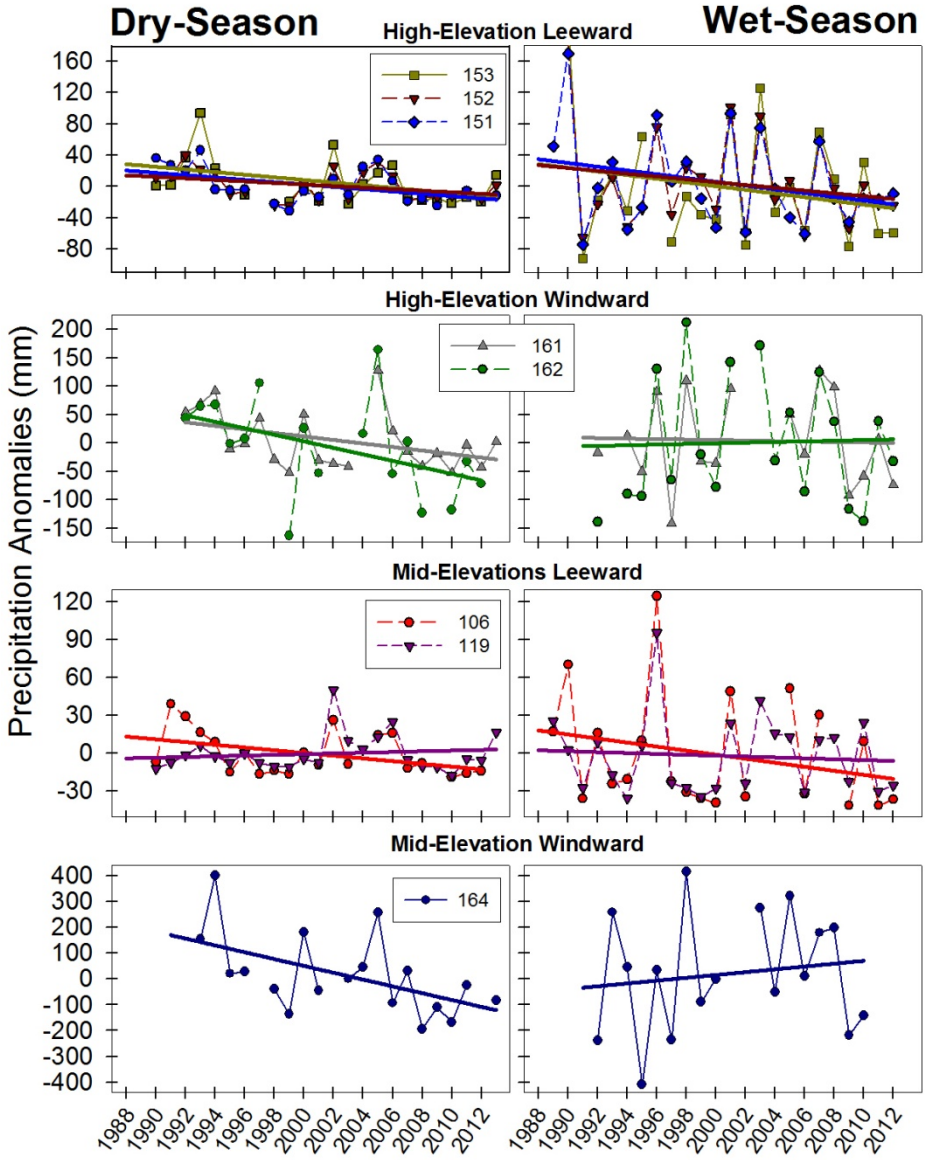

Figure 44: Time series of precipitation for dry (left) and wet (right) seasons.

Table 22: Temporal trends in seasonal precipitation over the period of 1988 to 2013.

		Dry-Season					Wet-Season				
Sta.	Elev.(m)	Trend (mm yr^{-1})	n	r^2	SE	p	Trend (mm yr^{-1})	n	r^2	SE	p
HN119	960	0.3	24	0.018	0.44	0.531	-0.4	24	0.006	0.94	0.713
HN106	1640	-1.1	21	0.178	0.53	0.057	-1.6	21	0.067	1.37	0.257
HN164	1650	-13.1	18	0.274	5.34	0.026	5.5	17	0.020	9.85	0.586
HN151	2120	-1.5	21	0.213	0.65	0.035	-2.4	24	0.081	1.73	0.179
HN162	2260	-5.8	17	0.202	2.96	0.070	0.6	19	0.001	4.36	0.897
HN161	2460	-3.1	21	0.168	1.59	0.065	-0.4	17	0.001	3.14	0.893
HN152	2590	-1.0	23	0.140	0.53	0.078	-1.8	23	0.039	1.95	0.367
HN153	2990	-1.7	21	0.175	0.83	0.059	-2.4	22	0.047	2.38	0.334

Period-of-record changes in ZP were assessed for seven HaleNet stations during the dry season and 8 stations during the wet seasons (Figure 45). For the dry season, increases in ZP were identified at all of the stations except station mid-elevation station HN-119 (960 m) (Table 23). Statistically significant increases were identified at the four leeward stations found above 1600 m (0.4 to 0.7 % yr^{-1}). For the wet season non-significant decreases in ZP were found at six of the eight stations.

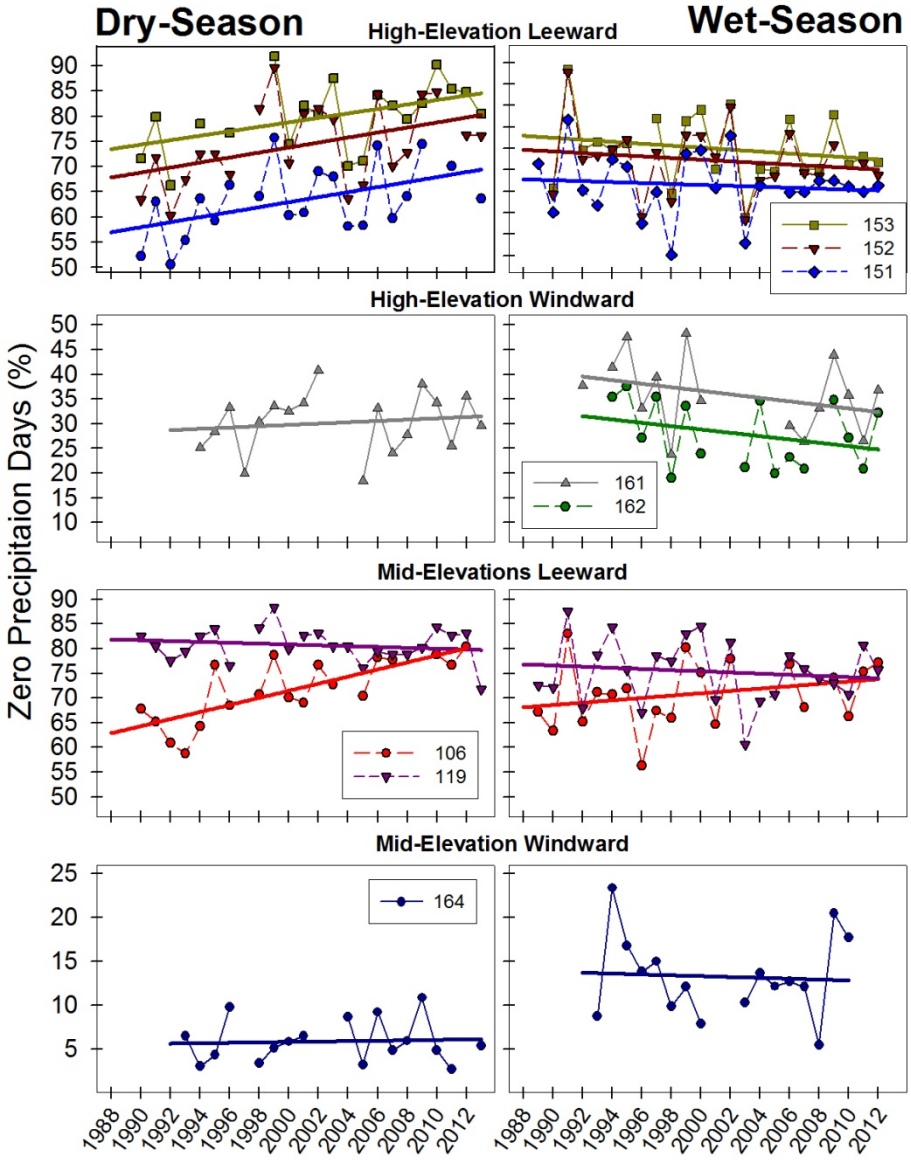

Figure 45: Time series of zero precipitation days for dry (left) and wet (right) seasons.

Table 23: Temporal trends in seasonal zero precipitation days over the period of 1988 to 2013.

		Dry-Season					Wet-Season				
Sta.	Elev.(m)	Trend (% yr^{-1})	n	r^2	SE	p	Trend (% yr -1)	n	r^2	SE	p
HN119	960	-0.1	23	0.031	0.10	0.425	-0.1	24	0.017	0.19	0.542
HN106	1640	0.7	19	0.590	0.14	0.000	0.2	20	0.071	0.20	0.257
HN164	1650	0.0	17	0.004	0.10	0.818	0.0	16	0.004	0.22	0.826
HN151	2120	0.5	21	0.244	0.20	0.023	-0.1	23	0.012	0.22	0.620
HN162	2260		14				-0.3	16	0.091	0.29	0.256
HN161	2460	0.1	18	0.019	0.24	0.583	-0.4	15	0.110	0.28	0.227
HN152	2590	0.5	22	0.190	0.23	0.042	-0.2	22	0.026	0.26	0.475
HN153	2990	0.4	20	0.221	0.20	0.037	-0.2	22	0.039	0.26	0.380

Period-of-record changes in PET were assessed for four HaleNet stations during the dry and wet seasons (Figure 46). For the dry season, increases in PET were found along the leeward transect except at HN-119 (960 m)(Table 24) and significant trends were identified at the three high-elevation leeward stations HN-151 (2120 m; 0.02 mm d^{-1} yr^{-1}), HN-152 (2590 m; 0.04 mm d^{-1} yr^{-1}) and HN-153 (2990 m; 0.04 mm d^{-1} yr^{-1}). For the wet seasons, decreases in PET were identified across the leeward gradient and significant decreases were found at the lowest (HN-119, 960 m) and highest (HN-153, 2990 m) stations (-0.02 and -0.06 mm d^{-1} yr^{-1}, respectively). PET was not calculated for any of the windward stations due to limitations in available data.

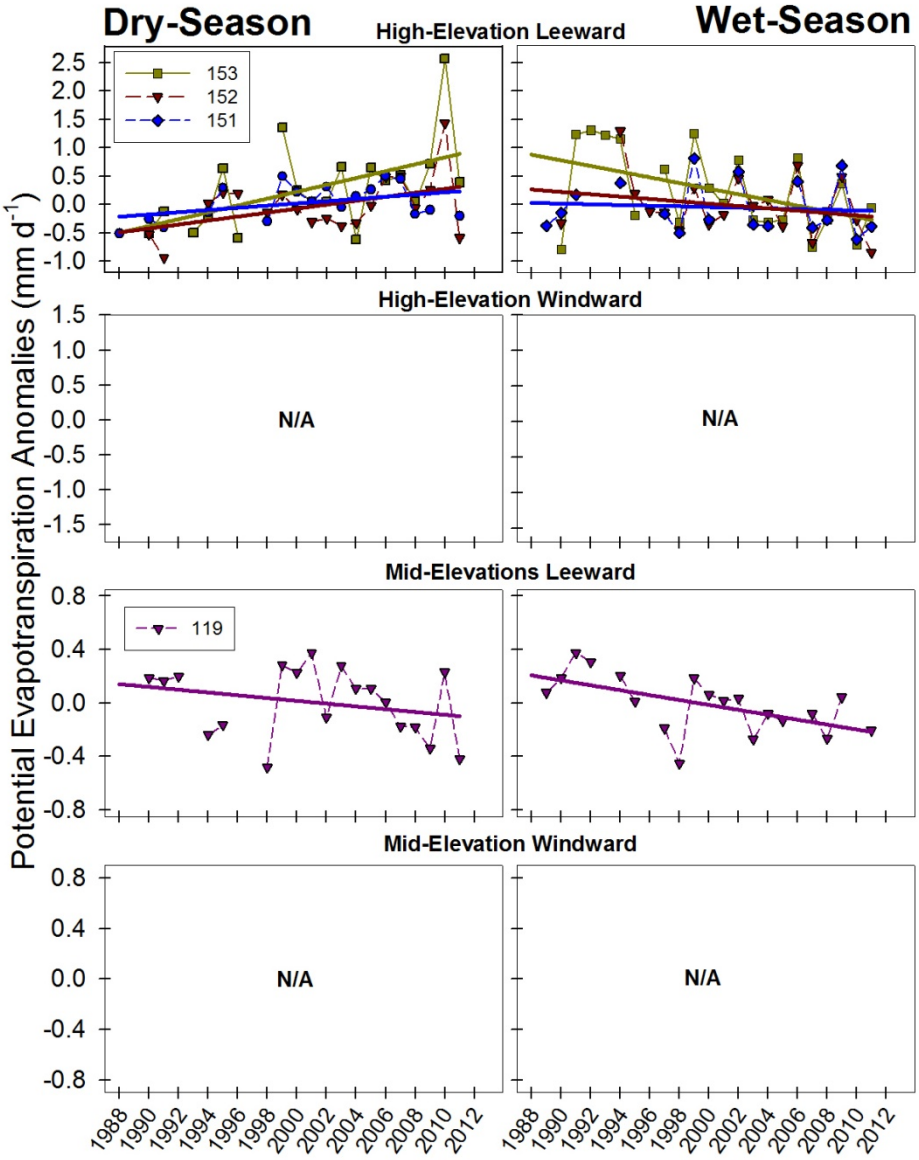

Figure 46: Time series of potential evapotranspiration for dry (left) and wet (right) seasons.

Table 24: Temporal trends in potential evapotranspiration over the period of 1988 to 2011.

		Dry-Season					Wet-Season				
Sta.	Elev.(m)	Trend (mm d^{-1} yr^{-1})	n	r^2	SE	p	Trend (mm d^{-1} yr^{-1})	n	r^2	SE	p
HN119	960	-0.01	19	0.079	0.01	0.243	-0.02	19	0.345	0.01	0.008
HN164	1650		8					8			
HN151	2120	0.02	18	0.168	0.01	0.092	-0.01	17	0.011	0.02	0.689
HN162	2260		10					10			
HN161	2460		14					11			
HN152	2590	0.04	19	0.268	0.02	0.014	-0.02	19	0.066	0.02	0.288
HN153	2990	0.06	19	0.256	0.02	0.023	-0.05	21	0.208	0.02	0.038

Linear trends are assessed for TWI base height and frequency of occurrence (Figure 47). Increases in TWI base height were observed in both the dry (6 m $decade^{-1}$; p = 0.82) and wet (33 m $decade^{-1}$; p = 0.10) seasons although trends were only significant in the wet season. For TWI frequency of occurrence an opposite trend was identified in each season (Table 25). For the dry season, increases in TWI frequency were identified (4 % $decade^{-1}$; p = 0.04) and for the wet season decrease were shown (-2 % $decade^{-1}$; p = 0.30).

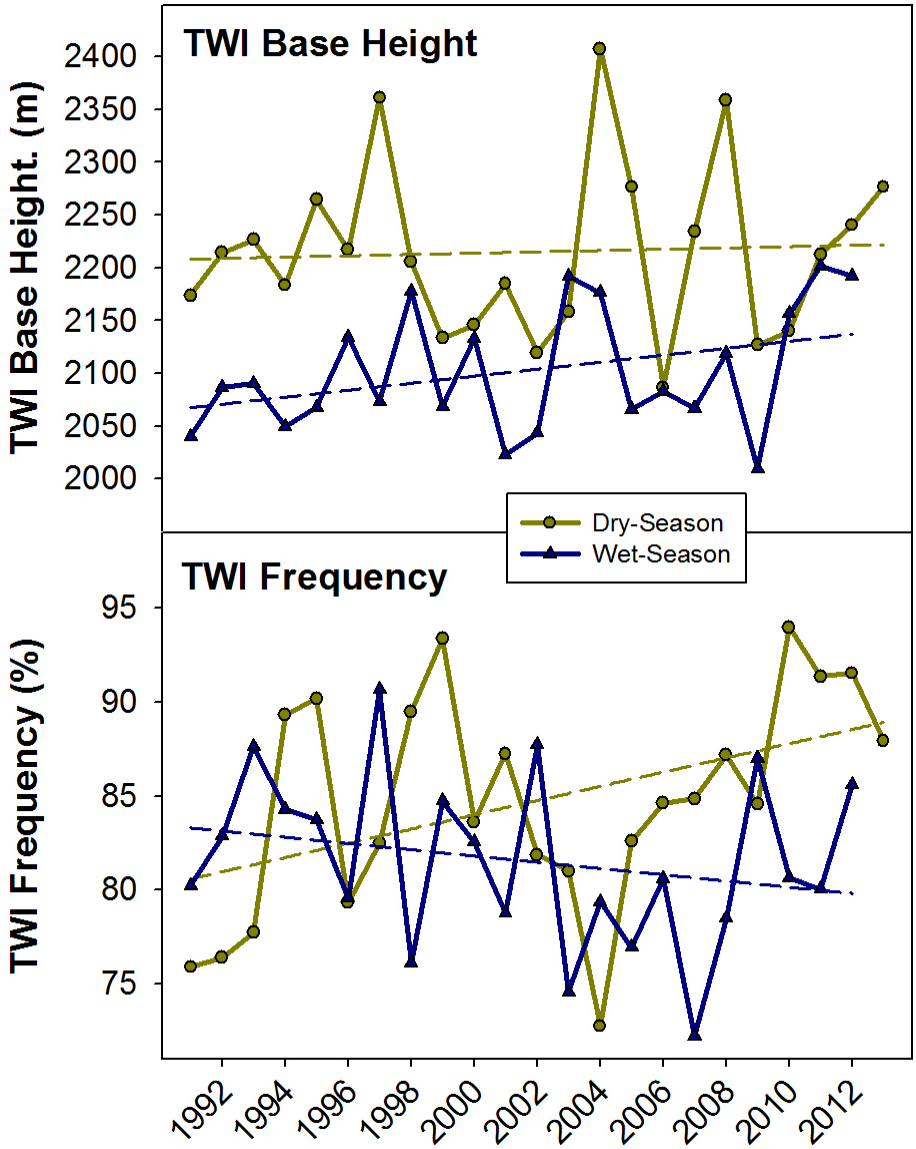

Figure 47: Time series of TWI base height (top) and frequency of occurrence (bottom) from 1991 - 2013.

Table 25: Temporal trends in seasonal TWI characteristics over the period of 1991 to 2013.

Base Height	Trend (m yr^{-1})	n	r^2	SE	p
Dry-season	0.6	23	0.003	2.63	0.816
Wet-seasion	3.3	22	0.132	1.90	0.097
Freqeuency	**Trend (% yr^{-1})**				
Dry-season	0.4	23	0.194	0.17	0.035
Wet-seasion	-0.2	22	0.054	0.15	0.296

6. Discussion

Haleakalā is one of the highest mountains of any oceanic island in the world. The eleven climate variables analyzed in this report show distinct, elevation-dependent, vertical profiles that are clearly influenced by the combined effects of surface topography, exposure to prevailing winds, and the presence or absence of the TWI. The presence of the TWI creates persistently clear sky conditions at the highest elevations and defines the upper boundary of a moisture rich cloud zone at middle elevations along the mountain slopes. Long-term changes in climate are apparent across both leeward and windward gradients and are characterized in this report as the percentage of decadal changes to energy and moisture regimes over time. For the dry season, a mixed signal of changes in energy and a clear decrease in moisture was observed, most notably at the highest elevations (Table 26). In terms of energy, significant increases in K_d (3% to 4% decade^{-1}) and decreases in CA (-2% to -5% decade^{-1}) were observed at leeward and windward high-elevation sites. Changes to these parameters suggest decreases in cloud cover at high elevations. Longman et al. (2014) showed through an analysis of satellite derived cloud observations, decreases in dry season high-elevation cloud cover amounting to -6% to -8% per decade (1998 -2012). Decreases in cloud cover are at least partially explained by the 4% per decade increase in dry season TWI frequency of occurrence observed in this study (Table 25). Reported decreases in CA and subsequent increases in K_d do not explain the observed decreases in T_a reported here. Significant decreases in T_a observed at three windward locations and the leeward summit station were found in this analysis (-0.4 °C to -0.8 °C decade^{-1}, Table 18). Decreases in temperature may be explained by localized effects such as changes to the wind patterns or they may be part of a large signal of decreased temperatures observed globally over the past ~decade (e.g England et al., 2014). Regarding moisture, a significant drying trend is apparent at all of the stations located above 1000 m. Observations indicate significant decreases in dry season RH (-3% to -5% decade^{-1}), and P (-3% to -8% decade^{-1}) and increases in VPD (9% to 10% decade^{-1}), PET (3% to 7% decade^{-1}) and ZP (4 to % decade^{-1}) found at two or more of the five high-elevation stations. In addition, the leeward cloud zone station located at 1640 m showed a significant decrease in P (-5% decade^{-1}) and an increase in ZP (7% decade^{-1}). The windward mid-elevation station HN-164 also showed decreases in P (-3% decade^{-1}). In general, the consistency of change among the stations and the abundance of significant trends add

confidence to the conclusion that decadal-scale drying has occurred during the dry season along both leeward and windward transects and potential increases in the TWI frequency of occurrence or changes in the base height during the dry season are a plausible explanation.

Significant increases in the TWI frequency of occurrence during the dry season are a likely explanation. Longman (2015) has shown a significant relationship between ENSO variability and TWI frequency between 1991- 2013. During the negative (La Niña) phase of ENSO, TWI frequency is significantly higher than during the positive (El Niño) phase for the dry season. Longman (2015) suggests that a predominantly negative signal in ENSO over the past ~2 decades has driven the increase in dry season TWI frequency shown here. In general, agreement was seen among the atmospheric variables analyzed (especially at the high-elevation sites) regarding a trend toward drier conditions over time. For 39 of the 63 dry season time series analyzed (62%), trends were determined to be statistically significant and for the five moisture variables analyzed at high-elevation stations, 15 of the 20 time series (75%) showed significant drying.

For the wet season, many of the climate variables showed decadal trends opposite of the dry season signal (Table 27). Regarding energy, decreases in available energy were identified for all of the variables at most of the stations analyzed. Decadal decreases in K_d and increases in CA were found along leeward and windward gradients with significant decreases in K_d (-12.5% decade) and CA (3.9 % decade^{-1}) identified at the mid-elevation windward station HN-164 (1650 m). Significant decreases in R_n (-4 to -8% decade^{-1}) were observed at three of the six stations analyzed and showed a consistent decreases in T_a (-0.2 °C to -0.10 °C decade^{-1}) were found at all stations and determined to be statistically significant at all of the stations except HN-151(2120 m)(Table 18). Decreases in the wet season TWI frequency (2% decade^{-1}) may explain some of these decreases. For moisture variables a mixed signal is observed. Decreases in precipitation were observed at all of the stations but regression slopes were small (-1 to -4% decade^{-1}) and not significant. RH increased at 3 of the 4 high-elevation stations (HN151, HN-152, and HN-161), significant at windward station HN-161 (2460 m), and VPD decreased at the same three stations, significant at HN-152 (2590 m) and HN-153 (2990 m). Decreases in available energy and increases in moisture are potentially explained by a decrease in the TWI frequency of occurrence or increases in base height although significant wet season trends were less abundant compared to the dry season.

Table 26: Percent change in dry season climate variables.

Trend decade^{-1}		ENERGY				MOISTURE				
Dry-Season		K_d	CA	R_n	WS	RH	VPD	P	ZP	PET
Sta.	Elev.(m)	%	%	%	%	%	%	%	%	%
HN119	960	-2.8	1.7	-4.0	-6.3	-1.3	8.3	2.1	-0.8	-3.0
HN106	1640							-5.0	7.2	
HN164	1650	-1.4		-1.8		-0.2	3.8	-3.2	0.2	
HN151	2120	3.0	-2.1	-1.6	0.5	-3.0	10.4	-4.7	5.0	3.3
HN162	2260	4.0	-2.3		-14.6			-3.1		
HN161	2460	3.6	-4.6	-3.0	-2.6	-3.2	8.7	-3.7	1.3	
HN152	2590	3.9	-2.8	0.6	-6.6	-5.0	8.9	-4.0	5.0	6.3
HN153	2990	2.0	-2.0	-2.4	9.5	-2.9	1.7	-7.8	4.4	6.7

Where K_d is the solar radiation; CA is daytime cloud attenuation of sunlight; R_n is net radiation; WS is wind speed; RH is relative humidity; VPD is vapor pressure deficit; P is precipitation; ZP is zero precipitation days; PET is potential evapotranspiration; Blue shaded squares indicate decreases in energy and increases in moisture and Orange shaded squares indicate increases in energy and decreases in moisture; All decadal trends are presented in units of % and significant trends are given in red; it is not appropriate to calculate T_a as a percent so it is not included in the table (see table 17).

Table 27: Percent change in wet season climate variables.

Trend decade^{-1}		ENERGY				MOISTURE				
Wet-Season		K_d	CA	R_n	WS	RH	VPD	P	ZP	PET
Sta.	Elev.(m)	%	%	%	%	%	%	%	%	%
HN119	960	-3.8	1.3	-8.3	-12.0	-1.9	9.9	-1.0	-1.2	-6.8
HN106	1640							-3.5	2.4	
HN164	1650	-12.5	3.9	-1.1		1.2	-12.6	1.0	-0.5	
HN151	2120	2.0	1.8	-4.2	-2.7	-0.5	0.7	-3.1	-1.1	-1.3
HN162	2260	-17.9	4.2	-3.4	-13.3			0.2	-3.4	
HN161	2460	-9.5	1.7		-5.9	3.0	-11.0	-0.3	-3.6	
HN152	2590	-2.2	1.8	-2.9	-10.4	1.3	-7.3	-2.9	-1.9	-4.2
HN153	2990	-8.6	0.6	-5.1	3.5	3.6	-15.5	-3.4	-2.3	-7.5

Decreases in available energy and increases in moisture are potentially explained by a decrease in the TWI frequency of occurrence or increases in base height (Table 25). During the negative (La Niña) phase of ENSO, TWI frequency is significantly lower than during the positive (El Niño) phase for the wet season (Longman, 2015). Longman (2015) suggests that a predominantly negative signal in ENSO over the past ~2 decades has driven the decrease in wet

season TWI frequency shown here. High-elevation decreases in wet season precipitation are not in agreement with a wetter signal shown by the other moisture variables analyzed, however, when the years 1988, 1989 and 1990 are removed from the precipitation time series, decreases are not detected (Longman, 2015).

A clear relationship can be seen between TWI variations and changes in energy and moisture variables along the slopes of the mountains. However, the causes of TWI variability are not clearly understood. Longman (2015) has shown significant correlations between TWI frequency and the ENSO and the PDO indices when time series are compared over the most recent two decades of data. Interestingly, cool phase ENSO and cool phase PDO are negatively correlated with the dry season TWI frequency and positively correlated with wet season TWI frequency (Longman, 2015). Current research efforts are focused on determining the role that these Pacific-centered modes of climate variability have on TWI variability and the subsequent effects TWI variability has on water regimes at high and mid elevations (Longman, 2015).

Again, it is important to note that of the 65 wet season time series analyzed only 22 trends were determined to be statistically significant (34%) and of the five high elevation moisture variables analyzed, a significant wetter signal was observed only at the leeward summit station (HN-153).

7. Conclusions

A detailed knowledge of the climate at any given elevation is critically important for a variety of resource management issues, including ground water and surface water development and protection, controlling and eradicating invasive species, protecting and restoring native ecosystems, and planning adaption strategies to address the effects of global warming (Giambelluca et al., 2014). HaleNet climate monitoring and the subsequent analyses of observed climate variability along the slopes of Haleakalā is a tool that can be useful for resource managers to better inform protection of the native plant and animals that reside there. Also, these data can be used as a proxy to understand how other mountain ecosystems function in the state where measurements are not available. In a recent effort aimed at mapping a number of climate variables at a 250 m resolution for the entire State of Hawai‘i, Giambelluca et al. (2014) have used HaleNet data to calibrate and validate a number of climate models used in the mapping effort. In addition, the growing length of record makes the HaleNet data set increasingly valuable

in understanding expected future changes to high-elevation ecosystems in Hawai‘i. Recent research endeavors that have made use of HaleNet observations have addressed changes in temperature (Giambelluca et al., 2008), moisture (Crausbay and Hotchkiss, 2010; Longman et al., in review), vegetation (Krushelnycky et al., 2013, Crausbay et al., 2014), and solar radiation (Longman et al., 2014) along the slopes of Haleakalā.

The goal of this report is to bring awareness of the climate diversity that exists along the slopes of Haleakalā Volcano and to the changes that are occurring there. The authors hope that this report will serve to stimulate further ecological research incorporating climatic events and processes in Hawai‘i, with an aim of informing successful research and management strategies for preserving native Hawaiian ecosystems and properly managing freshwater resources. Changes in moisture may affect vegetation characteristics, promote the spread of invasive species, and decrease water recharge to the aquifers. These changes are amplified by the time scales by which they are occurring. The faster the climate changes, the less time native species will have to react to these changes and the area in which these species have a competitive advantage may shrink.

Hawai‘i may prove to be highly relevant in the discussion on global climate change impacts. The HaleNet data is a resource and a tool that can help us better understand changing signals in the Earth’s climate, especially at high elevations. The findings in this report suggest that high-elevation climates in Hawai‘i are changing through time and that these changes are potentially driven by the variability of TWI frequency. Time series assessed over ~25 year periods may not be a sufficient amount of time to identify a robust change in climate; however these types of assessments can provide valuable information used to guide future research design. Further research is needed to determine how climates are changing are changing through time and the impacts that these changes have on high elevation ecosystems in Hawai‘i. Undoubtedly, the HaleNet data archive will be an essential tool moving forward with these and other important research questions.

8 Past and On-Going Research Projects on Haleakalā

8.1: Auwahi Dry-land Forest Restoration Project

The Hawaiian dryland montane forest is considered one of the most biologically diverse ecosystems in the islands; however less than 10% of Hawai‘i’s original dry land forest remains (Medeiros and von Allmen, 2006). The southwestern leeward slopes of Haleakalā Volcano were once covered with healthy dryland forests but these forests have been severely impacted by invasive species, human development, fire and agricultural practices. Feral ungulates, including goats, pigs, cattle, and sheep have consumed the native vegetation, and fire prone alien grasses now dominate the understory in most dryland forest ecosystems. Native Hawaiian plants did not evolve with mammalian herbivores or frequent disturbance, so they do not survive well under these increased pressures (Medeiros and von Allmen, 2006). In recent decades, a multi-agency collaboration, spearheaded by Arthur Medeiros of the USGS, has focused efforts on the reestablishment of the native dryland forest of East Maui in Auwahi and Kama‘ole districts (Medeiros, 2003). Extensive field exploration in the late 1980’s (Medeiros et al., 1986) called attention to the deterioration of the leeward dryland forest on the slopes of Haleakalā, and the Auwahi region was identified as prime area to focus conservation efforts (Erdman et al., 2000). Auwahi is one of the last remaining relatively intact dryland forests in the state of Hawai‘i and is home to greater variety of native trees than nearly any other dryland forest in the state (Medeiros et al., 1986). A land owner (‘Ulupalakua Ranch), resource managers, scientists, and volunteers began an effort to restore a 10 acre section of this dryland forest beginning in 1997. The area was completely fenced to exclude grazing animals, and measures were taken against alien grass and other invasive species, using herbicides and fast growing native species. Botanical members of the original community were protected and added as necessary. Since the initial restoration efforts began the project has expanded and now covers a total of 56 acres at three different sites (Figure 48).

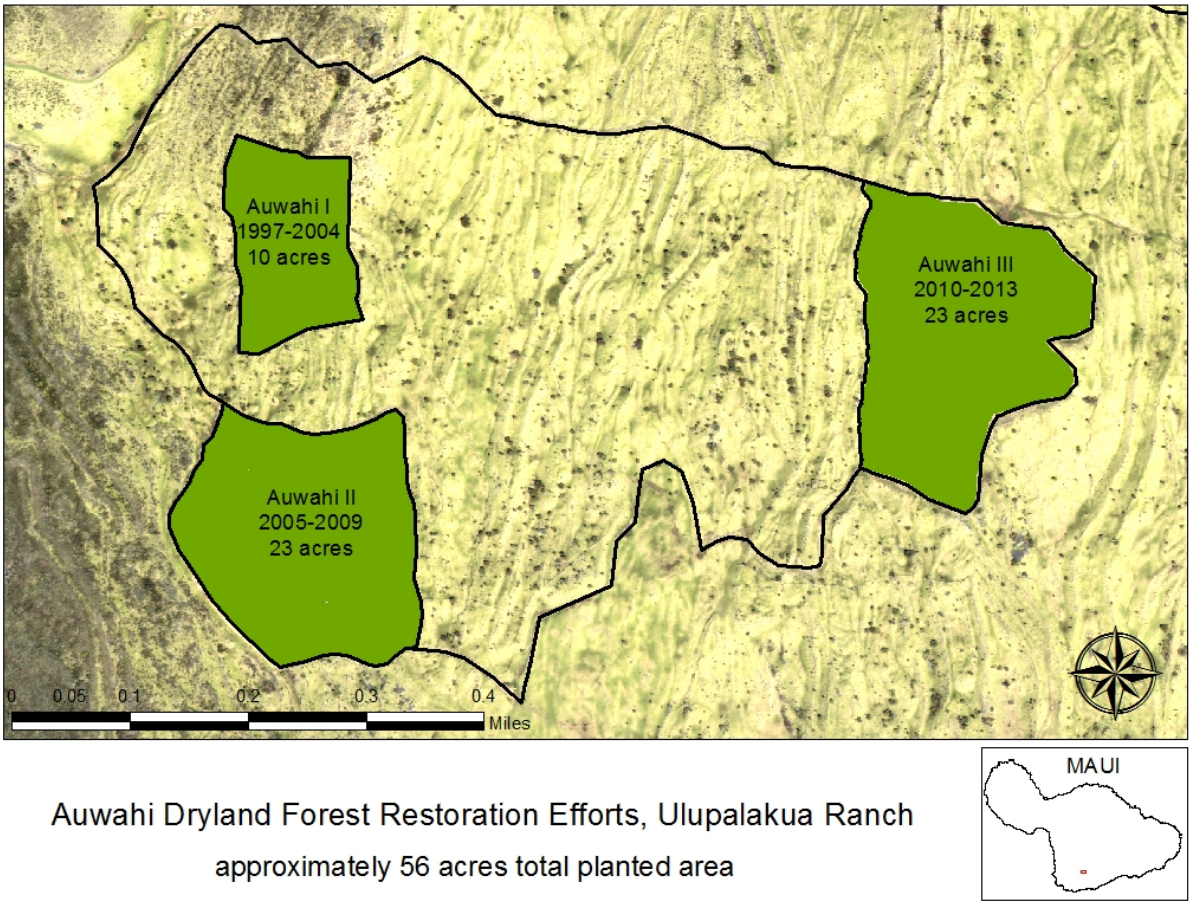

Figure 48: Auwahi dryland forest restoration area.

The benefits of restoring the native dryland forest in Auwahi include reestablishment of understory microhabitats for spontaneous regeneration of native species (Medeiros and von Allmen, 2006), increased cloud water interception (Giambelluca et al., 2011), and increased functioning of soil hydraulic properties (Perkins et al., 2012). In December of 2000 HaleNet station HN-141 (1240 m) was installed at Auwahi in the early stages of the restoration project. The unique placement of this station allows for the investigation of climate characteristics on the south-facing leeward slope of the mountain at the lower limits of the cloud zone. In addition the sustained operation of HN-141 will provide a more comprehensive understating to the effects that reforestation efforts have on microclimates in the area. Auwahi is now considered one of the most successful dryland forest restoration projects in the world (Cabin, 2011) and it serves as a

model for cost-effective approaches to restoring leeward forest systems at the landscape-level across the Hawaiian archipelago (Medeiros and vonAllmen, 2006).

Trends in climate variables observed at HN-141 were not assessed in the main body of this report due to the short (~13 yr) period of record at this station. Linear trends for six available variables are shown in Table 28. It is notable that despite increasing solar radiation and decreasing rainfall, decreases were observed in net radiation (non-significant) and air temperature (significant in both seasons). These changes are consistent with expected effects on the local microclimate of restoring woody vegetation and provide a measure of the physical impacts of this pioneering restoration effort.

Table 28: Period-of-record (2001-2013) trends at HN-141

Varible	Dry-Season					Wet-Season				
K_d	Trend (W m^{-2} yr^{-1})	n	r^2	SE	p	Trend (W m^{-2} yr^{-1})	n	r^2	SE	p
	0.109	13	0.002	0.72	0.883	0.465	12	0.070	0.54	0.408
R_n	Trend (W m^{-2} yr^{-1})					Trend (W m^{-2} yr^{-1})				
	-1.329	11	0.141	1.86	0.255	-1.327	11	0.1644	1.00	0.216
T_a	Trend (˚C yr^{-1})					Trend (˚C yr^{-1})				
	-0.089	13	0.496	0.03	0.007	-0.062	11	0.326	0.03	0.067
WS	Trend (m s^{-1} yr^{-1})					Trend (m s^{-1} yr^{-1})				
	-0.012	11	0.074	0.02	0.419	-0.041	10	0.454	0.02	0.033
ZP	Trend (% yr^{-1})					Trend (% yr^{-1})				
	-0.283	12	0.041	0.43	0.526	0.432	11	0.120	0.26	0.134
P	Trend (mm yr^{-1})					Trend (mm yr^{-1})				
	-1.786	13	0.126	1.42	0.235	-5.877	12	0.3506	2.53	0.043

8.2: Little HaleNet Climate Network

The high-elevation northeastern slopes of Haleakalā Volcano are home to some of the most remote and undisturbed forest ecosystems in Hawai‘i. These ecosystems are dominated with native vegetation, insects and bird species. Early Hawaiians did not use these high-elevation lands extensively (Burney et al., 1995) and current conservation efforts put forth by Haleakalā National Park and the Hawai‘i State Natural Area Reserve (NAR) have focused on reducing the spread of invasive species and protecting rare and endangered species in these areas (Loope et al., 1992). In August of 2005 a network of 12 climate stations was established to extend westward from HaleNet and to integrate with 134 permanent vegetation plots established

from 2003-2006 on the northeast slope of Haleakalā Volcano (Figure 49; Crausbay and Hotchkiss, 2010). The climate stations (referred to as "Little HaleNet") range from ~1980 m to ~ 2315 m in elevation and create three elevational transects from the Northeast Rift to Pu'u Alaea. Each elevational transect consists of one station in the alpine grassland and three stations that bracket the upper cloud forest limit. The climate stations are equipped with instrumentation to measure precipitation (established 2005), soil moisture (established 2007), air temperature (established 2008), relative humidity (established 2008), photosynthetically active radiation (established 2011) and soil temperature (2005-2008). Vegetation plots are arranged along nine elevational transects and represent points within the upper ~300 m of cloud forest and ~ 300 m immediately above the forest line.

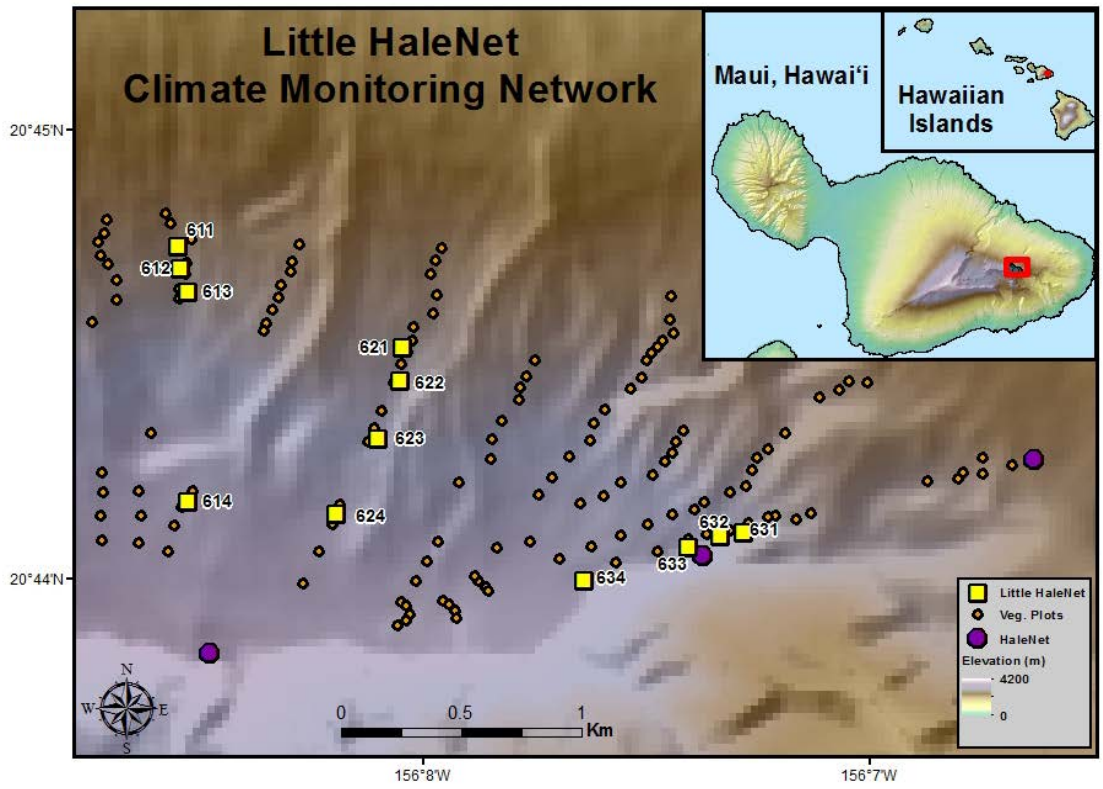

Figure 49: Little HaleNet climate network on the eastern slope of Haleakalā Volcano.

The Little HaleNet climate network has been used to: 1) create climate maps that describe spatial pattern of climate during strong El Niño and La Niña events relative to neutral climate (Crausbay et al., 2014), 2) identify the changes in plant species assemblage and structure due to changes in moisture (Crausbay and Hotchkiss, 2010), and 3) model the strong relationship

between the cloud forest's upper limit and humidity during strong El Niño events and to determine the relationships between cloud forest species assemblage and mean rainfall (Crausbay et al., 2014). The close spatial proximity of the climate stations along their respective transects provides essential information regarding variations in microclimate in relation to the cloud forest boundary. A recent study Gotsch et al. (2014) concluded that the microclimates along these transects affect stomatal conductance and transpiration of the dominant native species (ōhiʻa lehua, *Metrosideros polymorpha*) found there. The data obtained from Little HaleNet was integrated with data obtained from HaleNet station HN-162 (2260 m), which is located within the Little HaleNet domain, and HN-161 (2460 m) and HN-164 (1650 m) which are above and below Little HaleNet, respectively.

8.3. Big Bog (The wettest place in the Hawaiian Islands)

HaleNet station HN-164 (1650 m) is positioned on the windward slopes of northeastern Haleakalā Volcano in the heart of the tropical montane cloud forest. HN-164 is located in an area called "Big Bog" which has recently been identified as the wettest spot in the Hawaiian archipelago as well as one of the wettest spots in the world (Giambelluca et al., 2013). The analysis leading to the update of the Rainfall Atlas of Hawaiʻi in 2012 (http://rainfall.geography.hawaii.edu/) found that Big Bog averaged a whopping 10,271 mm of rainfall per year (Figure 50), slightly higher than the average for Mount Waialeale (10,010 mm) on the island of Kauaʻi, which had long been identified as the wettest spot in the Islands. Prior to the establishment of the HaleNet station there in 1992, rainfall for Big Bog was estimated at around 4,600 mm (180 inches) per year (Giambelluca, 1986). To everyone's surprise, the first full year of recorded data showed 13,995 mm (551 inches) of rainfall, which is one of the highest annual rainfall totals measured anywhere. The extremely wet conditions at Big Bog are explained by the persistent transport of moisture rich air by the northeast trade winds up the steep mountain slopes, where it condenses to form clouds and precipitation. Persistently cloudy conditions at Big Bog are verified by the fact that its average solar radiation, potential evapotranspiration and vapor pressure deficit are the lowest in the network and relative humidity and wet season cloud attenuation are the highest.

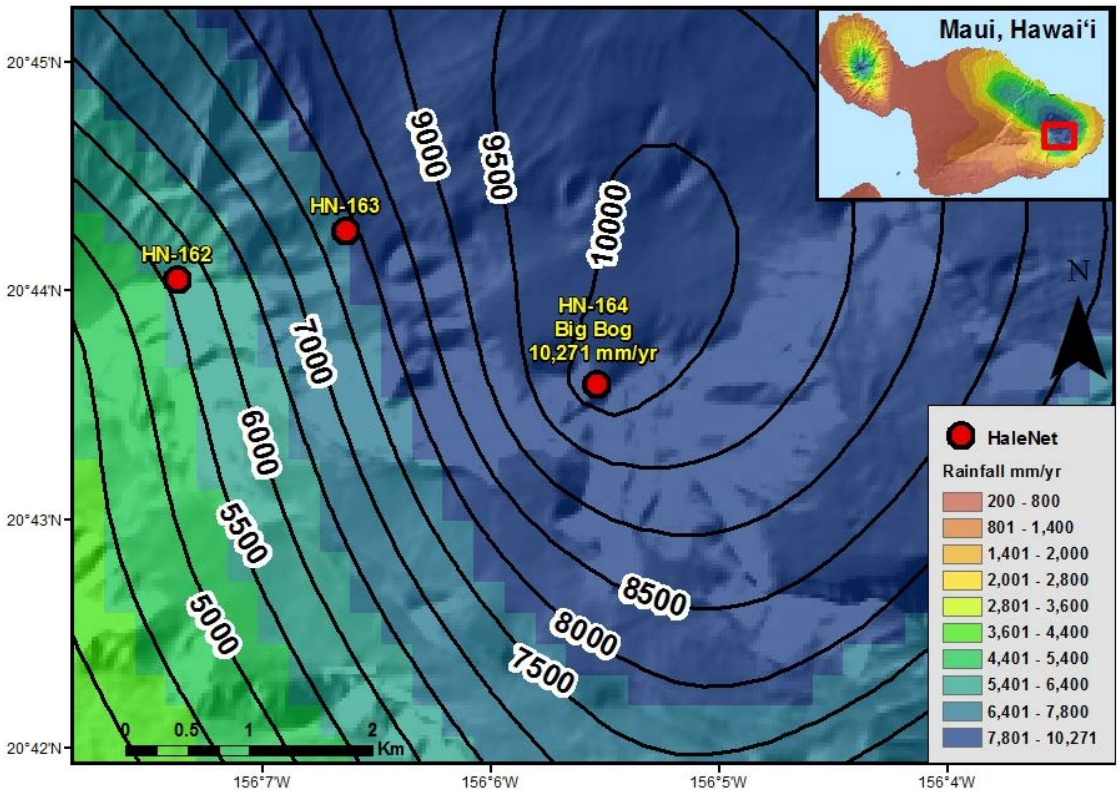

Figure 50: Mean annual rainfall Big Bog, Maui.

8.4. Cloud Water Interception in Hawai‘i

Cloud water interception (CWI) is a significant component of the hydrological cycle (Scholl et al., 2007) and a biologically important source of water (Muller-Dombois 1967) in tropical montane watersheds in Hawai‘i above cloud base altitude. Orographic uplift of moist air on the windward slopes driven by the trade winds and on the leeward slopes driven by thermal slope winds, create persistently cloudy conditions above the lifting condensation level (~ 600 m; DeLay and Giambelluca, 2010) and below the TWI base height (~2100 m, Cao et al., 2007). Several studies have focused on determining the role of intercepted cloud water on the slopes of Haleakalā because climate change and land cover change threaten local water supplies and the survival of endemic species (Scholl et al., 2007; Giambelluca et al., 2010; Delay et al., 2010; Giambelluca et al., 2011). These studies have highlighted the importance of cloud water to the survival of vegetation and the functioning of the hydrological cycle. HaleNet station HN-142 was only in operation for 2 years, however, the data obtained during this time provided valuable

insights into the role of fog at the upper boundary of the cloud zone on the windward side of the mountain. Using an isotopic mixing model approach, Scholl et al., (2007) estimated that cloud water intercepted at HN-142 (2000 m) and at HN-141 (1240 m; Figure 51) accounted for 37 and 46 % of annual rainfall at Waikamoi and Auwahi, respectively. In a related paper, Giambelluca et al. (2011), estimated CWI using the canopy water balance technique at these same sites and found that CWI was responsible for 166 and 1,212 mm (6.5 and 47.7 inches) per year, or 17 and 48% of total rainfall at the leeward and windward sites respectively. A large portion of intercepted cloud water, 74% (HN-141) and 83% (HN-142) was estimated to become throughfall, thus significantly increasing the soil water at both of these sites (Giambelluca et al., 2011). The interception of cloud water contributes to the soil water, ground water and stream flow on the windward slopes and provides life-sustaining moisture to dry and/or high-elevation leeward slopes (Giambelluca et al., 2010).

Figure 51: Fog screen at Auwahi (HN-141 site) used for intercepting cloud water.

8.5 The Haleakalā Silversword

The high-elevation slopes of Haleakalā Volcano are home to some of the most unique endemic plant species found anywhere in the Hawaiian archipelago. One such species, the "Haleakalā silversword" *(Argyroxiphium sandwicense* subsp. *macrocephalum*; Figure 52*)*, can be found on largely barren cinder cones in Haleakalā Crater and sparsely vegetated landscapes close to the summit (Loope et al., 1992). This species is currently confined to the geographic area spanning the central and western portions of Haleakalā to the summit, within the alpine zone ranging from 2150 to 2990 m elevation (Krushelnycky et al., 2013). By the early 1930s the Haleakalā silversword population had severely declined due to grazing by goats and cattle and to vandalism (Loope and Crivellone, 1986). In some areas, such as the Kaupo gap region, silverword populations were completely eliminated by grazing animals (Medeiros et al., 1986). Subsequently, after protection was provided by the national park, silversword numbers increased substantially (Loope and Crivellone, 1986). To exclude ungulates and grazing animals from native ecosystems including silverword habitats Haleakalā National Park installed a fence around the perimeter of much of the park and removed all ungulates inside of the fence. The increase in the silversword population during the latter part of the 20th century has been considered a conservation success story. However, the silversword has declined in recent decades.

Figure 52: Haleakalā silversword (*Argyroxiphium sandwicense macrocephalum).*

In a recent study, Krushelnycky et al., (2013) determined that silversword mortality has increased over the past 20 years. They concluded that the decline since the mid-1990s was associated with changing climatic conditions at high elevations on Haleakalā Volcano. Increases in temperature, solar radiation, and the number of zero rainfall days (Krushelnycky et al., 2013) were identified at the 3 high-elevation leeward HaleNet stations (2120, 2590 and 2990 m), which span the elevation range of silversword habitat. This increase in mortality due to changes in climate is alarming considering that the local climatic trend is toward warmer and drier conditions at high elevations; silversword decline is likely to continue In July of 2010, Dr. Paul Krushelnycky of the University of Hawai‘i installed a network of six weather stations in the crater of the volcano as part of an effort to monitor silversword population trends. This network, which is unofficially referred to as “CraterNet” covers a vertical elevation gradient of 725 m (2185 to 2910 m) and encompasses the major geographic range of the current silversword population (Figure 53). Station locations were chosen based on population density and proximity

to existing or planned silversword research plots. Each station is equipped with instrumentation to measure precipitation, air temperature, relative humidity, soil temperature (5 cm depth), and leaf wetness. In addition, two soil moisture sensors have been installed at each station to monitor moisture conditions in an area of exposed soil and beneath a healthy plant.

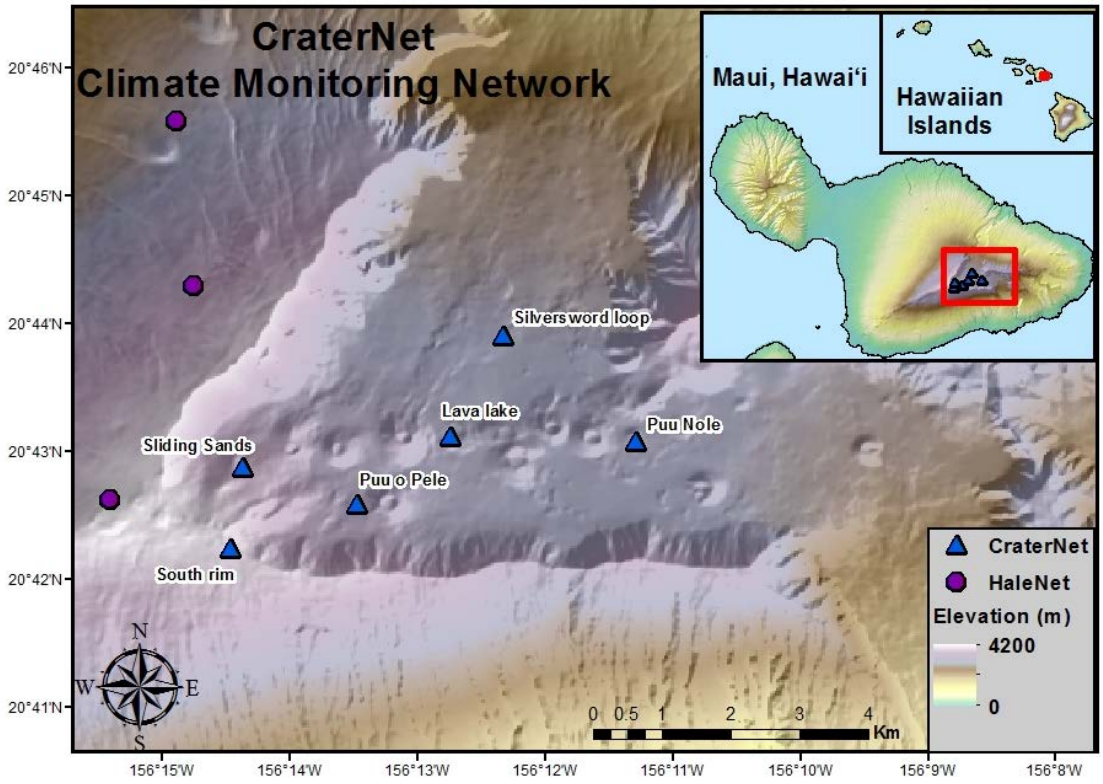

Figure 53: CraterNet climate monitoring network, Maui, Hawai‘i.

8.6. Evapotranspiration in Hawai‘i

Evapotranspiration is one of the most difficult to quantify of the components of the water or energy balance and direct measurements are costly to obtain (Giambelluca and Nullet, 1992b). An understanding of local differences in evapotranspiration is useful in many applications including agricultural planning and water resource assessment and management. For many years, evaporation pans were commonly used by the Hawaiian sugar growers to estimate evapotranspiration in Hawai‘i. Beginning in 1987, evaporation research began at six of the MauiNet sites (Nullet and Giambelluca, 1990). The Ekern evaporimeter, a 6” PVC cap reservoir containing a 6” black carborundum stone evaporating surface, was used to monitor evaporative

demand. To use this manual device, the reservoir is refilled every morning and the volume used is recorded. The previous day's evaporation rate is then obtained by dividing the measured volume by the surface area of the instrument (Nullet, 1989).

In the summer of 1988, a second series of evaporation measurements began at the first three HaleNet sites (HN-106, HN-119 and HN-151). For this experiment an automated version of the Ekern evaporimeter was introduced to record evaporation continuously. In the automated version, water flow to the carborundum stone evaporating surface is measured (Giambelluca et al., 1992a). The objectives of this analysis were to quantify the differences in average rates and diurnal patterns of evaporative demand along an elevation transect through the mean TWI, and to examine the influences on evaporation at high elevations by comparing measured values with potential evapotranspiration model estimates (Giambelluca and Nullet, 1992a). In a follow up analysis (Giambelluca and Nullet, 1992b) expanded the experimental gradient by incorporating evaporimeter measurements from HN-152 (2590 m) and HN-153 (2990 m). This analysis presents results of several years of measurements using the new instrument.

Using the evaporimeter results, Giambelluca and Nullet (1992b) were able to characterize the evaporation climate along the Haleakalā slope (Figure 54). At the lowest elevations evaporation is controlled by diurnal and seasonal variations in solar radiation. Within the cloud zone mid-day evaporation is frequently reduced by high humidity and low radiation causing the lowest evaporation rates. In the inversion level or "transitional zone", evaporation rates are highly variable as a result of shifts in the inversion height. Above the inversion zone in the arid "free atmosphere", evaporation is the highest due to extremely dry conditions.

Figure 54**:** Evaporimeter at HN-152.

Literature Cited

Adler, R.F., G.J. Huffman, A. Chang, R. Ferraro, P. Xie, J. Janowiak, B. Rudolf, U. Schneider, S. Curtis, D. Bolvin, A. Gruber, J. Susskind, and P. Arkin, 2003: The Version 2 Global Precipitation Climatology Project (GPCP) monthly precipitation analysis (1979-Present). *J. Hydrometeor*., **4**, 1147-1167.

Allen, R.G., L.S. Pereira, D. Raes, and M. Smith, 1998: *Crop Evapotranspiration*(guidelines for computing crop water requirements). FAO Irrigation and Drainage Paper No. 56. FAO, Rome.

Barnes M.L., 2013: *An Assessment of Diurnal and Seasonal Cloud Cover Changes over the Hawaiian Islands using Terra and Aqua Modis*. MS thesis, Department of Natural Resources Management, University of Hawai‘i at Mānoa, Honolulu.

Bonan, G., 2008: *Ecological Climatology* (2nd ed.). Cambridge University Press. Cambridge, U.K. 563 pp.

Burney, D., R.V. DeCandido, L.P. Burney, F.N. Kostel-Hughes, T.W. Stafford Jr. and H.F. James, 1995: A Holocene record of climate change, fire ecology and human activity from montane Flat Top Bog, Maui. *J. Paleolimnol.*, **13**, 209–217.

Cabin, R.J., 2011: *Intelligent Tinkering: Bridging the Gap between Science and Practice*. Island Press. Washington, D.C. 240 pp.

Cao, G.G., T.W. Giambelluca, D.E. Stevens, and T.A. Schroeder, 2007: Inversion variability in the Hawaiian trade wind regime. *J. Climate,* **20**, 1145–1160.

Crausbay, S.D. and S.C. Hotchkiss, 2010: Strong relationships between vegetation and two perpendicular climate gradients high on a tropical mountain in Hawai‘i. *J. Biogeogr.*, **37**, 1160-1174.

Crausbay, S.D., and S.C. Hotchkiss, 2012: Pollen-vegetation relationships at a tropical cloud forest’s upper limit and accuracy of vegetation inference. *Rev. Palaeobot. Palynol.*, **184**, 1-13.

Crausbay, S.D., A.G. Frazier, T.W. Giambelluca, R.J. Longman, and S.D. Hotchkiss, 2014: The addition of climate during a strong El Niño event improves distribution models of tropical montane cloud forest characteristics in Hawai‘i. *Oecologia,* **175**(1), 273-284.

DeLay, J.K., and T.W. Giambelluca, 2010: History of cloud water interception research in Hawai'i. In: *Tropical Montane Cloud Forests: Science for Conservation and Management*,L.A. Bruijnzeel, F.N. Scatena, L.S. Hamilton (eds.), 332-341. Cambridge University Press. Cambridge, U.K.

Diaz, H.F., T.W. Giambelluca, and J.K. Eischeid, 2011: Changes in the vertical profiles of mean temperature and humidity in the Hawaiian Islands. *Global Planet. Change*, **77**, 21–25.

Diaz, H.F, and T.W. Giambelluca, 2012: Changes in atmospheric circulation patterns associated with high and low rainfall regimes in the Hawaiian Islands region on multiple time scales. *Global Planet. Change*, **98-99**, 97-108.

Dunne, T., and Leopold L.B., 1978: *Water in Environmental Planning.* W.H. Freeman and Company. New York. 814 pp.

Durbin J., and G.S. Watson, 1971: Testing for serial correlation in linear regression III. *Biometrika*, **58**, 1–19.

Dutton, E.G., D.W. Nelson, R.S. Stone, D. Longnecker, G. Carbaugh, J.M. Harris, and J. Wendell, 2006: Decadal variations in surface solar irradiance as observed in a globally remote network. *J. Geophys. Res.*, **111**, D19101.

Ekern, P.C., 1983: *Measured Evaporation in High Rainfall Areas, Leeward Koolau Range, O‘ahu, Hawai‘i*. U. Hawai‘i Water Resour. Res. Center Tech. Rept. 156, Honolulu Hawai‘i. 60 pp.

England, M.H., S. McGregor, P. Spence, G.A. Meehl,, A. Timmermann, W. Cai, A.S. Gupta, M.J. McPhaden, A. Purich, and A. Santoso, 2014: Recent intensification of wind-driven circulation in the Pacific and the ongoing warming hiatus. *Nature Clim. Change*, **4**, 222-227.

Erdman, S., A. Medeiros, A. Durso, and L.L. Loope, 2000: Ranchers and biologists in Hawai'i: keeping a business strong and protecting native forests at Ulupalakua Ranch, Maui. *Rangelands*, **22**, 33-35.

Frazier, A.G., T.W. Giambelluca, and H.F. Diaz, 2013: Mapping rainfall trends in Hawai‘i, Abstract H43I-1580 presented at 2013 Fall Meeting, AGU, San Francisco, Calif., 9-13 Dec.

Garza, J.A., P.S. Chu, C.W. Norton, and T.A. Schroeder, 2012: Changes of the prevailing trade winds over the islands of Hawaii and the North Pacific. *J. Geophys. Res,*. **117** (D11).

Giambelluca, T.W., M.A. Nullet, and T.A. Schroeder, 1986: *Rainfall Atlas of Hawai'i*. Department of Land and Natural Resources, Honolulu. 267 pp.

Giambelluca, T.W., and D. Nullet, 1991: Influence of the trade-wind inversion on the climate of a leeward mountain slope in Hawai‘i. *Clim. Res.*, **1**, 207-216

Giambelluca, T.W., and D. Nullet, 1992a: Evaporation at high elevations in Hawai‘i. *J Hydrol.*, **136**, 219-235.

Giambelluca, T.W., and D. Nullet, 1992b: An automated recording atmometer: 2. Evaporation measurement on a high elevation transect in Hawai‘i. *Agric. For. Meteorol.*, ***62***,127-138.

Giambelluca, T.W., D.L. McKenna, and P.C. Ekern, 1992: An automated recording atmometer: 1. Calibration and testing *Agric*. *For. Meteorol*., **62**, 109-125.

Giambelluca, T.W., and T.A. Schroeder, 1998: The physical environment: climate, In: S.P. Juvik, J.O Juvik (eds.), *Atlas of Hawai‘i,* 3rd edition, 49–59. University of Hawai'i Press, Honolulu.

Giambelluca, T.W., H.F. Diaz, and M.S.A. Luke, 2008: Secular temperature changes in Hawai‘i . *Geophys. Res. Lett.*, **35**, L12702.

Giambelluca T.W., J. K. DeLay, M.A. Nullet, M.A. Scholl, and S.B. Gingerich, 2010: Interpreting canopy water balance and fog screen observations: separating cloud water from wind-blown rainfall at two contrasting forest sites in Hawai‘i. In: *Tropical Montane Cloud Forests: Science for Conservation and Management*, L.A. Bruijnzeel,F.N. Scatena, L.S. Hamilton (eds.), 342–351. Cambridge University Press. Cambridge, UK..

Giambelluca, T.W., J.K. DeLay, M.A. Nullet, M.A. Scholl, and S.B. Gingerich, 2011: Canopy water balance of windward and leeward Hawaiian cloud forests on Haleakalā, Maui, Hawai'i. *Hydrol Processes*, **25**, 438-447.

Giambelluca, T.W., Q. Chen, A.G. Frazier, J.P. Price, Y.-L. Chen, P.S. Chu, J.K. Eischeid, and D.M. Delparte, 2013: Online rainfall atlas of Hawai‘i. *Bull. Amer. Meteor. Soc.* **94**, 313-316.

Giambelluca, T.W., X. Shuai, M.L. Barnes, R.J. Alliss, R.J. Longman, T. Miura, Q. Chen, A.G. Frazier, R.G. Mudd, L. Cuo, and A.D. Businger, 2014: *Evapotranspiration of Hawai‘i.* Final report submitted to the U.S. Army Corps of Engineers—Honolulu District, and the Commission on Water Resource Management, State of Hawai‘i.

Gong, L., C.L. Xu, D. Chen, S. Halldin, and Y.D. Chen, 2006: Sensitivity of the Penman–Monteith reference evapotranspiration to key climatic variables in the Changjiang (Yangtze River) basin. *J. Hydrol.*, **329**, 620-629.

Gotsch S.G., S.D. Crausbay, A.Weintrab, T.W. Giambelluca, R.J. Longman, H. Asbjornesen, S.C. Hotchkiss and T. Dawson, 2014: Water relations and microclimate around the upper limit of cloud forest in Maui, Hawai‘i. *Tree Physiol.* **34**, 766-777.

Gueymard, C.A., 2008: REST2: High-performance solar radiation model for cloudless-sky irradiance, illuminance, and photosynthetically active radiation–Validation with a benchmark dataset. *Sol. Energy,* **82**, 272-285.

Gueymard C.A., 2012: Clear-sky irradiance predictions for solar resource mapping and large-scale applications: Improved validation methodology and detailed performance analysis of 18 broadband radiative models. *Sol. Energy*, **86,** 2145–2169.

Howell, T.A., and S.R. Evett, 2004: *The Penman-Monteith Method*. USDA Agricultural Research Service. Bushland, Texas. 12 pp.

Krushelnycky, P.D., L.L. Loope, T.W. Giambelluca, F. Starr, K. Starr, D. Drake, A.D. Taylor and R.H. Robichaux, 2013: Climate-associated population declines reverse recovery and threaten future of an iconic high-elevation plant. *Glob. Change Biol.* **19**, 911-922.

Liley, J.B., 2009: New Zealand dimming and brightening. *J. Geophys. Res*., **114,** D00D10.

Lauer, A., C. Zhang, O. Elison Timm, Y Wang, and K. Hamilton, 2013: Downscaling of climate change in the Hawai‘i region using CMIP5 results: On the choice of the forcing fields. *J. Clim.*, **26** 10006-10030.

Leopold, L.B., 1949: The interaction of trade wind and sea breeze, Hawaii. *J.Meteorol.*, **6**, 312-320.

Longman R.J.2011: *Homogenization of long-term solar radiation time series using a clear-sky radiation model and assessment of solar radiation variability at upper elevations on Maui, Hawaii*. Unpublished Master’s thesis, Geography Department, University of Hawai‘i at Mānoa, Honolulu.

Longman, R.J, T.W., Giambelluca, and O. Elison Timm, 2012: The spatial dynamics of potential evapotranspiration in Hawai‘i: How driving variables are influenced by the trade wind inversion. American Geophysical Union Fall Meeting, San Francisco, December 2012.

Longman, R.J., T.W. Giambelluca, and A.G. Frazier, 2012: Modeling clear-sky solar radiation across a range of elevations in Hawai‘i: Comparing the use of input parameters at different temporal resolutions. *J. Geophys. Res.*, **117**, D02201.

Longman R.J., T.W. Giambelluca and M.A. Nullet 2013: Use of a clear-day solar radiation model to homogenize solar radiation measurements in Hawai‘i., *Sol. Energy* **91**, 102-110.

Longman, R.J., T.W., Giambelluca, R.J. Allis, and M. Barnes, 2014: Temporal solar radiation change at high elevations in Hawai‘i. *J. Geophys. Res*,.**119,** 6022-6033.

Longman R.J, H.F. Diaz and T.W. Giambelluca (In review) Sustained increases in lower tropospheric subsidence over the central tropical North Pacific drives a decline in high elevation rainfall in Hawai‘i. Submitted to the *J. Clim.*, December 2014.

Longman, R.J., 2015: *The Effects of Trade Wind Inversion Variability on High Elevation Climates in Hawai‘i.* Ph.D. Dissertation, Geography Department, University of Hawai‘i at Mānoa, Honolulu.

Loope, L.L., A.C. Medeiros, and BH. Gagné, 1991: *Aspects of the History and Biology of the Montane Bogs.* Cooperative National Park Resources Studies Unit, Department of Botany, University of Hawai'i at Mānoa, Honolulu. *CPSU* Tech. Rept. **76**.

Loope, L.L., R.J. Nagata, and A.C. Medeiros, 1992: Alien plants in Haleakalā National Park. In: C.P.Stone, C.W. Smith, J.T. Tunison (eds.), *Alien Plant Invasions in Native Ecosystems of Hawaii: Management and Research*, 551-576. University of Hawaii Press for Cooperative National Park Resources Studies Unit, University of Hawai'i at Mānoa, Honolulu.

Loope, L.L., and T.W. Giambelluca,1998: Vulnerability of island tropical montane cloud forests to climate change, with special reference to East Maui, Hawai‘i. *Climate Change,* **39**, 503-517.

Loope L.L., and C.F. Crivellone, 1986: *Status of the Haleakalā Silversword: Past and Present.* Cooperative National Park Resources Studies Unit, Department of Botany, University of Hawai'i at Mānoa, Honolulu. CPSU Tech. Rept. 58.

Lowe, P.R., 1977: An approximate polynomial for the computation of saturation vapor pressure. *J. Appl. Meteorol.*, **16**, 100-102.

Lu, J., G. Sun, S.G. McNulty, and D.M. Amatya, 2005: A comparison of six potential evapotranspiration methods for regional use in the southeastern United States. *J. Am. Water Resour. Assoc.*, **41**, 621-633.

Medeiros A.C., L.L. Loope, and R.A. Holt, 1986: *Status of Native Flowering Plant Species on the South Slope of Haleakalā, East Maui, Hawai'i*. Cooperative National Park Resources Studies Unit, Department of Botany, University of Hawai'i at Mānoa, Honolulu. CPSU Tech. Rept. **59.**

Medeiros, A.C., C.F. Davenport, and C.G. Chimera, 1998: *Auwahi: Ethnobotany of a Hawaiian Dryland Forest*. Cooperative National Park Resources Studies Unit, Department of Botany, University of Hawai'i at Mānoa, Honolulu. *CPSU Technical Report* **117.**

Medeiros, A.C., 2003: The Pū 'Olē 'Olē blows and 'Awa is poured: Maui Kumu Keli'i Tau'a welcomes Hawaiian seedlings back to Auwahi. *Native Plants Journal*, **4**, 48-51.

Medeiros, A.C., and E. von Allmen, 2006: *Restoration of Native Hawaiian Dryland Forest at Auwahi, Maui*. USGS Fact Sheet, 2006-3035.

Minyard, W.P., T.W. Giambelluca, and D. Nullet, 1994: Elevational Patterns of Climate on the Leeward Slope of East Maui, Hawaii. Cooperative National Park Resources Studies Unit, Department of Botany, University of Hawai'i at Mānoa, Honolulu. CPSU Tech. Rept. **92.**

Monteith, J. 1965: Evaporation and environment. (Part of symposium on The State and Movement of Water in Living Organisms). *Soc. Exp. Biol.* **19,** 205-234.

Mueller-Dombois, D, 1967: Ecological relations in the alpine and subalpine vegetation on Mauna Loa, Hawai'i. *Journal of the Indian Botanical Society* **46**, 403-411.

Murray, F.W., 1967: On the computation of saturation vapor pressure. *J. Appl. Meteorol.*, **6**, 203-204.

National Park Service (NPS), 2015: *Haleakalā National Park, Island of Maui, Hawai'i*. National Park Service U.S. Department of Interior Foundation Document Part 1.

Nullet, D., 1989: *Climate Controls on Evaporation in Hawai'i*. Ph.D. Dissertation, Department of Geography, University of Hawai'i at Mānoa, Honolulu.

Nullet, D., and T.W. Giambelluca, 1990: Winter evaporation on a mountain slope, Hawaii. *J. Hydrol.*, **112**, 257-265.

Parmesan, C., 1996: Climate and species' range. *Nature*, **382**, 765-766. Penman, H., 1948: Natural evaporation from open water, bare soil, and grass. *Proc. Royal Soc.* **193**, 120-146.

Perkins, K.S., J.R. Nimmo, and A.C. Medeiros, 2012: Effects of native forest restoration on soil hydraulic properties, Auwahi, Maui, Hawaiian Islands. *Geophys. Res. Lett.* **39**, L05405.

Priestley, C., and R. Taylor, 1972: On the assessment of surface heat flux and evaporation using large-scale parameters. *Mon. Weather Rev.* **100**, 81-92.

Riehl, H., 1979: *Climate and Weather in the Tropics*. Academic Press, London. 611 pp.

Riehl, H., T.C. Yeh, J.J. Malkus, and N.E. La Seur, 1951: The northeast trade of the Pacific Ocean. *Quart. J. Royal Meteor. Soc***. 77**, 598-626.

Sanderson, M. 1993: *Prevailing Trade Winds: Climate and Weather in Hawaii*. University of Hawaii Press. Honolulu.127 pp.

Scholl M.A, T.W. Giambelluca, S.B. Gingerich, M.A. Nullet, and L.L. Loope, 2007: Cloud water in windward and leeward mountain forests: The stable isotope signature of orographic cloud water. *Water Resources Research* **43**, WI2411.

Schroeder, T.A., 1993: Climate controls (Chapter 3). In: *Prevailing Trade Winds: Climate and Weather in Hawaii*, M. Sanderson, ed., 12-36. University of Hawaii Press, Honolulu.

Sherrod, D.R., J.M. Sinton, S.E. Watkins, and K.M. Brunt, 2007: *Geologic Map of the State of Hawai`i*. U.S. Geological Survey Open-File Report 2007-1089, 83 pp.

Thomas, B.R., E.C. Kent, and V.R. Swail, 2005: Methods to homogenize wind speeds from ships and buoys. *Int. J. Climatol.*, **25**, 979-995.

Thornthwaite, C. 1948: An approach toward a rational classification of climate. *Geogr. Rev.*, **38**, 55-94.

Timm, O.E., H.F., Diaz, T.W. Giambelluca, and M. Takahashi, 2011: Projection of changes in the frequency of heavy rain events over Hawai'i based on leading Pacific climate modes. *J. Geophys. Res.* **116**, D04109.

Tu, C.C., and Y.L. Chen, 2011: Favorable conditions for the development of a heavy rainfall event over Oahu during the 2006 wet period. *Weather Forecast.*, **26**, 280-300.

Vecchi, G.A., and A.T. Wittenberg, 2010: El Niño and our future climate: where do we stand?. *WIREs Climate Change*, **1**, 260-270.

Vörösmarty, C.J., C.A. Federer, and A.L. Schloss, 1998: Potential evaporation functions compared on US watersheds: Possible implications for global-scale water balance and terrestrial ecosystem modeling. *J. Hydrol.*, **207**, 147-169.

Appendix

A.1 HaleNet Contributors

USGS: Gordon Tribble, Steve Gingerich, Art Medeiros

Field Technicians: Kathy Wakelee, Sabine Jessel, Bill Minyard, Chuck Chimera, Philip Thomas, Paul Krushelnycky, Stephanie Joe, Forest Starr, Kim Starr, David Penn, Dennis Nullet, John DeLay, Ryan Longman, Ryan Mudd

Haleakalā National Park:

Resource Management: Ron Nagata, Ted Rodrigues, Steve Anderson, Matt Brown, Terry Lind, Timmy Bailey, Clinton Fukushima, Ross Hart, Sean Birney

Cultural Resources: Liz Gordon

Maintenance: Mark Rentz, Peter Kafka

Superintendents: Don Reeser, Sarah Creachbaum, Natalie Gates

Windward Aviation: Don Shearer, Duke Baldwin, Peter Vorhees

Collaborating Scientists: Sara Hotchkiss, Shelley Crausbay, Martha Scholl

Haleakalā Ranch: Scott Meidell

Ulupalakua Ranch: Sumner Erdman

UH Kula Ag Exp Station: Dave Oka

Financial Support: National Park Service, UH URC Seed Money, USGS-PIERC, Haleakalā National Park, USGS Global Change Research Program, PICCC, EPSCoR-Hawai‘i

A.2 HaleNet related publications

A.2.1 Journal Articles

Berlin, K.E., T.K. Pratt, J.C. Simon, J.R. Kowalsky, and J.S. Hatfield, 2000: Plant phenology in a cloud forest on the island of Maui, Hawaii. ***Biotropica***, ***32***(1), 90-99.

Buczkowski, G., and P. Krushelnycky, 2012: The odorous house ant, *Tapinoma sessile* (Hymenoptera: Formicidae), as a new temperate-origin invader. ***Myrmecological News***, ***16***, 61-66.

Crausbay, S.D., A.G. Frazier, T.W. Giambelluca, R.J. Longman, and S.D. Hotchkiss, 2014: The addition of climate during a strong El Niño event improves distribution models of tropical montane cloud forest characteristics in Hawai‘i. ***Oecologia 175***(1), 273-284.

Diaz, H.F., T.W. Giambelluca, J.K. Eischeid, 2011: Changes in the vertical profiles of mean temperature and humidity in the Hawaiian Islands. ***Global and Planetary Change, 77***, 21–25.

Giambelluca, T.W. and D. Nullet, 1991: Influence of the trade-wind inversion on the climate of a leeward mountain slope in Hawai‘i, ***Climate Research***., ***1***, 207-216.

Giambelluca, T.W. and D. Nullet, 1992a: Evaporation at high elevations in Hawaii. ***Journal of Hydrology***, ***136***(1), 219-235.

Giambelluca, T.W., and D. Nullet, 1992b: An automated recording atmometer: 2. Evaporation measurement on a high elevation transect in Hawai‘i. ***Agriculture Forest Meteorology***, ***62***: 127-138.

Giambelluca, T.W., H.F. Diaz, M.S.A. Luke, 2008: Secular temperature changes in Hawai‘i . ***Geophysical Research Letters***, ***35***, L12702.

Giambelluca, T.W., J.K. DeLay, M.A. Nullet, M.A. Scholl, and S.B. Gingerich, 2011: Canopy water balance of windward and leeward Hawaiian cloud forests on Haleakalā, Maui, Hawai'i. ***Hydrological Processes***, ***25***(3), 438-447.

Giambelluca, T.W., Q. Chen, A.G. Frazier, J.P. Price, Y.-L. Chen, P.-S. Chu, J.K. Eischeid, and D.M. Delparte, 2013: Online rainfall atlas of Hawai‘i. ***Bulletin American Meteorological. Society,*** **94**, 313-316.

Goldstein, G., P. Melcher, J. Heraux, D.R. Drake,, and T.W. Giambelluca, 1996): Photosynthetic gas exchange and temperature-induced damage in seedlings of the tropical alpine species *Argyroxiphium sandwicense*. ***Oecologia,106***(3), 298-307.

Gotsch S.G., S.D. Crausbay, A. Weintrab, T.W. Giambelluca, R.J. Longman, H. Asbjornesen, S. C. Hotchkiss and T. Dawson, 2014: Water relations and microclimate around the upper limit of cloud forest in Maui, Hawai‘i. ***Tree Physiology, 34*** (7), 766-777.

Hartley, S., P.D. Krushelnycky, and P.J. Lester, 2010: Integrating physiology, population dynamics and climate to make multi-scale predictions for the spread of an invasive insect: the Argentine ant at Haleakalā National Park, Hawai‘i. ***Ecography***, ***33***(1), 83-94.

Krushelnycky, P.D., L.L. Loope, and S.M. Joe, (2004). Limiting spread of a unicolonial invasive insect and characterization of seasonal patterns of range expansion. ***Biological Invasions***, ***6***(1), 47-57.

Krushelnycky, P.D., S.M. Joe, A.C. Medeiros, C.C. Daehler, and L.L. Loope, 2005: The role of abiotic conditions in shaping the long-term patterns of a high-elevation Argentine ant invasion. ***Diversity and Distributions***, ***11***(4), 319-331.

Krushelnycky, P.D., L.L. Loope, T.W. Giambelluca, F. Starr, K. Starr, D. Drake, A.D. Taylor and R.H. Robichaux, 2013: Climate-associated population declines reverse recovery and threaten future of an iconic high-elevation plant. ***Global Change Biology, 19***(3), 911-922.

Loope, L.L., and T.W. Giambelluca, 1998: Vulnerability of island tropical montane cloud forests to climate change, with special reference to East Maui, Hawai‘i. ***Climate Change, 39,*** 503-517.

Longman, R.J., T.W. Giambelluca, and A.G. Frazier, 2012. Modeling clear-sky solar radiation across a range of elevations in Hawai‘i: Comparing the use of input parameters at different temporal resolutions. ***Journal of Geophysical Research,117***, (D2) D02201.

Longman R.J., T.W. Giambelluca, and M.A. Nullet, 2013: Use of a clear-day solar radiation model to homogenize solar radiation measurements in Hawai‘i. ***Solar Energy, 91***,102-110.

Longman, R.J., T.W. Giambelluca, R.J. Allis, and M. Barnes, 2014: Temporal solar radiation change at high elevations in Hawai‘i. ***Journal of Geophysical Research, 119,*** (10) 6022-6033.

Scholl, M.A, T.W. Giambelluca, S.B. Gingerich, M.A. Nullet, and L.L. Loope, 2007): Cloud water in windward and leeward mountain forests: The stable isotope signature of orographic cloud water. ***Water Resources Research, 43***, WI2411.

Sherrod, D.R., J.T. Hagstrum, J.P. McGeehin, D.E. Champion, and F.A. Trusdell. 2006: Distribution, 14C chronology, and paleomagnetism of latest Pleistocene and Holocene lava flows at Haleakalā volcano, Island of Maui, Hawai ‘i: A revision of lava flow hazard zones. ***Journal of Geophysical Research: 111***(B5).

A.2.2 Book Chapters

DeLay, J.K., and T.W. Giambelluca, 2010: History of cloud water interception research in Hawai'i. In: *Tropical Montane Cloud Forests: Science for Conservation and Management*, L.A. Bruijnzeel, F.N. Scatena, L.S. Hamilton (eds.), 332-341. Cambridge University Press. Cambridge, UK.

Giambelluca, T.W., J.K. DeLay, M.A. Nullet M.A. Scholl, S.B Gingerich, 2010: Interpreting canopy water balance and fog screen observations: separating cloud water from wind-blown rainfall at two contrasting forest sites in Hawai‘i. In: *Tropical Montane Cloud Forests: Science for Conservation and Management*, L.A. Bruijnzeel, F.N. Scatena, L.S. Hamilton (eds.), 342-351. Cambridge University Press. Cambridge, UK.

A.2.3 Technical Reports

Giambelluca, T.W., X. Shuai, M.L. Barnes, R.J. Alliss, R.J. Longman, T. Miura, Q. Chen, A.G. Frazier, R.G. Mudd, L. Cuo, and A.D. Businger, 2014: *Evapotranspiration of Hawai‘i*. Final report submitted to the U.S. Army Corps of Engineers—Honolulu District, and the Commission on Water Resource Management, State of Hawai‘i.

Keener, V.W., J.J. Mara, M.L. Finucane, D. Spooner, and M.H. Smith, 2012: Climate change and Pacific Islands: indicators and impacts. Report for the 2012 Pacific Island Regional Climate Assessment. Washington, DC: Island Press.

Krushelnycky, P.D., L.L. Loope, and R.G. Gillespie, 2007. Inventory of arthropods of the west slope shrubland and alpine ecosystems of Haleakalā National Park. Pacific Cooperative Studies Unit, University of Hawai‘i at Mānoa, PCSU Tech Rep. #148,.

Loope L.L., and C.F. Crivellone, 1986: Status of the Haleakalā silversword: past and present. Cooperative National Park Resources Studies Unit, Department of Botany, University of Hawai'i at Mānoa, Honolulu. *CPSU* Tech. Rept. 58.

Thompson, L.G., 2011: Climate records from ice cores drilled in Papua, New Guinea. *MOUNTAIN VIEWS*, 3. The Newsletter of the Consortium for Integrated Climate Research in Western Mountains Vol 5 no.2.

A.2.4 Articles in Review

Longman R.J, H.F. Diaz and T.W. Giambelluca (In review). Sustained Increases in lower tropospheric subsidence over the central tropical North Pacific drives a decline in high elevation rainfall in Hawai‘i. Submitted to the *Journal of Climate*, December 2014.

A.2.5 Doctoral Dissertations

Nullet, D., 1989: *Climate Controls onEvaporation in Hawai‘i.* Ph.D. Dissertation, Department of Geography, University of Hawai‘i at Mānoa, Honolulu.

Longman, R.J., 2015:. *The Effects of Trade Wind Inversion Variability on High Elevation Climates in Hawai‘i*. Ph.D. Dissertation, Department of Geography, University of Hawai‘i at Mānoa, Honolulu.

A.2.6 Master’s Theses

Frazier, A.G., 2012: *Month-year Rainfall Maps of the Hawaiian Islands*. M.A. thesis. Department of Geography, University of Hawai‘i at Mānoa, Honolulu.

Longman R.J., 2011: *Homogenization of Long-term Solar Radiation Time Series Using a Clear-sky Radiation Model and Assessment of Solar Radiation Variability at Upper Elevations on Maui, Hawaii.* M.A. thesis. Department of Geography, University of Hawai‘i at Mānoa, Honolulu.

Menard, T.P., 1999: *Ecological and Hydrological Effects of a Rainless Period on a Montane Cloud Forest Treeline on Haleakalā Maui.* M.A. thesis, Department of Geography, University of Hawai‘i at Mānoa, Honolulu.

Minyard, W. P. (1994). *Relationship of Vegetation Distribution to Water Availability above the Trade Wind Inversion on the West Slope of East Maui, Hawai‘i.* M.A. thesis, Department of Geography, University of Hawai‘i at Mānoa, Honolulu.

Schlappa, K., 2006: *Measurements of Cloud Water and Dry Deposition at Kilauea, Hawai‘i.* M.A. thesis, Department of Oceanography, University of Hawai‘i at Mānoa, Honolulu.

Tran, L.T., 1995: *Relationship between the Inversion and Rainfall on the Island of Maui*. M.A. thesis. Department of Geography, University of Hawai‘i at Mānoa, Honolulu.

Tamayose, J., 2006: *Supplemental Feeding Influences Reproductive Success of the Hawaiian Goose (Branta sandvicensis) at Haleakalā National Park, Maui, Hawai'i*. M.A. thesis. Department of Botany, University of Hawai‘i at Mānoa, Honolulu.

A.2.7 Poster Presentations

Frazier, A.G., H.F. Diaz, and T.W. Giambelluca, 2011: Rainfall in Hawai'i: spatial and temporal changes since 1920. Abstract GC21B-0900 presented at the American Geophysical Union Fall Meeting, San Francisco, December 2011. Presented by Abby Frazier.

Frazier, A.G., T.W. Giambelluca, H.F. Diaz, 2012: Spatial rainfall patterns of ENSO and PDO in Hawai‘i. American Geophysical Union Fall Meeting, San Francisco, December 2012. Presented by Abby Frazier.

Longman, R.J., T.W. Giambelluca, and M.A. Nullet, 2010: HaleNet climate network. A briefing by the Pacific Islands Climate Change Cooperative (PICCC) and the Pacific Climate InformationSystem (PaCIS) about effective interagency communication, coordination, and collaboration on climate change in the Pacific Islands region. Honolulu, December 2010. Presented by Ryan Longman.

Longman, R.J, T.W. Giambelluca, and M.A. Nullet, 2010: Assessment of spatial and temporal microclimatic variability using the HaleNet climate network on Haleakalā Volcano, Maui, Hawai‘i. American Geophysical Union Fall Meeting, San Francisco, December 2010. Presented by Ryan Longman.

Longman, R.J., T.W. Giambelluca, and M.A. Nullet, 2011: Recent trends in solar radiation at high elevations in Hawai‘i. American Geophysical Union Fall Meeting, San Francisco, December 2011. Presented by Ryan Longman.

Longman, R.J., T.W. Giambelluca, and O. Elison Timm, 2012: The spatial dynamics of potential evapotranspiration in Hawai‘i: How driving variables are influenced by the trade wind inversion. American Geophysical Union Fall Meeting, San Francisco, December 2012. Presented by Ryan Longman.

Longman, R.J., T.W. Giambelluca, X. Shuai, M. Barnes, R.J. Alliss, R.J. Longman, T. Miura, Q. Chen, and M.A. Nullet, 2013: Development of high spatial resolution solar radiation maps for Hawai‘i. American Geophysical Union Fall Meeting, San Francisco, December 2013. Presented by Ryan Longman.

Longman, R.J., H.F. Diaz, and T.W. Giambelluca, 2014: Sustained increases in lower tropospheric subsidence over the Central Tropical North Pacific drives a decline in high elevation precipitation in Hawai‘i. American Geophysical Union Fall Meeting, San Francisco, December 2014. Presented by Ryan Longman.

Giambelluca, T.W., M.A. Nullet, L.L. Loope, and R.J. Longman, 2011: Tropical island listening post—The climate monitoring network on Haleakalā. Hawai‘i Conservation Conference, Honolulu, August 2011. Presented by Lloyd Loope.

Giambelluca, T.W., H.F. Diaz, O. Elison Timm, M. Takahashi, A.G. Frazier, and R.J. Longman, 2011: Regional climate trends in Hawai‘i. American Geophysical Union Fall Meeting, San Francisco, December 2011. Presented by Tom Giambelluca.

Giambelluca, T.W., X. Shuai, M. Barnes, R.J. Longman, T. Miura, Q. Chen, R.J. Alliss and A.G. Frazier,2013: Mapping evapotranspiration in Hawai‘i. American Geophysical Union Fall Meeting, San Francisco, December 2013. Presented by Tom Giambelluca.